Micromachined Hot Wire Sensors for Turbulence Measurement Applications

Dissertation

zur Erlangung des Grades

des Doktors der Ingenieurwissenschaften

der Naturwissenschaftlich-Technischen Fakultät

der Universität des Saarlandes

von

Jianguo Zhao

Saarbrücken

2020

Tag des Kolloqiums: 16.12.2020

Dekan: Univ.-Prof. Dr. rer. nat. Jörn Walter

Berichterstatter: Prof. Helmut Seidel, Prof. Thrassos Panidis

Vorsitz: Prof. Chihao Xu

Akad. Mitarbeiter: Dr.-Ing. Paul Motzki

Kurzzusammenfassung

Hitzdrahtanemometer bieten eine effektive und zuverlässige Möglichkeit, Geschwindigkeit, Scherstress und Vortizität eines turbulenten Flussfeldes zu bestimmen. Durch die Anwendung von Mikrotechnologien, womit die Abmessungen des Hitzdrahts in den Bereich der Kolmogorov-Länge reduziert werden können, können kleinste Wirbel vermessen werden.

Sensoren mit Einzeldrähten sowie mit zwei jeweils ±45° geneigten Drähten mit kleinsten Abmessungen von 150 μm Länge, 3 μm Breite und 0.3 μm Dicke wurden hergestellt. Zur Vermeidung von Unterätzungen der Si-Zinken wurden Additive zu TMAH dazugegeben, wodurch auch die durch Pt katalysierte Dekomposition von H_2O_2 deutlich reduziert werden konnte.

Die Sensoren wurden im Konstant-Temperatur-Modus betrieben und die Dämpfung des Schaltkreises wurde mit der Root-Locus-Methode analysiert. Dabei spielen der Offset, das Verstärkungs-Bandbreite-Produkt und der Überhitzungsgrad eine wesentliche Rolle für die Stabilität. Die Schlussfolgerungen wurden mittels Spice-Simulation verifiziert.

Ein Square-Wave-Test wurde benutzt, um die Grenzfrequenz abzuschätzen. Für einen Draht mit 3 × 0.3 μm² Querschnitt wurden 200 kHz gefunden. Die Sensoren wurden in einem kleinen Windkanal kalibriert. Das Geschwindigkeits-Signal folgt dem King'schen Gesetz. Für die jeweilige Anwendung muss per Design ein sinnvoller Kompromiss zwischen Richtungsempfindlichkeit und räumlicher Auflösung gefunden werden. Die Messergebnisse zeigen, dass die ±45° Doppeldraht-Sensoren eine sehr gute Richtungsempfindlichkeit aufweisen.

Abstract

Hot wire anemometers are a useful and reliable tool for measuring turbulent flow quantities, such as velocity, shear stress, and vorticity. Nevertheless, the measurement of small scale eddies, particularly at the Kolmogorov scale, remains to be a challenge. This can be solved by microfabrication, reducing the hot wire's dimensions to be comparable to the Kolmogorov length.

Single wire and double 45° inclined hot wire sensors were microfabricated, with the smallest wire dimensions being down to 150 μm length ×3 μm width ×0.3 μm thickness. A primary challenge was to avoid undercutting of Si prongs by the etching process. This was alleviated by adding a surfactant to TMAH and by deactivating the decomposition of H_2O_2 catalyzed by Pt.

The sensors were operated at constant temperature mode, and the circuit damping was analyzed by the root locus method, showing that offset voltage, gain band product, and overheating ratio play essential roles in the stability. The conclusions were verified by Spice circuit simulations.

A square wave test was used to estimate the cutoff frequency, which was found to exceed 200 kHz for a wire with 3×0.3 μm² cross section. The sensors were calibrated in a small wind tunnel. The observed flow velocity responses comply with King's law. In addition, a reasonable compromise between directional sensitivity and spatial resolution has to be found for each application by sensor design. Double 45° wires proved to have excellent directional responses.

Table of Contents

Chapter 1　Introduction

1.1. Turbulence and its scales

Turbulence is a widespread flow phenomenon existing in nature and in artificial apparatus, such as atmospheric turbulence, ocean currents, chimney plumes, or wakes of an aircraft (see Figure 1-1). Its underlying mechanism has not been thoroughly understood yet so that it is regarded as one of the most challenging subjects of classical physics [1][2].

(a) Atmospheric turbulence　　　　　　　　　(b) Ocean currents
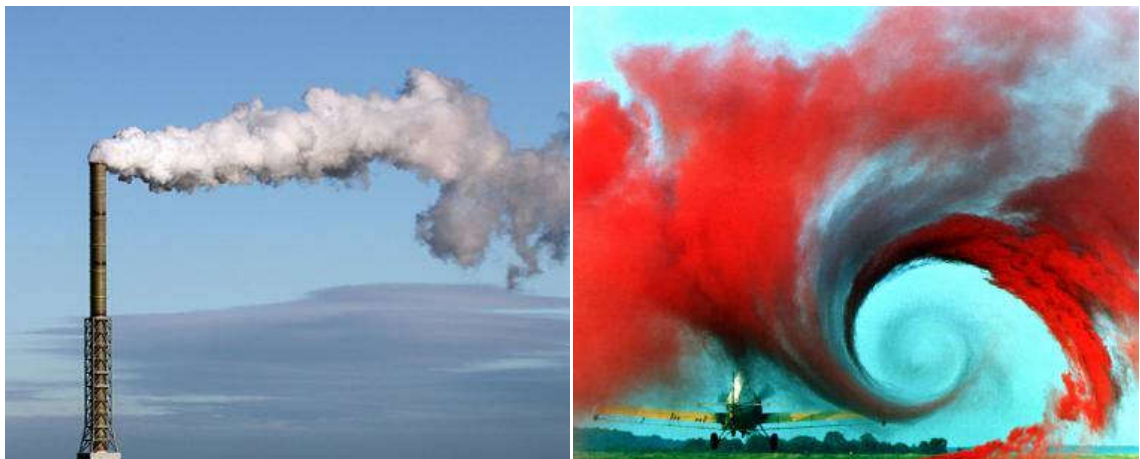
(c) Chimney plumes　　　　　　　　　(d) Wakes of an aircraft

Figure 1-1: Turbulence phenomena.

In turbulence, the velocity at a point undergoes irregular fluctuations, in contrast to laminar flow, in which the fluid motion changes continuously. The fluids' motion is also diffusive

and can thus enhance mixing. In addition, turbulence is usually associated with a high Reynolds number [3]. The so-called critical Reynolds number, which defines the onset of turbulence, depends on the flow situation. For current in a pipe, it is 2300, for a free streaming flow on a flat plate, the value can be as high as $Re > 5 \times 10^5$ [4][5]. Here Re is an indicator of the ratio of inertial forces versus viscous forces in a flow regime, with the following definition:

$$Re = \frac{VL}{\nu} \tag{1-1}$$

where V and ν are velocity and dynamic viscosity of fluids; L is the characteristic size of the investigated object.

The discovery of coherent structures in turbulence with the help of flow measurement tools reveals the quasi-order feature of turbulence [6][7][8][9][10][11][12][13][14]. Now, it is generally considered that turbulent flow is composed of eddies of different sizes and duration time, and energy exchange occurs from larger eddies to smaller ones, which is called energy cascade [15][16]. In some cases, energy transfer in inversely direction may also take place [17][18].
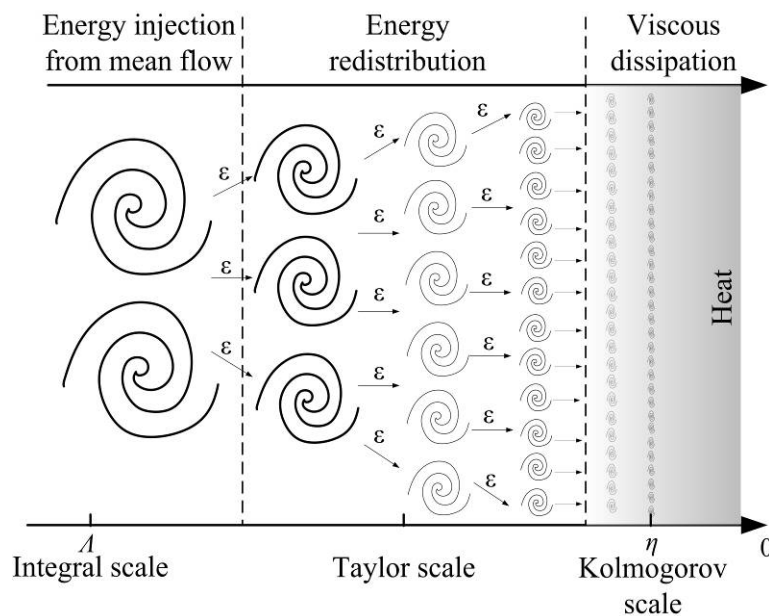
Figure 1-2: Eddies' evolution in turbulence and its energy cascade process.

The largest eddies are comparable to the characteristic sizes of the flow field, for example, the turbulent flow in a water pipe contains visible eddies as large as the pipe diameter. Reynold's number of eddies at this scale is huge, and inner inertial forces are thus dominant.

The eddies exhibit large velocity fluctuations and long duration time. They extract energy from the mean flow and transmit energy to somewhat smaller eddies. The small eddies will induce the still smaller eddies, and their Reynolds numbers are continuously reduced as well. The process persists until viscous forces become dominant. At the end of the energy cascade, the smallest eddies convert all energy into heat by viscous internal friction of the molecules of the fluid. The characteristic length of the smallest eddies is called Kolmogorov length η, where $Re = 1$. Accordingly, the characteristic time of these eddies is named as Kolmogorov time τ_η. They obey the following expressions[15]:

$$\eta \equiv \left(\frac{\nu^3}{\varepsilon}\right)^{\frac{1}{4}}, \tau_\eta \equiv \left(\frac{\nu}{\varepsilon}\right)^{\frac{1}{2}},\qquad(1\text{-}2)$$

where ε is the turbulence energy dissipation rate. In the case of high Reynolds number turbulence, the Kolmogorov length may be down to dozens of microns, and its characteristic time may reach several hundreds of kilohertz.

Broad scales in time and space are typical features of turbulence. The ratios of the largest to the smallest eddy in characteristic length and time increase as follows with the Reynolds number [19]:

$$\Lambda/\eta \sim Re^{3/4}, \quad \tau_\Lambda/\tau_\eta \sim Re^{1/2},\qquad(1\text{-}3)$$

Here Λ and τ_Λ are noted as the characteristic length and time of large eddies (usually referring to the integral scale, in which the largest eddies can be found). For turbulence at $Re > 5\times10^5$, the length of the largest and smallest structure may span at least four orders of magnitude, and their time scales may cover three orders of magnitude.

1. 2. Applications of hot wire anemometry in turbulent measurement

The accurate measurement of turbulent transportation has wide applications and significance. It will provide researchers with fundamental information to understand turbulence mechanisms and create better simulation models. The knowledge of turbulence models will further bring many practical benefits, such as forecasting weather, reducing aircraft drag, enhancing flight stability, controlling pollutant dispersion, and controlling automotive wind noise. PIV (Particle image velocimetry) [20][21][22], LDA (Laser Doppler anemometry) [23][24], and hot wire anemometry are the principal measurement

methodologies for turbulent flows [25][26]. Here, we focus on hot wire anemometry, which is based on a thermal convection principle and is used most frequently. Its applications in characterizing turbulent flows are mainly in the following fields:

(1) **Velocity measurement** Hot wires have been applied to measure the instantaneous velocity of turbulence for a long time [27][28][29][30]. Numerous efforts have been made in manufacturing technology to improve their temporal and spatial resolution. The classical so-called Wollaston process can produce very thin wires [31][32]. Ligrani employed it to produce a Pt-Rh alloy hot wire with a 0.625 μm diameter [33]. Bailey used laser trimming to reduce a nanoscale wire, which could achieve a measurement volume of 50 μm×50 μm×50 μm [34].
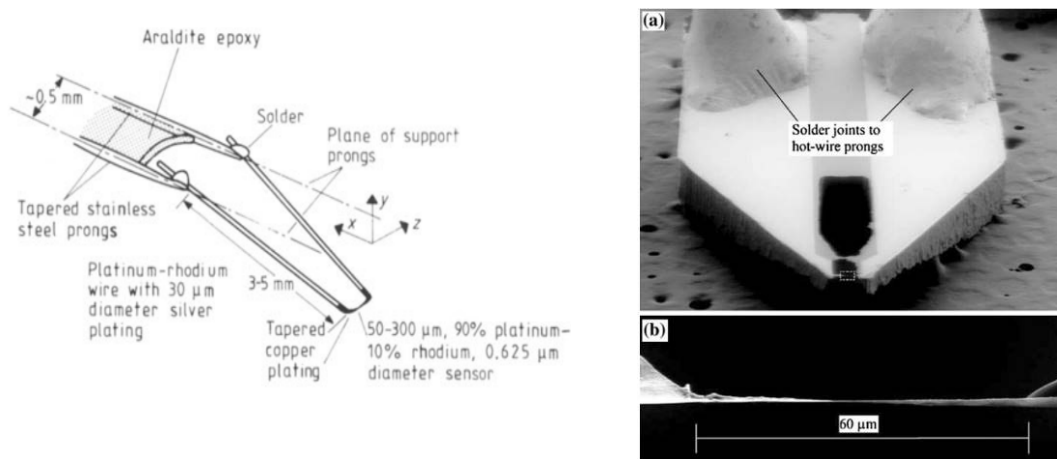
(a) Schematic diagram of a sub-miniature hot wire sensor based on the Wollaston process [33].

(b) A nanoscale hot wire manufactured by laser trimming [35].

Figure 1-3: Single hot wires applied to the velocity measurement of turbulent flows.

Besides velocity magnitude measurement, various structures of hot wire anemometers have been invented to measure flow directions. X-probe and triple wires are typical structures widely used to direction measurement [36][37], as shown in Figure 1-4. More complex structures by design have been categorized by Vukoslavčević [38][39]. The obtained velocity can be further used to calculate the so-called Reynolds stress to solve the Reynolds stress equation model describing turbulent flows [40][41][42]. It is an artificial stress tensor derived from an averaging operation of Navier-Stokes equation. Its magnitude is related to the fluctuating parts of turbulence velocity.
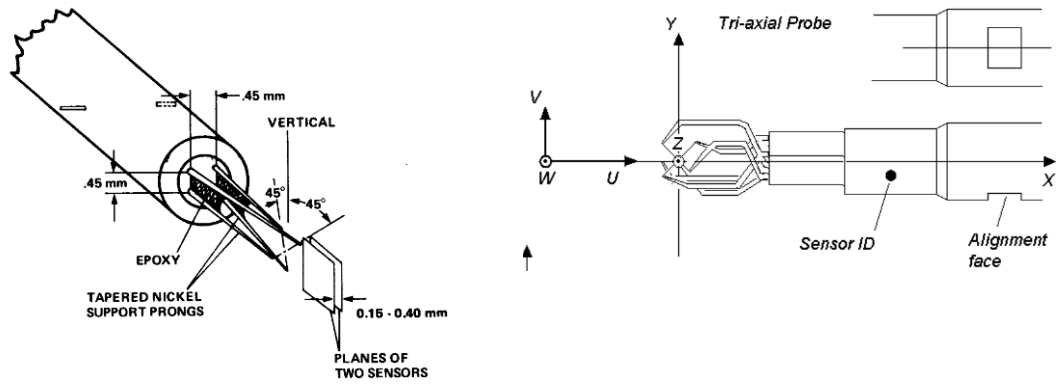
<table>
<tr><td>(a) X-array probe [43].</td><td>(b) Triple wire probe [44].</td></tr>
</table>

Figure 1-4: Hot wires applied to flow velocity direction measurement.

(2) **Wall shear stress measurement** Wall shear stress occurs in the flow near to a solid wall, where fluids undergo dramatic deformation due to wall constraints and the presence of fluid viscosity. It affects the velocity gradient of the flow boundary layer, and it is responsible for flow drag. Barenblatt found that the mean stream-wise velocity profile deviated from the universal logarithmic "law of the wall" in the turbulence boundary [45][46]. Savill and Mumford revealed that applying a large eddy break-up device to the turbulent boundary layer resulted in a drag reduction [47][48]. These findings have once more brought the researchers' attention to turbulent boundary layers and renewed the interest in measuring wall shear stress. The measurement principle is based on the premise that the stress is proportional to the velocity gradient. As an effective velocimetry, hot wires are the preferred devices for characterizing wall shear stress of turbulent flows applied on many occasions [49][50][51]. Typically, one or more parallel hot wires are employed to measure local velocity at specific positions near the wall (compare Figure 1-5).
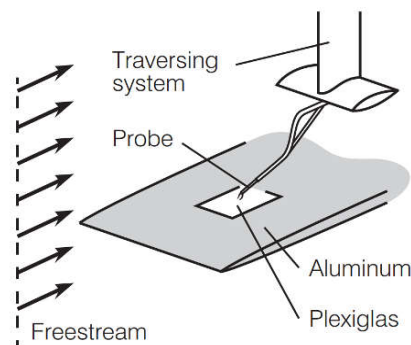
(a) Schematic setup for wall shear stress measurements using a single hot wire in a wind tunnel [50].
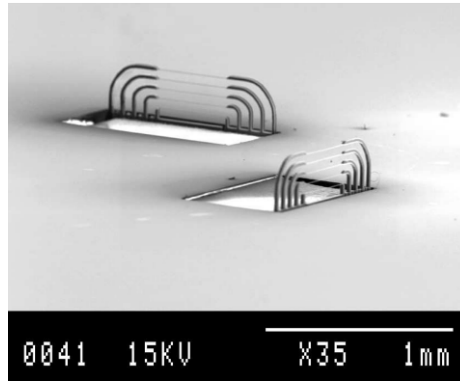
(b) Multiple parallel hot wires for wall shear stress fabricated by microfabrication technology [52].

Figure 1-5: Hot wire sensors for wall shear stress measurement applications.

(3) **Vorticity measurement** Vorticity is defined as the curl of the velocity vector flow field that is equal to twice the angular velocity of the fluid's rotation. Turbulence always has a characteristic of nonzero vorticity. In a sense, phase coherence within the vorticity field is regarded as the organizing principle of turbulent motion [53]. To resolve the vorticity of a flow field has been an elusive and long-held goal [54]55][56][57]. Kovasznay employed four hot wires to construct the first vorticity probe to measure the streamwise vorticity [58] (see Fig. 1-6). Since then, more wires and spatial arrangements have been constructed to simultaneously measure all components of the vorticity vector [10][59][60][61][62][63][64].
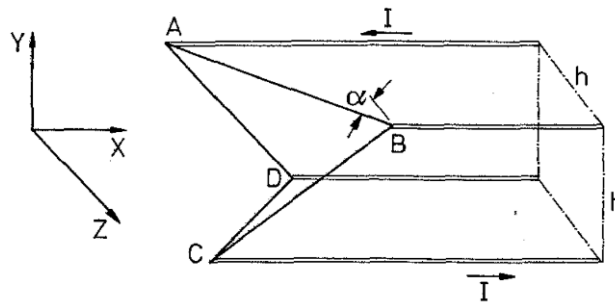
Figure 1-6: Kovasznay-type stream-wise vorticity probe consisting of four hot wires.
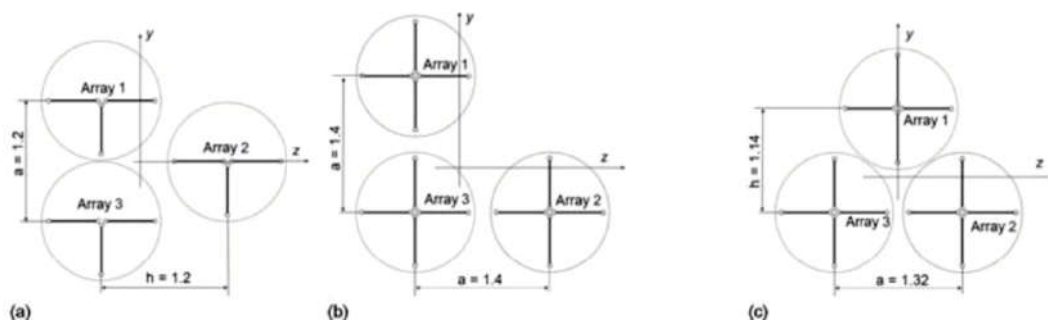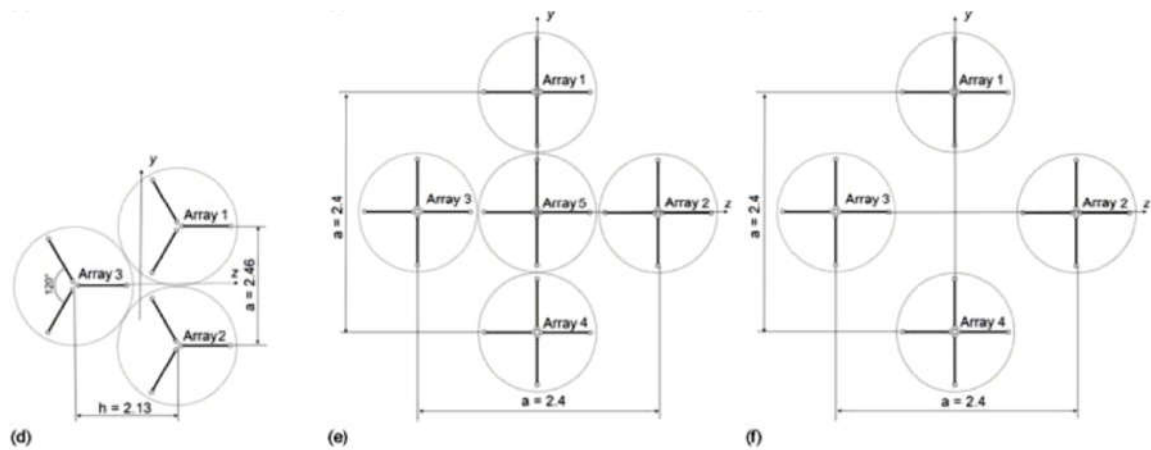
Figure 1-7: Various configurations of hot wires applied to turbulence vorticity measurement [65].

1.3. Motivation

Acquisition of velocity & its spatial distribution (velocity gradient) is the primary task of turbulence measurements and a prerequisite to determine wall shear stress and vorticity. All these quantities of interest can be obtained by using a number of hot wires with a specific spatial arrangement. As introduced previously, turbulence is comprised of multiple scales of fluid motion in the form of eddies. It is desirable to obtain full information of turbulence velocity in all scales. Considerable achievements in resolving large-scale turbulent structures have been made by hot wires. Nevertheless, the measurement at small scales remains a challenge in practice, due to the missing availability of a hot wire probe with small characteristic size and high response frequency [66][67][68][69].

To accurately probe fluid motions of the smallest structures that are defined by the Kolmogorov length, the hot wire length should be shorter than the Kolmogorov length [19]. Otherwise, the velocity signal will be lost or attenuated because of a spatial filter effect. This has been noted by many researchers. Wyngaard estimated that more than 10% attenuation occurs when wire length is equal to the Kolmogorov length [70]. Antonia pointed out that the effect would be exacerbated when multiple hot wires were regarded as a nominal measurement point to measure spatial derivatives of velocity in small-scale turbulence [71][72][73].

Furthermore, the temporal resolution of the measurement system should meet Nyquist criterion of the sampling theorem, which states that the sampling frequency should be twice larger than the signal frequency. The eddies at the Kolmogorov scale have the shortest

characteristic time τ_η. Therefore, a hot wire to measure the smallest turbulence structures should have a response frequency larger than $2/\tau_\eta$. According to the relation of hot wire cutoff frequency and wire size, which will be introduced in the following chapters, the reduction of hot wire's cross-section can increase its cutoff frequency considerably.

Motivated by a reduced spatial filter effect and an improved frequency response, we employed microfabrication technology to manufacture such hot wires. Single wire and double wires with 45° inclination are the focus of the investigation, which acts as the common element of various hot wire probes to measure turbulent flow quantities of interest. The double 45° hot wires are designed to measure flow, not only velocity magnitude but also the direction. These wires have the potential to be constructed to complicated 3D structures, which provide additional alternatives to measure more components of velocity, wall shear stress, or vorticity of turbulence.

Chapter 2   Fundamentals

2.1. Anemometers in turbulent flow velocity measurements

Various types of sensors and instruments with high performance were developed for measuring the transient velocity of turbulent flow research and industrial applications. Three basic types of measurement instruments are available: (1) hot wire anemometry (HWA), (2) laser Doppler anemometry (LDA), and (3) particle image velocimetry (PIV). A short introduction and comparison of these measurement techniques are given in the following, showing their state of advancement.

2.1.1. HWA

HWA is able to measure flow velocity at a single point, which is based on the heat convection principle. Due to its fast response and relatively low cost, it is most commonly used for velocity measurements of non-recirculating air or other gas flow. HWA usually consists of two parts: a thin electrically resistive wire and two prongs. The thin wire is usually made of a temperature-sensitive material whose resistance depends on the wire's temperature, such as nickel or platinum. The prongs are usually made of tungsten or other conducting materials. They are connected to the wire to provide mechanical and electrical interconnection. As a driving current is applied to the wire through the prongs, it is heated by the Joule effect. Once the HWA is placed in a flow, heat convection happens through the boundary between the wire and the fluid. The amount of heat that the fluid takes off from the HWA surface correlates to the flow velocity. King [74] investigated the relation of heat convection of heated platinum in a flow, and gave an expression of heat convection:

$$h_c = a_0 + b_0 V^{0.5},\qquad\qquad\text{(2-1)}$$

where V is the flow velocity, a_0 and b_0 are calibration constants, which are determined by the wire's geometry and fluid properties. When the wire is in thermal equilibrium, the heat generation rate of the Joule effect must be equal to the heat loss rate of flow convection. The power consumption of hot wire can be derived by measuring electrical parameter variations of the wire, such as the wire's resistance, current, voltage, or their combinations. Details of the readout circuit are introduced in the following chapters. For an HWA working in constant temperature mode, which is employed in the King's experiment, the relation of

voltage output and observed fluid velocity is given by

$$U^2 = a_1 + b_1 V^{0.5} ,$$
(2-2)

where a_1 and b_1 are constants, which are related to geometry and properties of the wire, fluid properties, as well as operation condition. They can be quantified in the calibration. Eq. (2-2) is usually used to estimate the flow velocity.
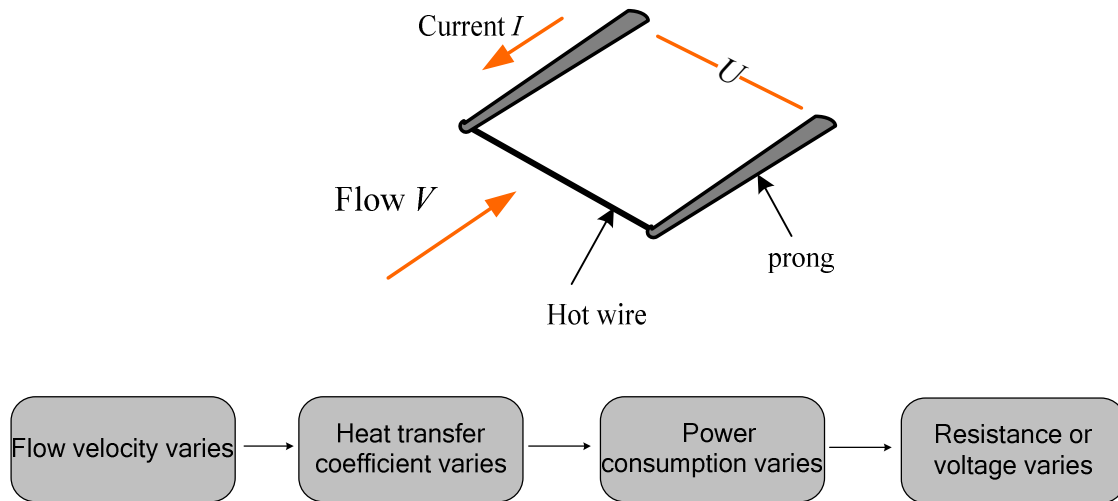
Figure 2-1: Schematic diagram of a hot wire sensor.

2. 1. 2. LDA

LDA is one of the most significant approaches for turbulence diagnostics because of its high spatial and temporal resolution. It is a nonintrusive technique which is based on the Doppler effect to measure the velocity at a single location. Small particles are seeded into the flow with their velocities corresponding directly to the flow velocity. These particles are spotted by a laser beam with a fixed wavelength as well as and scatter the light. If the particles are moving at a velocity relative to the beam, because of the Doppler effect, the frequency shift of the scattered light is proportional to the relative velocity. Thus, the particle's velocity can be derived by the frequency shift. Because the shift is only a small fraction of the laser frequency, it is difficult to measure it directly. To improve this measurement, two laser beams with identical frequency and an intersecting angle are used. The interference of two beams results in a fringe pattern in the intersecting area. As particles continually traverse brightness and darkness zones of the fringes, the intensity variation of the scattered light is modulated by the fringes' pitch. Correspondingly, the current signal of the photodetector fluctuates with a period. It can be shown mathematically that the reciprocal period is equal

to the Doppler-shifted frequency. Hence, the particle velocity is calculated by measuring the period of the receiver current. Note that the velocity is taken as the projection perpendicular to the bisector of the two beams. LDA can accurately measure the velocity in a wide range. However, the validate data rates are typically limited to several ten kilohertz in practical due to the concentration of seeded particles and due to the size of the intersection area [75]. Another limitation is the difficulty in measuring velocities near walls [76].
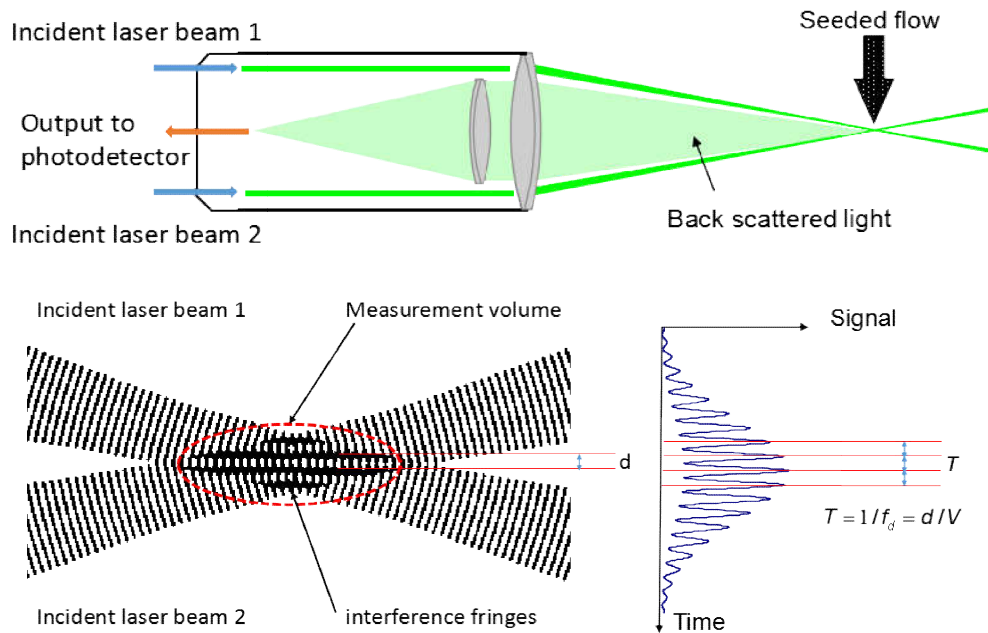
Figure 2-2: Schematic diagram of LDA.

2. 1. 3. PIV

PIV is the most popular method nowadays to visualize entire flow fields and to quantify instantaneous scalar or vector velocity without intrusion. The modern development of high frame rate and high pixel resolution cameras, short-pulse laser with high exposure dose, as well as the image processing algorithm opened the possibility to capture snapshots of moving particles and analyze their tracks in the flow field. To achieve visualizing the flow field, a sufficient number of small particles are homogeneously and contentiously seeded into the field. They are exposed by the laser pulse and act as a tracer. By means of synchronizing trigger signal of laser pulse and camera's shutter, images of seeding particles can be captured in a rapid sequence by a high frame rate camera. Note that the time interval between two adjacent exposures should be smaller than the time scale of the measured flow. The location changing in the adjacent frames corresponds to their displacement. Each

particle's velocity is approximately equal to its displacement divided by the time interval. However, it is hugely challenging to identify all particles in the images and record their location variation. Alternatively, a cross-correlation operation is used to estimate the "mean" displacement of particles in the sub-regions. The captured images are divided into subdomains, which are called interrogation areas. A peak of cross-correlation represents the displacement of overall particles in this area. Therefore, the size of the interrogation determines the spatial resolution of PIV. With respect to the throughput performance of the camera, a tradeoff between the spatial resolution and the temporal resolution is made [77][78]. Typical PIV frequency response is in the range of hundred Hertz with a spatial resolution in the millimeter range [76].
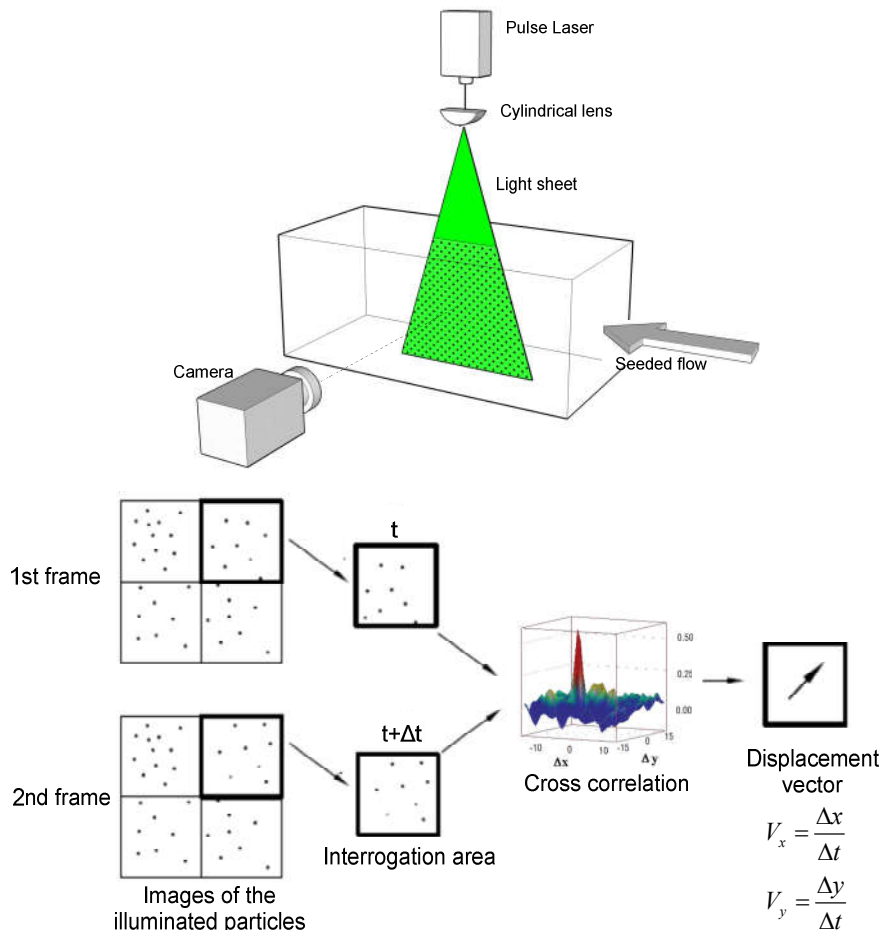
Figure 2-3: Schematic diagram of PIV.

A brief comparison with these three types of tools is given in the table below. Note that none of these tools can meet all requirements in all situations in turbulent flow measurement. In practice, they are complementary to such measurements.

Table 2-1: Comparison of methods in turbulent flow measurement.

	HWA	LDA	PIV
Signal property	Nonlinear, analog	Linear, discrete, no need for calibration	Linear, discrete
Spatial resolution	Single point measurement, depending on the diameter of hot wires, typically 5 μm × 1000 μm	Single point measurement, depending on the diameter of laser beams' waist, typically 100 μm × 1000 μm	Multi-point measurement, depending on the interrogation size and camera resolution, typically 1 mm × 1 mm
Temporal resolution	Depending on the structural size of hot wire and material. Up to several hundreds of kHz	Depending on seeds' concentration and diameter of laser beams' waist. Typically tens of kHz	Depending on the frame rate and laser pulse's frequency. Typically hundreds of Hz
Intrusive or not-intrusive	Intrusive	Non-intrusive, but needs seeds	Non-intrusive, but needs seeds
Cost	Relative low	Expensive	Very expensive

2.2. Heat transfer model of hot wire

A real hot wire placed in the flow suffers Joule heating, thermal conduction, heat radiation, natural convection, forced convection, and the wire itself also stores some heat, as illustrated in Figure 2-4.
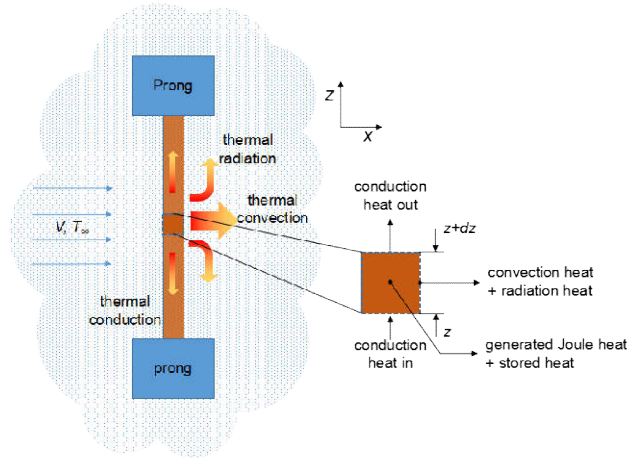
Figure 2-4: Heat transfer of hot wire.

Since the hot wire is made of thermally conductive material (thermal conduction coefficient > 10 W/(m·K)), and its diameter is extremely small to the order of 10^{-6} m, the radial temperature distribution can be regarded as quite uniform. Even if the convection coefficient is up to the order of 10^4 W/(m²·K), the wire's Biot number remains far less than 0.1(Biot number is dimensionless criteria, Bi=$h·L/k_f$, which indicates whether or not the temperatures inside a body will vary significantly. When it is less than 0.1, the temperature distribution of the inner body is uniform). Hence, the wire can be treated as a one-dimensional object for the integral or differential operation.

We note the mean temperature of hot wire and its total resistance as T_w and R_w, thus $T_w = \frac{1}{l}\int_{-0.5l}^{0.5l} T(z)\mathrm{d}z$ and $R_w = \int_{-0.5l}^{0.5l} \rho_r(z)\mathrm{d}z$, where $T(z)$ and $\rho_r(z)$ are the temperature and resistivity at position z of hot wire; l is the wire length. According to the first law of thermodynamics, Joule heating power P is absolutely equal to the sum of all dissipation rates for all types of heat transfer. For any differential element in the wire, there is

$$\mathrm{d}P = \mathrm{d}\dot{Q}_{fc} + \mathrm{d}\dot{Q}_{nc} + \mathrm{d}\dot{Q}_{cd} + \mathrm{d}\dot{Q}_r. \qquad (2\text{-}3)$$

where $\dot{Q}_{fc}$, $\dot{Q}_{nc}$, $\dot{Q}_{cd}$, and $\dot{Q}_r$, represent heat transfer rate by forced convection, natural convection, thermal conduction, and thermal radiation; $\dot{Q}_s$ is the heat storage rate. The individual terms in Eq. (2-3) can be expressed as follows:

1) Joule heating rate dP:

$$dP = I^2 dR_w = \frac{I^2 \rho_r(z)}{A_c} dz ,\qquad (2\text{-}4)$$

where I is the electrical current in the wire; A_c is the cross-sectional area of the wire. Most frequently, platinum is used as the sensitive material of a hot wire sensor, due to its highly linear temperature coefficient of resistance (T CR), α. The resistivity is of the form

$$\rho_r(z) = \rho_0[1 + \alpha[T(z) - T_0]] = \rho_a + \rho_0 \alpha[T(z) - T_a] ,\qquad (2\text{-}5)$$

where ρ_a and ρ_0 are the platinum resistivity at the temperature T_a ($\approx 15°\text{C}$) and at $0°\text{C}$.

2) Forced convective heat transfer rate $\dot{Q}_c$:

$$d\dot{Q}_{fc} = h_c A_p [T(z) - T_a] dz ,\qquad (2\text{-}6)$$

where A_p is the perimeter of the wire's cross-section

$$d\dot{Q}_{nc} = h_{nc} A_p [T(z) - T_a] dz ,\qquad (2\text{-}7)$$

where h_{nc} is the natural convection coefficient.

3) Thermal radiation rate $\dot{Q}_r$:

$$d\dot{Q}_r = \sigma\varepsilon[T(z)^4 - T_a^4] A_p dz ,\qquad (2\text{-}8)$$

where σ is Stefan Boltzmann constant, ε is the emissivity of the material.

4) Heat storage rate $\dot{Q}_s$:

$$d\dot{Q}_s = \rho_m c_m A_c \frac{\partial T(z)}{\partial t} dz ,\qquad (2\text{-}9)$$

where ρ_m is the density of the wire, c_m is the specific heat capacity.

5) Heat transfer rate of thermal conduction to prong $\dot{Q}_{cp}$:

$$d\dot{Q}_{cp} = -k_w A_c \frac{\partial^2 T(z)}{\partial z^2} dz ,\qquad (2\text{-}10)$$

where k_w is the thermal conduction coefficient of hot wire. Substituting with the above expressions for dP, $d\dot{Q}_{fc}$, $d\dot{Q}_{nc}$, $d\dot{Q}_{cp}$, $d\dot{Q}_r$, $d\dot{Q}_s$ of Eq. (2-3), the governing equation for the hot wire sensor is obtained:

$$-k_w A_c \frac{\partial^2 T(z)}{\partial z^2} + \rho_m c_m A_c \frac{\partial T(z)}{\partial t} + (h_c + h_{nc}) A_p [T(z) - T_a] + \sigma \varepsilon A_p [T(z)^4 - T_a^4] = \frac{I^2 \rho_r(z)}{A_c} . \quad (2\text{-}11)$$

In most applications, the contribution of radiation and natural convection can be neglected. Some investigation indicated that the error due to ignoring radiation is in the range of 0.1-0.01% [79]. Collis examined the contribution of natural convection and suggested that it can be neglected at $Re > 0.58 \, Gr^{1/3}$, where Gr is Grashof number, a dimensionless quantity which approximates the ratio of the buoyancy to the viscous force acting on a fluid [80]. Stengele confirmed the conclusion of Collis and proposed a critical Reynolds number $Re > 0.0045$, where the contribution of convective heat transfer is smaller than 1% [81]. By ignoring the terms of radiation and natural convection in Eq. (2-11) and substituting $\rho_r(z)$ with Eq. (2-5), Eq. (2-11) can be simplified to

$$k_w A_c \frac{\partial^2 T(z)}{\partial z^2} - \rho c_p A_c \frac{\partial T(z)}{\partial t} + (\frac{I^2 \rho_0 \alpha}{A_c} - h_c A_p)[T(z) - T_a] + \frac{I^2 \rho_a}{A_c} = 0 . \quad (2\text{-}12)$$

$T(z)$ depends on the heat convection coefficient h_c and the heating current I. To solve Eq. (2-12), h_c and I, are decomposed into a time-averaged or static part and into a small fluctuating part. They are denoted by over bar and prime symbols, respectively:

$$h_c = \overline{h}_c + h_c', \quad I = \overline{I} + I' .$$

The fluctuating part is a function of time and is assumed to be a small deviation from the steady part. Accordingly, the resultant quantity $T(z)$, can also be regarded as a superposition of a time-averaged part and a fluctuating part.

$$T(z) = \overline{T}(z) + T'(z) .$$

When all terms that involve the product of two quantities are neglected, accordingly, Eq. (2-12) is separated into a static and a transient equations:

$$k_w A_c \frac{\partial^2 \overline{T}(z)}{\partial z^2} + (\frac{\overline{I}^2 \rho_0 \alpha}{A_c} - \overline{h}_c A_p)[\overline{T}(z) - T_a] + \frac{\overline{I}^2 \rho_a}{A_c} = 0 , \quad (2\text{-}13)$$

$$k_w A_c \frac{\partial^2 T'(z)}{\partial z^2} - \rho c_p A_c \frac{\partial T'(z)}{\partial t} + (\frac{\overline{I}^2 \rho_0 \alpha}{A_c} - \overline{h}_c A_p) T'(z) + (\frac{2\overline{I} \rho_0 \alpha I'}{A_c} - A_p h_c')[\overline{T}(z) - T_a] + \frac{2\overline{I} \rho_a I'}{A_c} = 0$$
$$(2\text{-}14)$$

The solution of the static equation is given by Brunn[26]:

$$\overline{T}(z) = \frac{I^2 \rho_a l_c^2}{k_w A_c^2} \cdot [1 - \frac{\cosh(z/l_c)}{\cosh(0.5l/l_c)}] + T_a , \qquad (2\text{-}15)$$

where $l_c^2 = k_w A_c / (\dfrac{I^2 \rho_0 \alpha}{A_c} - \overline{h}_c A_p)$ is called "cold length" The time-averaged temperature over the wire length thus can be expressed as:

$$\overline{T}_w = \frac{1}{l} \int_{-0.5l}^{0.5l} \overline{T}(z) dz = \frac{I^2 \rho_a l_c^2}{k_w A_c^2} [1 - \frac{\tanh(0.5l/l_c)}{0.5l/l_c}] + T_a . \qquad (2\text{-}16)$$

In order to illustrate the temperature distribution along the wire, the temperature along the wire is normalized by $[\overline{T}(z) - \overline{T}_a]/(\overline{T}_w - \overline{T}_a)$, as shown in Figure 2-5. It can be seen that a wire with a longer length has a more uniform temperature distribution.
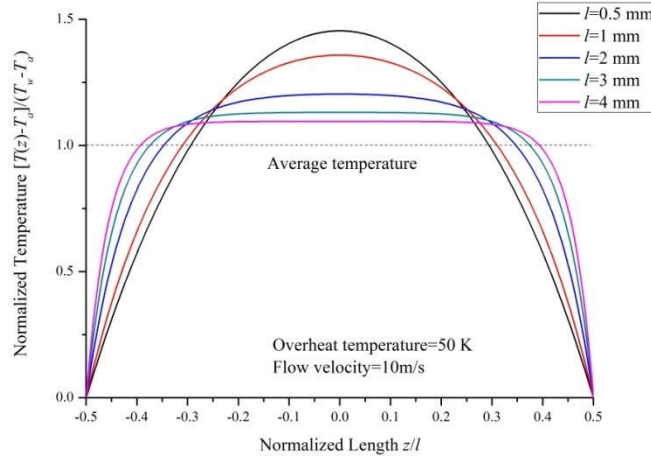
Figure 2-5: Temperature distribution along the wire length.

The resistance of the entire hot wire at the ambient temperature T_a is noted as $R_a = \rho_a l = \int_{-0.5l}^{0.5l} \rho_a dz$. According to the Leibniz integral rule, $\int_{-0.5l}^{0.5l} \frac{\partial T(z)}{\partial t} dz = l \cdot \frac{\partial (\int_{-0.5l}^{0.5l} T(z) dz)}{\partial t} = l \cdot \frac{\partial T_w}{\partial t}$. Applying integrating operation to Eq. (2-12) with respect to variable z, there is

$$k_w A_c \frac{\partial T(z)}{\partial z}\Big|_{-0.5l}^{0.5l} - \rho c_p A_c l \frac{\partial T_w}{\partial t} + (I^2 R_0 \alpha - h A_p l)(T_w - T_a) + I^2 R_a = 0 . \qquad (2\text{-}17)$$

The first term in Eq. (2-17) represents the thermal conduction contribution. It can be ignored if its portion to the total transferred heat is less than 5% [82]. Therefore, when thermal conduction is ignored, the governing equation of hot wire is obtained:

$$\rho c_p A_c l \frac{\partial T_w}{\partial t} + (h_c A_p l - I^2 R_0 \alpha)(T_w - T_a) = I^2 R_a . \qquad (2\text{-}18)$$

It defined the mean temperature variation with respect to time when prescribed current, and convection conditions are applied to a hot wire. By introducing an expression $T_w - T_a = (R_w - R_a)/R_0 \alpha$ to eliminate temperature variables in Eq. (2-18), a new expression of the governing equation with respect to the hot wire resistance is derived

$$\rho c_p A_c l \frac{\partial R_w}{\partial t} + (R_w - R_a)(h_c A_p l - I^2 R_0 \alpha) - I^2 R_a R_0 \alpha = 0 \qquad (2\text{-}19)$$

By a similar treatment as done to T_w, R_w can also be decomposed into static and fluctuating parts. Thus, static and transient equations are extracted from Eq. (2-19)

$$(\bar{R}_w - R_a)(\bar{h}_c A_p l - \bar{I}^2 R_0 \alpha) = \bar{I}^2 R_a R_0 \alpha . \qquad (2\text{-}20)$$

$$\rho c_p A_c l \frac{\partial R'_w}{\partial t} + (\bar{h}_c A_p l - \bar{I}^2 R_0 \alpha) R'_w = A_p l (R_a - \bar{R}_w) h'_c + 2\overline{IR}_w R_0 \alpha I' . \qquad (2\text{-}21)$$

Solving the static equation, the time-averaged resistance of a hot wire is obtained

$$\bar{R}_w = \frac{\bar{h}_c A_p l R_a}{\bar{h}_c A_p l - \bar{I}^2 R_0 \alpha} . \qquad (2\text{-}22)$$

Introducing the voltage drop on the wire, $U = IR_w$, to simplify Eq. (2-20), there is

$$\bar{U}^2 = \frac{\bar{h}_c A_p l \bar{R}_w (\bar{R}_w - R_a)}{R_0 \alpha} . \qquad (2\text{-}23)$$

If the response of the hot wire measurement system is far faster than flow velocity or convection coefficient variation, a more operable expression without time averaging operation will take the place of Eq. (2-23) to approximate the correlation between voltage drop and convection coefficient:

$$U^2 = \frac{h_c A_p l R_w (R_w - R_a)}{R_0 \alpha} \qquad (2\text{-}24)$$

As for the dynamic behavior of hot wire, it is determined both the hot wire and its driving circuit. The time response of hot wire is governed by Eq. (2-21). Sorting the terms of it, there is

$$\frac{\rho c_p A_c l}{A_p \overline{h}_c l - \overline{I}^2 R_0 \alpha} \frac{\partial R'_w}{\partial t} + R'_w = -\frac{A_p l (\overline{R}_w - R_a)}{A_p \overline{h}_c\_ c l - \overline{I}^2 R_0 \alpha} \cdot h' + \frac{2 \overline{IR}_w R_0 \alpha}{A_p \overline{h}_c l - \overline{I}^2 R_0 \alpha} \cdot I' \,. \quad (2\text{-}25)$$

Taking Laplace transform of Eq. (2-25), the transient resistance of the hot wire in Laplace domain is obtained:

$$R'_w(s) = -\frac{K_v}{\tau_w s + 1} \cdot h'_c(s) + \frac{K_i}{\tau_w s + 1} \cdot I'(s) \,, \qquad\qquad (2\text{-}26)$$

where s is Laplace variable,

$$K_v = \frac{A_p l (\overline{R}_w - R_a)}{A_p \overline{h}_c l - \overline{I}^2 R_0 \alpha} \,, \quad \tau_w = \frac{\rho c_p A_c l}{A_p \overline{h}_c l - \overline{I}^2 R_0 \alpha} \,, \quad K_i = \frac{2 \overline{IR}_w R_0 \alpha}{A_p \overline{h}_c l - \overline{I}^2 R_0 \alpha} \,.$$
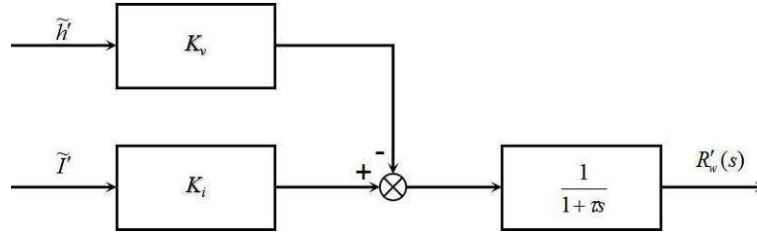
Figure 2-6: Block diagram of the hot wire.

2.3. Correlation of forced convection coefficient and flow velocity

The convection coefficient indicates the convective heat transfer capability. Solving the coefficient is the core issue of the fluid-solid conjugate heat transfer problem. While Eq. (2-24) links forced convection coefficient to the wire's voltage, an explicit expression between velocity and the wire's voltage can not be directly derived unless a correlation between the coefficient and velocity has already been known.

2.3.1. Convection of an infinitely long cylinder with an arbitrary cross-section

To develop a correlation of convection coefficient and flow velocity, we restrict our attention to the heat transfer on an arbitrary cross-section of hot wire. It is assumed that the hot wire has an infinite length with a very smooth surface, and the forced convection exclusively dominates heat transfer, neglecting thermal conduction to the prongs and other types of heat losses.

Figure 2-7: Temperature and velocity boundary layer on an arbitrary shape.

As the wire is suspended in the flow, a thermal boundary layer and a temperature boundary layer always coexist between the fluid and the wire's 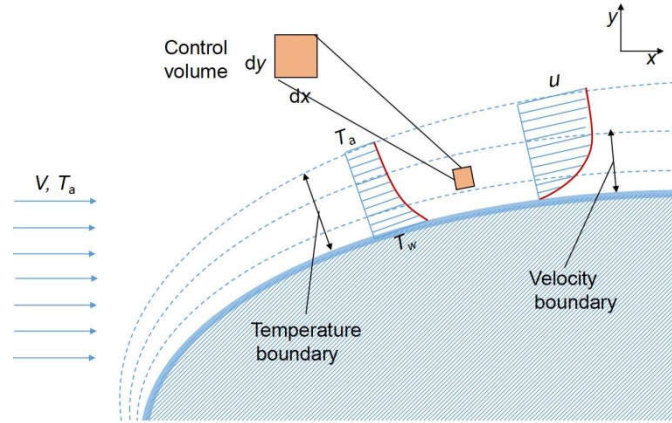surface, as illustrated in Figure 2-4. Due to the temperature difference between the wire and its surrounding fluid, heat is transferred into the thermal boundary layers by momentum exchange and diffusion of fluid molecules. According to Newton's cooling law, the convective heat is expressed as

$$\dot{Q} = h_c A_p (T_w - T_a),$$ (2-27)

Meanwhile, according to Fourier law, the transferred heat by thermal conduction between the wire surface and adjoining fluid layer at $y=0$ is of the form

$$\dot{Q} = -k_f A_p \left.\frac{\partial T}{\partial y}\right|_{y=0},$$ (2-28)

where k_f is the thermal conduction coefficient of the fluid. On the surface of the hot wire, there is no fluid motion and heat transfer occurs only by thermal conduction. Combining Eq. (2-27) with (2-28), the convective coefficient is thereby expressed by the following formula

$$h = \frac{-k_f \left.\partial T/\partial y\right|_{y=0}}{T_w - T_a}.$$ (2-29)

Dimensionless parameter similarity is an advantageous method to handle fluid dynamics and heat transfer problems. It allows us to extrapolate the result obtained from a surface experiencing one set of controlled conditions to any surface, as long as they have similar geometry and similar dimensionless parameters. Normalizing y and T of Eq. (2-29) by the characteristic length of hot wire L and the temperature difference between fluid and solid surface, Eq. (2-29) is thus converted to

$$\frac{h_c L}{k_f} = +\frac{\partial T^*}{\partial y^*}\bigg|_{y^*=0} = Nu \qquad (2\text{-}30)$$

where, the left term is regarded as a dimensionless parameter of heat convection coefficient h_c, called Nusselt number. Once the Nusselt number is known, the convection coefficient is thus solved by

$$h_c = \frac{k_f}{L} \cdot Nu \qquad (2\text{-}31)$$

Eq. (2-30) reveals that the fluid's temperature gradient $\partial T^*/\partial y^*$ is the key to solve the convective coefficient. Turning back to forced convection of hot wire in the flow, the fluid motion and heat transfer must comply with the conservation laws of mass, momentum, and energy. Based on the boundary layer theory, the diffusion terms of velocity and temperature along the surface (x-direction) are much smaller than those normal to the wire's surface. With the exception of the occasion of some high Mach number flow, it is reasonable to neglect the variation of aerodynamic heating because of the viscous stress of velocity. Besides, the pressure gradient along the surface is approximately equal to the mainstream gradient. Therefore, the equations of these laws applying to any control volume in the boundary layers are simplified as follows:

$$\text{Continuity equation: } \frac{\partial u}{\partial x} + \frac{\partial \upsilon}{\partial y} = 0 \text{ ,} \qquad (2\text{-}32)$$

$$\text{Momentum equation: } u\frac{\partial u}{\partial x} + \upsilon\frac{\partial \upsilon}{\partial y} = -\frac{1}{\rho}\frac{dp}{dx} + v\frac{\partial^2 u}{\partial y^2} \text{ ,} \qquad (2\text{-}33)$$

$$\text{Energy equation: } u\frac{\partial T}{\partial x} + \upsilon\frac{\partial T}{\partial y} = \alpha\frac{\partial^2 T}{\partial y^2} \text{ ,} \qquad (2\text{-}34)$$

where ρ, v, α are the density, kinematic viscosity, and thermal diffusivity of the fluid, p, T are the pressure and temperature of the fluid, u, and v are the x and y components of the fluid velocity. The dimensionless form of the above equations are expressed as

$$\frac{\partial u^*}{\partial x^*} + \frac{\partial \upsilon^*}{\partial y^*} = 0 \qquad (2\text{-}35)$$

$$u^* \frac{\partial u^*}{\partial x^*} + \upsilon^* \frac{\partial u^*}{\partial y^*} = -\frac{\mathrm{d}p^*}{\mathrm{d}x^*} + \frac{1}{Re} \frac{\partial^2 u^*}{\partial y^{*2}}$$ (2-36)

$$u^* \frac{\partial T^*}{\partial x^*} + \upsilon^* \frac{\partial T^*}{\partial y^*} = \frac{1}{RePr} \frac{\partial^2 T^*}{\partial y^{*2}}$$ (2-37)

where, p^*, u^*, v^*, x^*, y^*, and T^* are the dimensionless form of $p, u, v, x, y,$ and T; Re and Pr are the Reynolds number and the Prandtl number (it is a dimensionless number to assess the relation between momentum transport and thermal transport capacity of a fluid, defined as the ratio of momentum diffusivity to thermal diffusivity [83]. The solution of $\partial T^*/\partial y^*$ at any position x^* can be obtained by solving the group of Eq. (2-35), Eq. (2-36), and Eq. (2-37). Referring to the definition of Nusselt number, Nusselt number at x^* (local Nusselt number), Nu_x, can be calculated. Hence, the local number can be expressed as a function of Reynolds number, the Prandtl number, and on the pressure gradient.

$$Nu_x = f_1(x^*, Re, Pr, \frac{dp^*}{dx^*})$$ (2-38)

Note that $\mathrm{d}p^*/\mathrm{d}x^*$ represents the geometry effect on fluid motion. For a prescribed geometry profile, the average Nusselt number of the overall surface is a variable, dependent on the Reynolds number and the Prandtl number.

$$Nu = f_2(Re, Pr)$$ (2-39)

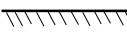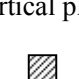An analytical solution of the Nusselt number can be obtained only in some exceptional cases, for example, the occasion of incompressible laminar flow [84]. The approximate solution for the general flow condition can be obtained by numerical simulation, such as the finite element method. Practically, Nusselt numbers of most engineering applications are estimated by experiment. Table 2-2 exhibits their Nusselt numbers for given geometries. Substituting Reynold's number of Eq. (2-39) with its definition, there is

$$Nu = f_2(\frac{VL}{\nu}, Pr)$$ (2-40)

Therefore, the Nusselt number is regarded as a function of flow velocity. Combing Eq. (2-40) and Eq. (2-24), A link from flow velocity and voltage drop is established. If the value of U is probed by specifically designed readout circuits, then the convection coefficient can be solved by applying Eq. (2-24). Consequently, the flow velocity can be derived by the

relation of the Nusselt number or convection coefficient.

Table 2-2: Geometry effect on Nusselt number [85].

Geometry	Nusselt number correlation [p455,fundanmental of heat and mass transfer]	Conditions
Plate	$Nu = 0.664Re^{1/2}Pr^{1/3}$	Laminar, $Pr \geq 0.6$
	$Nu = 0.037Re^{4/5}Pr^{1/3}$	Turbulence, $0.6 \leq Pr \leq 60$, $Re \leq 10^8$
Circular cylinder	$Nu = 0.42Pr^{0.2} + 0.57Pr^{0.33}Re^{0.50}$	$0.01 \leq Re \leq 10000$, $0.71 \leq Pr \leq 1000$
Non-circular cylinders	$Nu = CRe^m Pr^{1/3}$	
Square	$C = 0.246$, $m = 0.588$	$Re = 5 \times 10^3 - 10^5$
	$C = 0.102$, $m = 0.676$	$Re = 5 \times 10^3 - 10^5$
Hexagon	$C = 0.160$, $m = 0.638$	$Re = 5 \times 10^3 - 1.95 \times 10^4$
	$C = 0.0385$, $m = 0.782$	$Re = 1.95 \times 10^4 - 10^5$
	$C = 0.153$, $m = 0.638$	$Re = 5 \times 10^3 - 10^5$
Vertical plate	$C = 0.228$, $m = 0.731$	$Re = 4 \times 10^3 - 1.5 \times 10^4$

2.3.2. Convection of hot wire with a circular shape

Although a brief empirical relationship between flow velocity and voltage has been given in Eq. (2-2) by King, it is still necessary to clarify the unknown constants in the equations and examine its validity. In the case of the experiment of King, an infinitely long cylinder with a circular cross-section was employed. Its corresponding Nusselt number is as described in Table 2-2:

$$Nu = 0.42Pr^{0.2} + 0.57Pr^{0.33}Re^{0.50}.$$ (2-41)

Accordingly, the expression of the convection coefficient can be easily derived by Eq. (2-31). Introducing the obtained convection coefficient to Eq. (2-24), there is

$$U^2 = \frac{k_f}{R_0\alpha} \cdot \frac{A_p l}{L} \cdot (0.42Pr^{0.2} + 0.57Pr^{0.33}Re^{0.50})(R_w - R_a)R_w.$$ (2-42)

Replacing Pr and Re with their original definition, there is

$$U^2 = \frac{0.42\pi\mu^{0.2}k_f^{0.8}C_p^{0.2}l(R_w - R_a)R_w}{R_0\alpha} + \frac{0.57\pi\rho^{0.5}\mu^{-0.17}k_f^{0.67}C_p^{0.33}ld^{-0.5}(R_w - R_a)R_w}{R_0\alpha} \cdot V^{0.5}.$$ (2-43)

where C_p is the heat capacity of the fluid, d is the diameter of the hot. Comparing Eq. (2-2) with Eq. (2-22), the constants a_1 and b_1 of King's law are thus obtained:

$$a_1 = \frac{0.42\pi\mu^{0.2}k_f^{0.8}C_p^{0.2}l(R_w - R_a)R_w}{R_0\alpha},$$ (2-44)

$$b_1 = \frac{0.57\pi\rho^{0.5}\mu^{-0.17}k_f^{0.67}C_p^{0.33}ld^{-0.5}(R_w - R_a)R_w}{R_0\alpha},$$ (2-45)

Nusselt number that was introduced in Eq. (2-41) is valid under the condition: a very long circular heated cylinder and a flow condition: $0.01 \leq Re \leq 10000$, $0.71 \leq Pr \leq 1000$, which implies the application scope of King's law. Recently accurate measurement shows King's law should be corrected to the following expression

$$U^2 = a_1 + b_1V^n$$ (2-46)

where n is a constant around 0.5 [86][87][88][89][90].

2.4. Measurements of the velocity vector

2.4.1. Effective cooling velocity

A hot wire anemometer is not only sensitive to the magnitude of the flow velocity but also its direction. Actually, taking the flow angle into account, the term V of Eq. (2-24) should be replaced by effective cooling velocity V_{eff}. The velocity vector can be decomposed into three components: V_N, V_T, and V_B. They are normal, tangential, and bi-normal to the hot wire, respectively (compare Figure 2-8). Each component's contribution to V_{eff} is expressed by a formula [91].

$$V_{eff}^2 = V_N^2 + kV_T^2 + hV_B^2 .$$ (2-47)

The weights of V_T and V_B contribution are defined as direction sensitivity factor, k and h. They can be calculated from the results of a calibration experiment. h is approximated to one, and k has a weak contribution and may be regarded as a constant or can even be ignored [92].
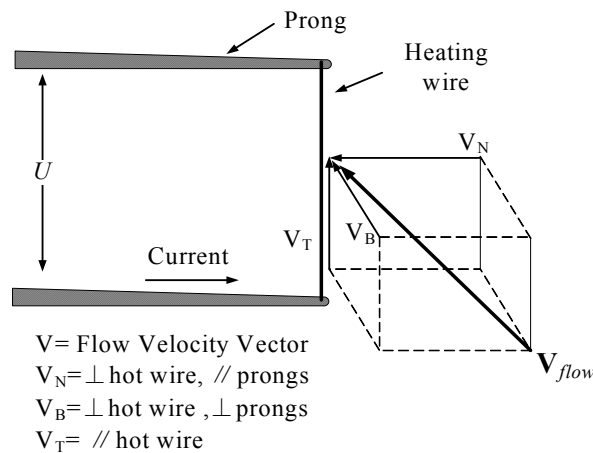
Figure 2-8: Hot wire and flow velocity vector definition.

2.4.2. Velocity direction measurement

Two hot wires can be assembled to specific structures to measure the velocity direction and the magnitude of two-dimensional flows. The typical structure, X-array probe, is described in the literature [93][94]. It consists of two orthogonal hot wire sensors, as shown in Figure 2-9. The prongs of the probe are aligned to the direction of the main flow direction. Applying the concept of effective cooling velocity to the two sensors, an equation group is

constructed:

$$\begin{cases} V_{eff1}^2 = (V_x \sin 45° + V_y \cos 45°)^2 + k(V_x \sin 45° - V_y \cos 45°)^2 \\ V_{eff2}^2 = (V_x \sin 45° - V_y \cos 45°)^2 + k(V_x \sin 45° + V_y \cos 45°)^2 \end{cases} \quad (2\text{-}48)$$

where V_{eff1} and V_{eff2} are the effective cooling velocity of the hot wire 1 and 2. The yaw factor k of the X-array probe usually varies in the range of 0.01-0.05, so it can be ignored [Bradshaw,2013]. Therefore, the coarse solution of Eq. (2-48) is obtained as follows

$$\begin{cases} V_x = \frac{\sqrt{2}}{2}(V_{eff1} + V_{eff2}) \\ V_y = \frac{\sqrt{2}}{2}(V_{eff1} - V_{eff2}) \end{cases} . \quad (2\text{-}49)$$
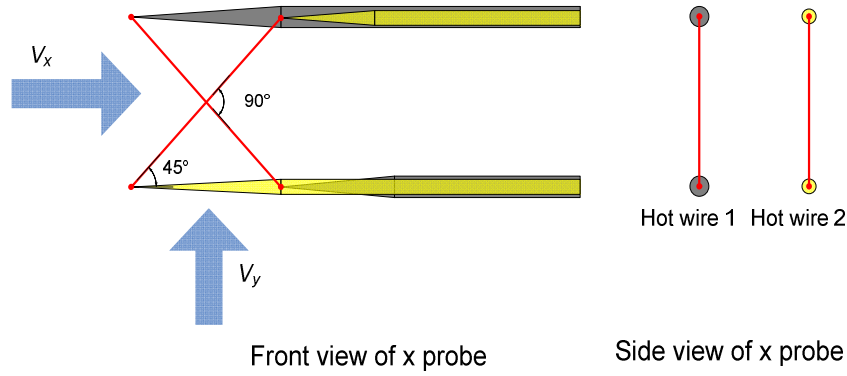
Figure 2-9: X probe structure.

Hot wires can also be configured to measure the three-dimensional velocity, such as a "T" array or an orthogonal array [95][96][62]. A typical "T" array contains three hot wires. Its configuration is illustrated in Figure 2-10. Similarly, an equation group is obtained by applying the concept of effective velocity to every hot wire.

$$\begin{cases} V_a^2 = (V_z \sin \alpha + V_x \cos \alpha)^2 + k(V_z \cos \alpha - V_x \sin \alpha)^2 + hV_y^2 \\ V_b^2 = (V_z \sin \alpha - V_y \cos \alpha)^2 + k(V_z \cos \alpha + V_y \sin \alpha)^2 + hV_x^2 \\ V_c^2 = (V_z \sin \alpha - V_x \cos \alpha)^2 + k(V_z \cos \alpha + V_x \sin \alpha)^2 + hV_y^2 \end{cases} . \quad (2\text{-}50)$$

where V_a, V_b, and V_c are the effective cooling velocity of the hot wires in the "T" array Eq. (2-50) contains three unknown variables V_x, V_y, and V_z. They have an analytical solution.

Figure 2-10: Structure of a "T" array probe.

2. 4. 3. Wall shear stress and vorticity measurement

In turbulence measurement, the measurement of vorticity and wall shear stress are also of great interest besides determining the velocity. Wall shear stress τ_w and vorticity ω_{tur} can be measured by using certain geometrical arrangements of multiple hot wires [54][97][9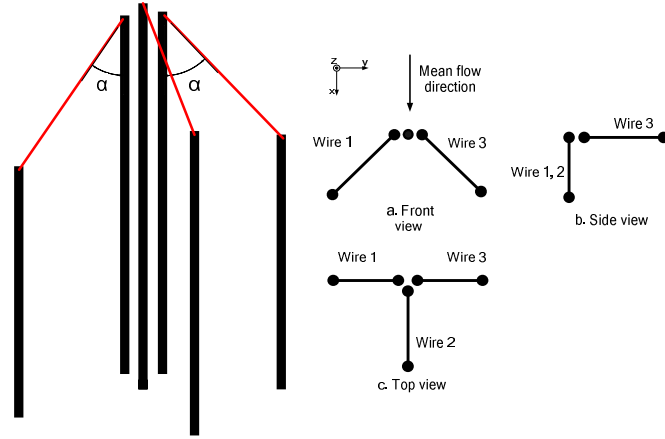8]. For turbulent air flow or isotropic Newtonian flow, these quantities are defined by derivatives of the velocity vector in the following way:

$$\tau_{wall} = \mu \nabla V \,, \tag{2-51}$$

$$\omega_{tur} = \nabla \times V = (\frac{\partial V_z}{\partial y} - \frac{\partial V_y}{\partial z}, \frac{\partial V_x}{\partial z} - \frac{\partial V_z}{\partial x}, \frac{\partial V_y}{\partial x} - \frac{\partial V_x}{\partial y}). \tag{2-52}$$

The velocity gradients can be determined by assembling several hot wires with small spatial intervals and by calculating the ratio of velocity variation between adjacent hot wires to the length of the intervals.

Specifically, for a one-dimensional wall shear stress measurement, two parallel hot wires are assembled with a particular pitch, as illustrated in Figure 2-11. The stress between the two wires is expressed in the form:

$$\tau_{wall} = \mu \frac{\partial V_z}{\partial y} \approx \mu \frac{V_{z2} - V_{z1}}{y_2 - y_1} \,. \tag{2-53}$$

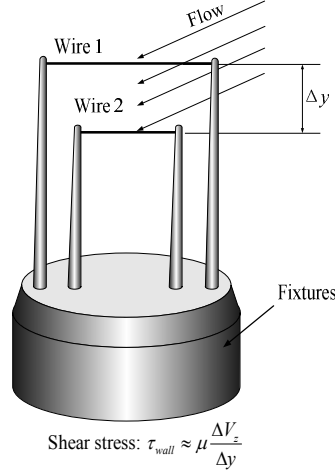Shear stress: $\tau_{wall} \approx \mu \dfrac{\Delta V_z}{\Delta y}$

Figure 2-11: Hot wires for shear stress measurement.

For vorticity measurements, more hot wires are required. Vorticity probes usually consist of three or four groups of hot wire arrays. Each array is regarded as a single point velocity probe, being able to detect the local velocity vector. A specific short distance separates these arrays. Figure 2-12 demonstrates a vorticity probe that contains three "T" arrays of 3D velocity probes. Each vorticity probe is placed along the stream-wise direction of the measured flow. The velocity components in the $x-, y-, z-$directions at every center position of the three arrays are denoted by $V_{i,n}$, where i and n represent the direction and each probe's ID. V_i, $V_i/\Delta x$ and $V_i/\Delta y$ can be well solved by solving Eq. (2-50). However, the centers of all velocity probes lie in the same z plane, that is to say $\Delta z = 0$. The values of V_z that are measured by different velocity probes are regarded as being identical. Hence, the solution of $V_i/\Delta z$ cannot be achieved directly. Nevertheless, $V_i/\Delta z$ can still be estimated approximately by Taylor's frozen-flow hypothesis [99]. Since the time it takes that the mean flow traverses the spatial structures of a stationary probe is far shorter than the inherent evolution time of the fluctuations [100][101], Taylor assumed that the spatial distribution of turbulence velocity is frozen without changing over the time scale of the velocity's temporal derivative at a single point [102][103]. Under this assumption, the gradient along the mean flow direction is given by [104]:

$$\frac{\partial V_i}{\partial z} \approx -\frac{1}{\overline{V_z}}\frac{\mathrm{d}V_i}{\mathrm{d}t} \approx -\frac{1}{\overline{V_z}}\frac{V_i(t_2)-V_i(t_1)}{t_2-t_1}, \tag{2-54}$$

where $\overline{V_z}$ is local mean velocity along the streamwise direction, $V_i(t_2)$ and $V_i(t_1)$ are the transient velocity along every direction at the time t_2 and t_1.
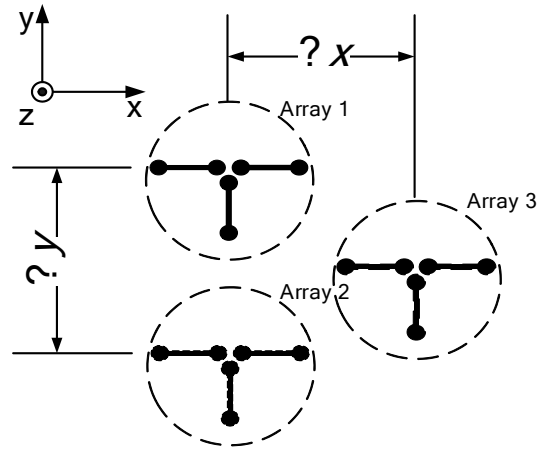
Figure 2-12: A typical configuration of a vorticity probe assembled by three "T" arrays.

2.5. The operation mode of the readout circuit

Hot wire can be operated in two modes, constant current mode (CC mode) or constant temperature mode (CT mode).

2.5.1. Constant current mode

In this mode, the current that heats the wire is kept constant. The resistance of the wires is varied with its temperature and results in a potential change. The potential drop is measured by a voltage meter to derive flow velocity. Figure 2-13 is a schematic diagram of the driving circuit for CC mode. The constant current source can be obtained in many forms of subcircuits that have been described in many references [105][106][107]. The voltage buffer has a very high output resistance and a low input resistance. Thus, it achieves an impedance transformation to isolate the interfering of voltage sampling on the hot wire.

Figure 2-13: Schematic diagram of a constant current circuit.

For constant current mode, $I'=0$ and $I = \bar{I}$. Laplace transform of transient resistance of the wire is then derived as

$$R'_w(s) = -\frac{K_v}{\tau_w s + 1} \cdot h'_c(s),$$ (2-55)
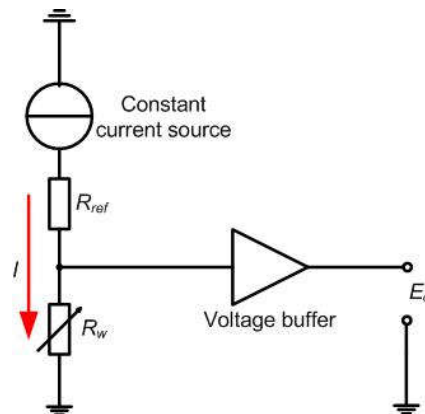
where K_v and τ have already been given in the expression mentioned above. $-K_v$ is also equal to the hot wire's static sensitivity of resistance to the convection coefficient. Normally, the voltage buffer can fast respond to hot wire. It is reasonable to assume that the hot wire self almost dominates the dynamic response of the overall hot wire measurement system, regardless of voltage buffer. Thus, fluctuating part of the output of the voltage buffer is expressed as

$$E'_o(s) = IR'_w(s) = \frac{-IK_v}{1+\tau_w s}$$ (2-56)

The transfer function of the measurement system is obtained as

$$H_{cc}(s) = \frac{E'_o(s)}{h'_c(s)} = \frac{-K_v}{1+\tau_w s},$$ (2-57)

Obviously, the transfer function is subject to a first-order (linear) system, which has a time constant τ_w to characterize how fast the response to a step input is. The expression of time constant τ_w has been expressed by Eq. (2-26).

Time constant provides characteristic time that the wire's resistance or averaged temperature recover to the value in thermal equilibrium when the wire undergoes an external perturbation, such as velocity fluctuation. Corrsin pointed out three sources of influence on the time constant: the wire material, its geometry, and the working conditions [108]. The time constant turns out to be independent of the wire length while being strongly dependent on the wire cross-section. Different materials may change the time constant by a factor two [109], with platinum giving the smallest value. Minimizing the cross-section of the wire's geometry can significantly improve the frequency response.

The bandwidth is a more explicit definition to describe the system's dynamic characteristics. In the field of signal processing and control, the bandwidth is usually defined as the difference between the upper and lower cutoff frequency. At the cutoff frequency, a system's output falls to -3 dB point corresponding approximately to the nominal passband amplitude

of 0.707. The cutoff frequency of a first-order system can be conveniently calculated by the time constant as follows:
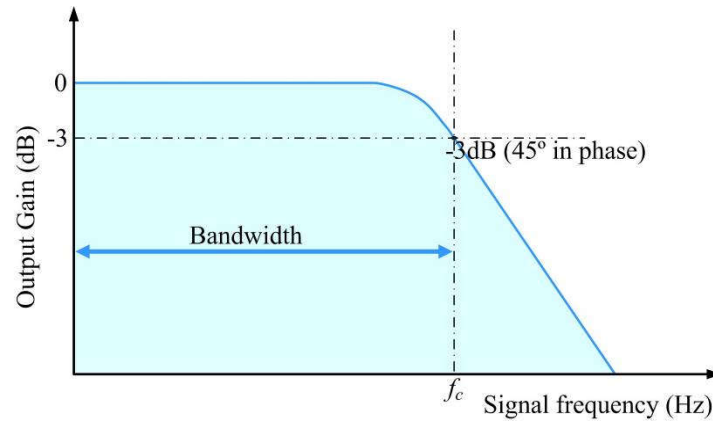
$$f_c = \frac{1}{2\pi\tau_w}. \tag{2-58}$$

Figure 2-14: Cutoff frequency and bandwidth of a hot wire sensor operating in constant current mode.

If the characteristic time of turbulence flow of investigated is far more significant than the time constant τ_w, then the fluctuating part of the flow can be precisely captured by CC hot wire measurement system. If so, then the relation between the output of the measurement system and the flow velocity can be expressed by modified King law.

2.5.2. Constant temperature mode

Although both CC and CT modes have the same signal-to-noise ratio (SNR) [110][111], CT mode is more widely used because of its excellent frequency response. Its bandwidth can reach hundreds of kilohertz, far more than the CC mode hot wire or LDA. In CT mode, the wire's temperature is kept constant by a feedback control circuit. Its schematic diagram is illustrated in Figure 2-15. Wheatstone resistance bridge circuit consists of a left-side-hand active bridge and a right-side-hand passive bridge. Hot wire is placed in the active bridge. Point A in the passive bridge is acted as a floating potential reference. The differential mode voltage between points A and B is fed to a voltage-to-current amplifier with high gain. Due to a positive TCR and self-heating, the wire's resistance is monotonically regulated by convective cooling and by the driving current. When the HWA is idle, the potential of the HWA and the reference point are quasi balanced. So, the differential mode voltage is almost equal to zero. When fluid flow is present, the heat convection tends to induce deviations of the wire's temperature from its balanced position, resulting in nonzero voltage output of the

bridge. The voltage is further amplified by the high gain amplifier and fed back to the bridge to establish a closed-loop control. As a result, HWA temperature and resistance are kept constant. The output voltage E_o and the voltage on hot wire U have the following relation

$$E_o = \frac{U(R_1 + R_w)}{R_w}.$$
(2- 59)

Replacing U of Eq. (2-59) with E_o, the relation between CT circuit output and flow convection is obtained:

$$E_o^2 = \frac{h_c A_p l(R_w - R_a)(R_1 + R_w)^2}{R_w R_0 \alpha}.$$
(2- 60)

When the relation between the convection coefficient of a hot wire and flow velocity complies with Eq. (2-1) or Eq. (2-41) that is the basis of King's law, the relation between CT circuit output and flow convection can be further expressed as a brief form:

$$E_o^2 = A + BV^n,$$
(2- 61)

where $A = a_1(R_1 + R_w)^2/R_w^2$, $B = b_1(R_1 + R_w)^2/R_w^2$.
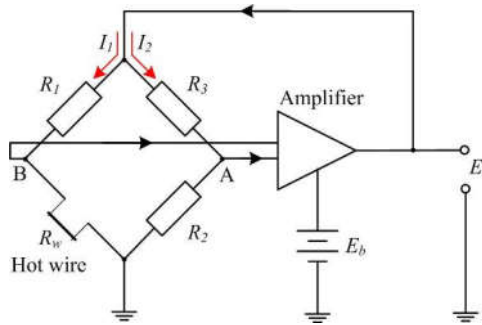
Figure 2-15: Schematic diagram of a constant temperature circuit.

The above equation is valid only if the bandwidth of constant temperature hot wire is far larger than the fluctuation frequency of the investigated flow. In the following content, the dynamic property of hot wire is analyzed. For a constant temperature circuit that has a configuration as Figure 2-15, there is

$$\begin{aligned}
E_o &= I_1(R_1 + R_w) \\
E_o &= I_2(R_2 + R_3) \\
E_i &= I_1 R_1 - I_2 R_3 + E_b \\
E_o &= A_a E_i
\end{aligned}$$
(2- 62)

where E_i is the potential difference between positive and negative terminals of the amplifier,

E_b, and A_a are offset voltage and actual gain of the amplifier. Assuming that the transfer function of the amplifier is expressed as

$$A_a(s) = K_a \frac{P(s)}{Q(s)}.$$
(2- 63)

where K_a is the gain of the amplifier; P(s) and Q(s) are polynomial expressions whose roots are the zeros and poles of the amplifier. The electrical quantities of the circuit, current on the arm I_1, I_2, and the voltage E_o, E_i are decomposed into time average and fluctuating parts. Solving the static part of Eq. (2-62), the time average current across the hot wire is obtained:

$$\bar{I}_1 = \frac{K_a E_b (R_2 + R_3)}{K_a \Delta R + \Sigma R},$$
(2- 64)

where $\Sigma R = (R_1 + \bar{R}_w)(R_2 + R_3)$ and $\Delta R = R_3 \bar{R}_w - R_1 R_2$. Combing Eq. (2-63) and the fluctuation parts of Eq. (2-62), the fluctuation part of the circuit output in the Laplace domain is obtained:

$$E_o'(s) = \frac{\bar{I}_1 K_v R_1 (R_2 + R_3) Q(s) h_c'(s)}{\Sigma R(\tau_w s + 1) Q(s) + \bar{I}_1 K_i (R_2 + R_3) Q(s) + K_a P(s) \Delta R(\tau_w s + 1) + \bar{I}_1 K_i K_a R_3 P(s)}.$$
(2- 65)

Furthermore, the transfer function of hot wire is derived from Eq. (2-65):

$$H_{CT}(s) = \frac{E_o'(s)}{h_c'(s)} =$$

$$\frac{\bar{I}_1 K_v R_1 (R_2 + R_3) Q(s)}{\Sigma R(\tau_w s + 1) Q(s) + \bar{I}_1 K_i (R_2 + R_3) Q(s) + K_a P(s) \Delta R(\tau_w s + 1) + \bar{I}_1 K_i K_a R_3 P(s)}.$$
(2- 66)

Assuming amplifier has infinitely broad bandwidth, $P(s) = Q(s) = 1$, therefore, the transfer function is degraded into a first-order system:

$$H_{CT}(s) = \frac{\bar{I}_1 K_v R_1 (R_2 + R_3)}{(\Sigma R + K_a \Delta R)\tau_w s + \Sigma R + K_a \Delta R + \bar{I}_1 K_i (R_2 + R_3 + K_a R_3)},$$
(2- 67)

which has a time constant τ_∞

$$\tau_\infty = \frac{(\Sigma R + K_a \Delta R)\tau_w}{\Sigma R + K_a \Delta R + \bar{I}_1 K_i (R_2 + R_3 + K_a R_3)}.$$
(2- 68)

Introducing the expression of $\bar{I}_1$ and K_i, Eq. (2-68) is further simplified as

$$\tau_\infty = \frac{(\Sigma R + K_a \Delta R)\tau_w}{\Sigma R + K_a \Delta R + 2\overline{R}_w(\gamma - 1)(R_2 + R_3 + K_a R_3)}, \tag{2-69}$$

where γ is the overheating ratio of the hot wire, which is equal to R_w/R_a. The cutoff frequency of constant temperature with infinite broad bandwidth amplifier is expressed as

$$f_{CT} = \frac{1}{2\pi\tau_\infty} = [1 + \frac{2\overline{R}_w(\gamma - 1)(R_2 + R_3 + K_a R_3)}{\Sigma R + K_a \Delta R}]\frac{1}{\tau_w}. \tag{2-70}$$

Since the gain of amplifier K_a is huge (the typical value is larger than 10^5), the cutoff frequency is approximated to

$$f_{CT} \approx \frac{2(\gamma - 1)K_a R_3 \overline{R}_w}{\Sigma R + K_a \Delta R}\frac{1}{\tau_w}, \tag{2-71}$$

It shows that the cutoff frequency of CT hot wire is significantly increased as compared to the CC hot wire.

2. 6. End conduction effect

For a finite length hot wire, a portion of Joule's heat is dissipated to the prongs by thermal conduction. It can result in an undesirable attenuation of the amplitude of the hot wire's response compared to an infinite long hot wire. The attenuation is frequency-dependent. Moreover, the attenuation becomes more significant when the fluctuation frequency of the turbulence is increased and the wire length is insufficient. This is the so-called end conduction effect [112]. It may lead to overestimating the bandwidth of the hot wire and causing an unexpected measurement error. Hot wire calibration is usually implemented under static or low frequency conditions, instead of applying dynamic conditions, due to the difficulty of a direct dynamic calibration. As a result, attenuation at high frequency cannot be captured by the calibration. Much attention was focused on this effect [111][66][113][114]. Figure 2-16 shows an example of the amplitude attenuation of voltage response with the fluctuation frequency, which was demonstrated by Samie [112]. Several platinum wires with different length-to-diameter ratios were heated to a constant temperature. Their amplitude of response to velocity fluctuations was reduced with increasing frequency. In the most severe case, the attenuation reached approximately 30% compared to the case without end conduction. It caused non-negligible measurement errors.
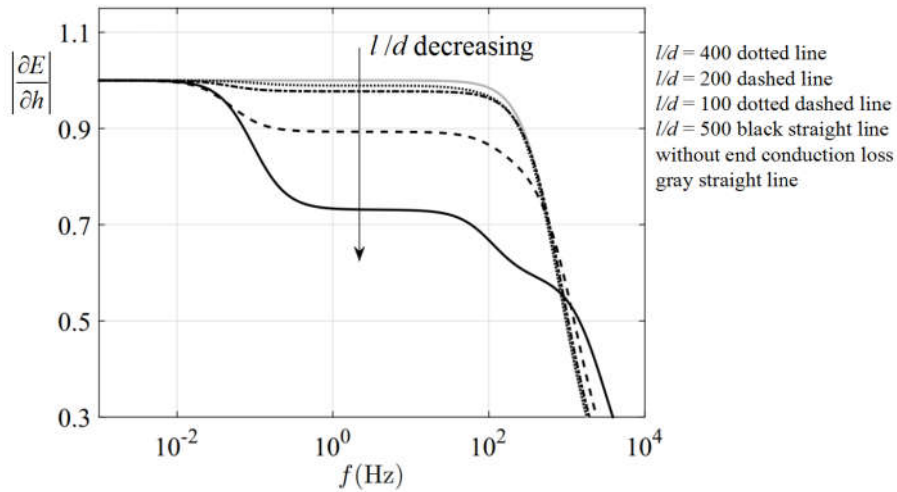
Figure 2-16: Hot wire sensitivity to velocity with different length-to-diameter ratios[112].
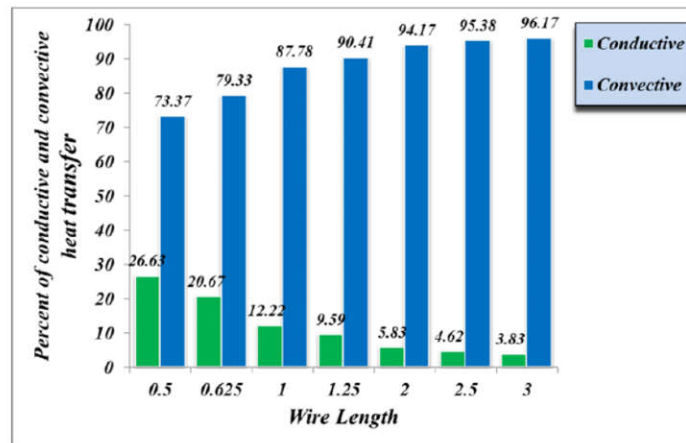

Figure 2-17: Ratios of conduction and convection with respect to wire length in mm [115].

Freymuth found that the thermal conduction effect can be ignored when the proportion of end conduction loss σ is less than 5% [82]. To minimize σ, one possible way is to reduce the length-to-diameter ratio of hot wire by extending the wire length or shrinking the diameter. While the latter will deteriorate the spatial resolution which is inversely proportional to the wire length. There is a strong motivation to shorten the wire's length to avoid the spatial filtering, especially when a hot wire is used to measure high Reynolds number flow where the velocity fluctuation is usually high and a shorter wire length is required. In addition, there is much difficulty in fabricating very fine hot wires less than 1μm diameter, due to the limited capability of convectional manufacturing techniques of a Wollaston wire. Ligrani proposed a criterion for the ratio $l/d > 200$, allowing to neglect the end conduction [33]. However, Li examined Ligrani's experimental condition and thought the criterion was only valid for platinum wires at typical velocities at atmospheric pressure [116]. Actually, σ is not

only determined by the aspect ratio but also depends on the wire material as well as on the flow and driving conditions.
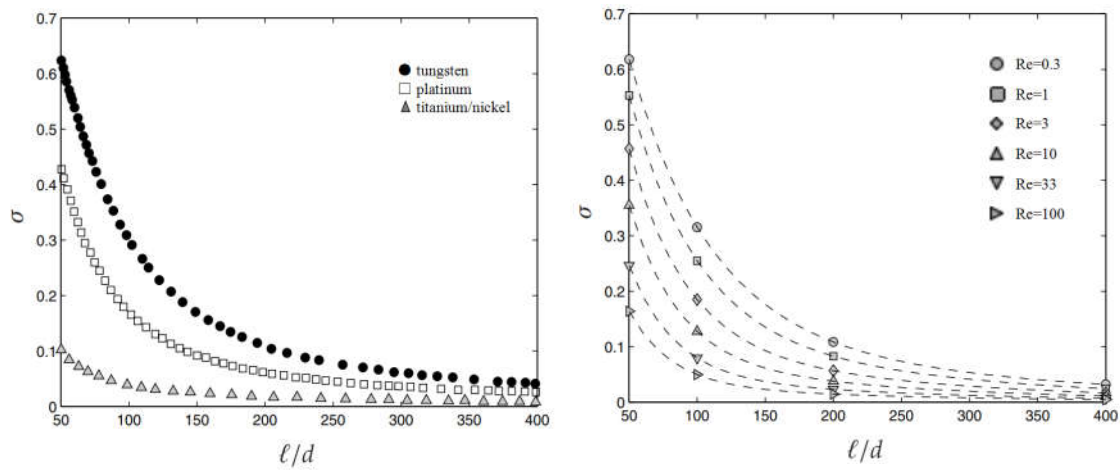

Figure 2-18: The effects of Reynolds number, wire material, and length-to-diameter ratio on end conduction σ [116].

Hultmark introduced a more effective criterion Γ to evaluate the thermal conduction, which contains all factors, and he proposed that the attenuation can be neglected if $\Gamma > 14$ [116].

$$\Gamma = \frac{l}{d}\sqrt{4\gamma(\frac{k_f}{k})Nu} \ .$$
(2-72)

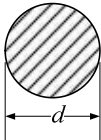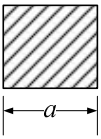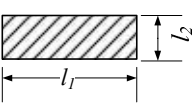# Chapter 3   Sensor Concept and Design

3.1. The concept

3.1.1. Scale effect on the time constant

As introduced in the previous chapter, time constant plays a crucial role in determining dynamic properties of hot wire sensors, regardless of whether they operate in constant current mode or constant temperature mode. Eq. (2-26) reveals how material data, geometry parameter, heat convection coefficient, and working current affect the time constant. It can be simplified by eliminating current terms,

$$\tau_w = \frac{\rho c_p A_c}{\bar{h}_c A_p} \frac{\bar{R}_w}{R_a} , \tag{3-1}$$

among these parameters, A_c/A_p is the reciprocal of the perimeter-to-surface area ratio. This ratio is analogous to the surface-to-volume ratio for a 3D object, which is related to the characteristic size and shape of the geometry. In Table 3-1, characteristic lengths and expressions of A_c/A_p for various cross-sectional shapes of hot wires are listed.

Table 3-1: Perimeter-to-surface area ratio of different 2D geometry.

Cross-section	Characteristic length L	A_c/A_p
Circle:	d	$\dfrac{4}{d}$
Square:	a	$\dfrac{4}{a}$
Rectangle:	l_1	$2(\dfrac{1}{l_1}+\dfrac{1}{l_2})$

For a prescribed geometrical shape, A_c/A_p is inversely proportional to the characteristic

length. Furthermore, the empirical expression of Nusselt number in Table 2-2 implies that reducing the characteristic size has a positive effect on the enhancement of heat convection, which shows $Nu \propto Re^m$ ($0 < m < 1$). Giving that to both Nusselt number and Reynolds number are proportional to the characteristic length, therefore, convection coefficient $h_c \propto Re^m/L \propto L^{m-1}$ In summary, combining the above mentioned effects of the characteristic size on A_c/A_p and on h, it can be concluded that reducing the wire's size can decrease the time constant,

$$\tau_w \propto L^{2-m}. \tag{3-2}$$

3.1.2. Concept of sensor

Based on this starting point of minimizing characteristic sizes to reduce the time constant, we employed micro fabricating technology, which has several unique advantages over conventional Wollaston fabrication technology. It can naturally achieve smaller characteristic line widths with relatively limited effort.

It is also capable of mass production. Many hot wires can be fabricated in the same batch process. The resultant hot wires have more identical parameters in geometry, resistivity, and temperature coefficient of resistance. Thereby, a part of calibration work can be saved. For convectional hot wire, these parameters are different and are required to be calibrated individually.

Conventional hot wire sensors are used to measure velocity vector, wall shear stress, or vorticity, as introduced in Chapter 2. Similarly, micromachined hot wires can also be configured to measure these flow quantities in the same way. Not only that, but two or more hot wires with the same or different shapes can also be integrated compactly into a single chip, which allows obtaining a better spatial resolution.

In our research, two types of hot wires were designed and fabricated by micromachining technology. The layouts of hot wires are illustrated in Figure 3-1. Figure 3-1a shows a typical single hot wire for velocity magnitude measurement, whose principle has been introduced in Chapter 2. Figure 3-1b shows double 45º hot wires that were integrated into a chip to measure the velocity angle and amplitude of 2D airflow simultaneously.
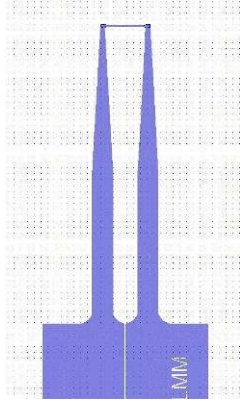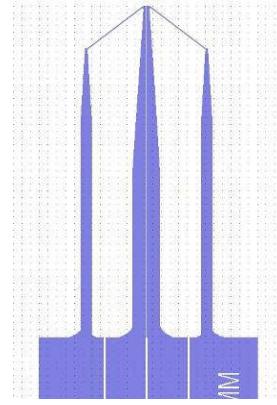
<table>
<tr><td>(a) Single hot wire</td><td>(b) Double 45° hot wires</td></tr>
</table>

Figure 3-1: Layouts of two types of hot wires of designed.

The angle of the two wires is equal to 90º. Their conducting leads are connected to one common prong, and they are isolated by a small gap. The wires have identical dimensions by design. Hence, it is reasonable to assume that they have an identical heat convection coefficient when they are placed in the flow and heated to the same temperature. The prongs of the sensor are along the streamwise direction and bi-normal to the $z-$direction, where the velocity component V_z of 2D flow is ignored. The output voltage of each circuit is denoted by E_1 and E_2, respectively. Referring to the correlation of the output of constant temperature hot wire and flow velocity that is given by Eq. (2-61), we obtain the following expressions for these two hot wires:

$$\begin{cases} E_1^{\,2} = A_1 + B_1\left(\sqrt{(V_x\sin45^\circ + V_y\cos45^\circ)^2 + k_1(V_x\sin45^\circ - V_y\cos45^\circ)^2}\,\right)^{n1} \\ E_2^{\,2} = A_1 + B_2\left(\sqrt{(V_x\sin45^\circ - V_y\cos45^\circ)^2 + k_2(V_x\sin45^\circ + V_y\cos45^\circ)^2}\,\right)^{n2} \end{cases}, \quad (3\text{-}3)$$

where A_i, B_i, n_i (i=1, 2) are the calibration constants as defined in Eq. (2-61). The velocity and flow angle can be derived by the solution of the equation group:

$$\begin{cases} V = \sqrt{V_x^{\,2} + V_y^{\,2}} \\ \varphi = \arctan\dfrac{V_x}{V_y} \end{cases}. \quad (3\text{-}4)$$
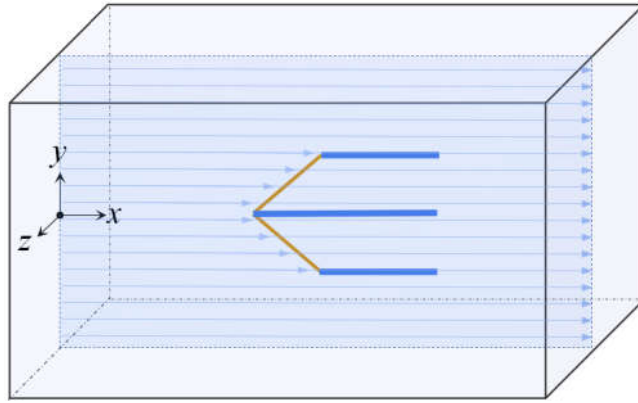
Figure 3-2: Schematic diagram of 2D velocity measurement of hot wire sensors.

3.1.3. Material and structure of hot wires

Figure 3-2 illustrates the 3D geometry of a hot wire chip. Two hot wires were integrated into it. The chip's substrate is silicon with a thickness of 500 μm. Platinum was selected as the sensing material. Platinum has an excellent linear TCR in a wide temperature range, and it can survive in a harsh environment of high temperature, or in a highly corrosive, oxidizing fluid. It also has a low thermal conductivity and a low specific heat capacity, which are beneficial in reducing the end conduction effect and reducing the time constant. Tungsten with 10% titanium (WTi) is plated on the silicon prongs to transmit an electrical signal, and it is also the material of bonding pads. Between WTi and silicon is silicon nitride, acting as the electrical isolation layer.
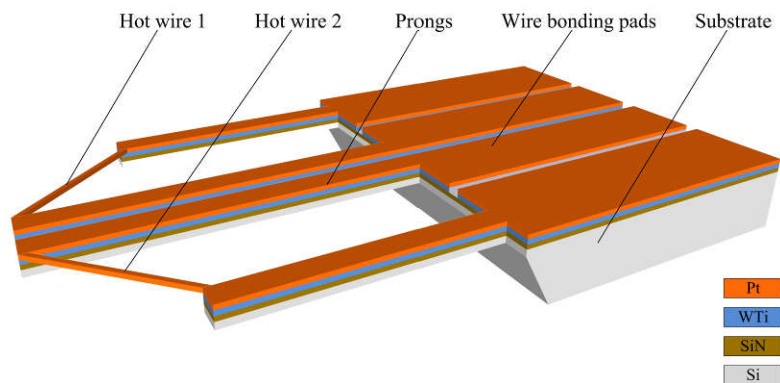

Figure 3-3: Structure of hot wire sensors.

3.2. Heat convection modeling of micromachined hot wire

As the basis of the velocity measurement of hot wire, the relation between convection and flow velocity has been introduced in Chapter 2. For a circular cross-section of thin wire, the

correlation of flow velocity and heat convection coefficient is subject to $h_c \propto V^n$ ($n\approx0.5$), which consequently determines the expression of King's law in a form $U^2 \propto V^n$ However, a hot wire fabricated by MEMS process has an approximately rectangular cross-section, which is different from circular shape of a hot wire manufactured by the conventional process, as illustrated in Figure 3-7. Hence the validation of the relations that were obtained for the circular cross-section of wire becomes questionable for rectangular ones.

Although the Nusselt number of a rectangular cross-section has been given in Table 2-2, where, the correlation seems $h_c \propto V^m$ ($m\approx0.73$). It is valid only in the large Reynolds numbers, $4\times10^3\sim 1.5\times10^4$. It is not always appropriate when the wires' dimensions are very tiny. A micromachined hot wire usually has a small Reynolds number in a vast range of flow velocities. Therefore, a correction between the convection coefficient and flow velocity is required for the micromachined hot wire.

3.2.1. Knudsen number and flow regime

The characteristic size of flow domains of interest determines the applicability of N-S equations. N-S equations are established on the continuum assumption. This regards the smallest sampling volume in the flow domain to be infinitesimal and the fluids' properties of adjacent sampling volumes, such as density, pressure, and temperature, to vary continuously. In fact, when the length scale of the volume is close to or smaller than the order of the mean free path of the fluids' molecules, the continuum assumption is no longer valid, and N-S equations break down. Fluids' properties appear to fluctuate significantly. Statistical mechanics is used to model this situation. The Knudsen number is a quantitative criterion that determines what governing laws dominate flow phenomena. It is defined as the ratio of the mean free path of molecules to the characteristic length.

$$Kn = \frac{\lambda_0}{L},$$
(3-5)

where λ_0 represents the mean free path of molecules. Depending on the Knudsen number, the flow is classified into three regimes, as illustrated in Figure 3-3.
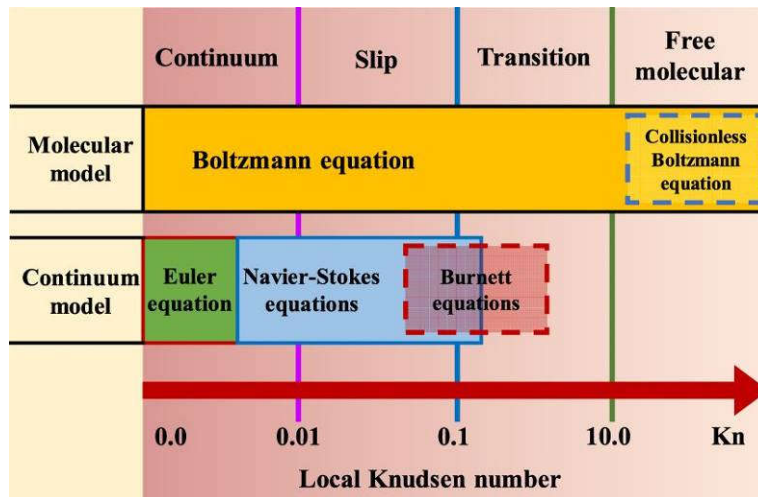
Figure 3-4: The classification of flow regime [117].

Continuum flow ($Kn > 0.01$) The characteristic size of an object of interest is far larger than the mean free path of molecules. The continuum assumption is satisfied, and the flow can be modeled by N-S equations with no-slip boundary condition.

Slip flow ($0.01 < Kn < 0.1$) N-S equations still hold in the bulk fluid, except for the Knudsen layer. This layer is a region near the solid wall within several mean free path lengths, where fluids have particular behavior different from the bulk flow. The average intermolecular distance is smaller than the average distance between molecules and the solid wall. As a result, the probability of collision of molecules and the solid wall is much larger than that of mutual collisions of molecules. The molecules in the smallest sampling volume are in nonequilibrium, continuum assumption is thereby not valid [118]. In order to model the overall flow, Maxwell's slip boundary condition instead of no-slip boundary condition is applied to N-S equations.

Transition flow ($0.1 < Kn < 1$) The characteristic size of an object of interest is in the order of the mean free path. The continuum assumption begins to break down. Statistical methods, such as Monte Carlo method and Lattice Boltzmann method, are used to simulate the fluids in this regime. Microfluidic or nano devices usually work in slip flow or transition regimes.

Molecular flow ($Kn > 10$) The characteristic size of an object of interest is far smaller than the mean free path of the molecules. The flow should be considered to consist of individual molecules. They move in straight lines, and the collision probability of intermolecular becomes negligible. Molecular flow usually occurs in ultra-high vacuum equipment or outer space.

3.2.2. Boundary treatment

It is crucial to choose the appropriate flow regime in order to simulate the flow accurately. For air velocity measurement, typical values of Knudsen number of convectional hot wire covers continuum flow to slip flow. The smallest size that we are capable of fabricating is 2 μm, which corresponds to a Knudsen number of 0.034. Hence, according to the classification of flow regime, the wire works in the slip flow regime.

Table 3-2: Typical values of Knudsen number of hot wires.

Characteristic size of hot wire	Mean free path (20°C, 1 atm.)	Knudsen number
5 μm	68 nm, air	0.0136
10 μm	68 nm, air	0.0068
25 μm	68 nm, air	0.0027

In the slip flow regime, a flow domain can be separated into two regions: bulk fluids region and Knudsen layer. Knudsen layer takes a considerable portion of the flow domain. Continuum conditions are not valid anymore. Nevertheless, the momentum exchange and energy transfer of overall flow can still be well simulated if fictionalizing an appropriate velocity on the interface between fluids and solid wall. It is called slip velocity, which is a linear extrapolation of the velocity profile from bulk fluids to the Knudsen layer (actually, only a very small slip of fluid exists on the wall). The expression of slip velocity u_s is given by Maxwell [119][120]:

$$u_s - u_w = \frac{2 - \sigma_v}{\sigma_v} \lambda_0 \frac{\partial u}{\partial y} + \frac{3}{4} \frac{\mu}{\rho T} \frac{\partial T}{\partial x}, \qquad (3\text{-}6)$$

where u_w is wall velocity and σ_v is tangential momentum accommodation coefficient. Analogue to slip velocity, it also assumes a temperature jump at the interface, which is a linear extrapolation of the temperature profile from the bulk fluid to the Knudsen layer. It is of the form

$$T_s - T_w = \frac{2 - \sigma_T}{\sigma_T} \frac{2\gamma}{\gamma + 1} \frac{\lambda_0}{Pr} \frac{\partial T}{\partial y}, \qquad (3\text{-}7)$$

where σ_T is the thermal accommodation coefficient, γ is the specific heat ratio of the
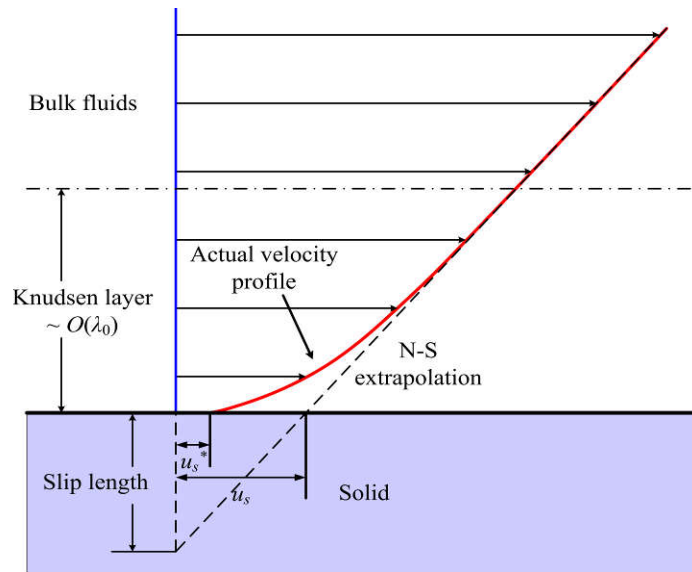
gas.

Figure 3-5: Slip velocity boundary condition.

Although velocity slip and temperature jump are fictitious, they fortuitously improve the predictive capabilities of Navier–Stokes models [121]. With slip velocity and temperature jump conditions, the forced heat convection is simulated by a commercial software package COMSOL, which employs finite element method (FEM) and integrates a slip flow module. Figure 3-6 presents the computation result of the heat convection coefficient of a hot wire under slip and nonslip boundary conditions. It shows that the differences in the convection coefficients can become considerable, especially when the wire's diameters become small. For instance, a hot wire with 10 μm diameter is operated at a flow velocity of 100 m/s. The difference of slip and nonslip condition in the heat convection coefficient is less than 3%, while, for a hot wire with 3 μm diameter, this difference is enlarged to 8%.
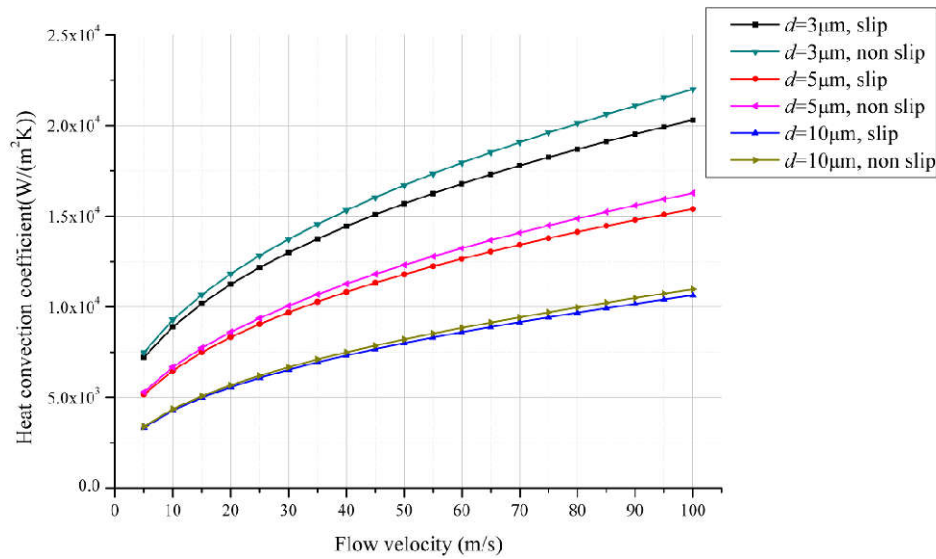
Figure 3-6: Heat convection coefficient with slip and nonslip boundary condition.

3.2.3. Geometry effect on convection coefficient

The characteristic length of an object is a perspective to analyze the effect of the object's geometry on forced convection. For a circular shape, its characteristic length is equal to its diameter, while, for a rectangular shape, there are two geometry factors to affect the convection coefficient: wire width l_1 and thickness l_2. We introduce a new parameter, the aspect ratio AR, which is equal to l_1/l_2. The dependence of the convection coefficient on the wire's width and aspect ratio were simulated by FEM with slip boundary conditions.

(a) Cross-section of conventional hot wires   (b) Cross-section of MEMS hot wires

Figure 3-7: the difference of cross-section of convectional and micro hot wires.

When logarithmic scale axes were employed to illustrate the simulation result, the relation curve of wire width and heat convection coefficient shows an apparent regularity, in Figure 3-8. Under the same aspect ratio, the resultant curves approximate a straight line, and all lines are parallel. That is to say $h \propto c_1 \cdot l_1^{c_2}$, where, c_1 and c_2 are intercepts and slopes of the straight lines, and are determined by aspect ratio and width size, respectively. Figure 3-8 shows the lines have negative slopes, $c_2 < 0$. It implies that the forced convection

45

coefficient can be rapidly increased when the characteristic size is decreased. Meanwhile, the figure shows their intersection rise with the increasing of aspect ratio. It means increasing aspect ratio can also improve the convection coefficient. We also compare the convection coefficient of a rectangle with a circular one. When $AR \geq 2$, a rectangular wire has better convection capability than a circular one.
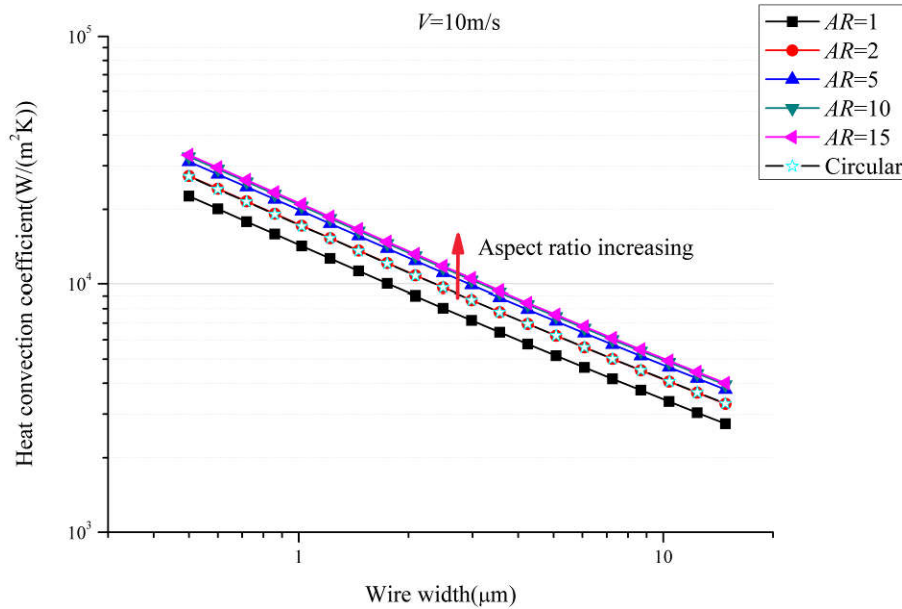

Figure 3-8: The dependence of heat convection coefficient on the wire's width and thickness.

Although increasing aspect ratio can improve heat convection, Figure 3-8 shows there is no significant difference in the coefficients for the case of $AR = 10$ and $AR = 15$. It seems that the benefits of increasing the aspect ratio in the convection coefficient become insignificant. Further simulations with higher aspect ratios at different flow velocities verified this assumption, as shown in Figure 3-9. Hot wires with 3 μm, 5 μm, 10 μm width were simulated at flow velocities of 10 m/s, 50 m/s, 100 m/s. The simulation results were normalized by dividing their convection coefficient at $AR = 1$, respectively, where it has the smallest convection coefficient. When aspect ratios are more than 10, the growth of the convection coefficient tends to be slow. It inspired us that there is no need to pursue to continuously minimize the aspect ratio to improve the convection coefficient, as long as the aspect ratio is more than about 10.
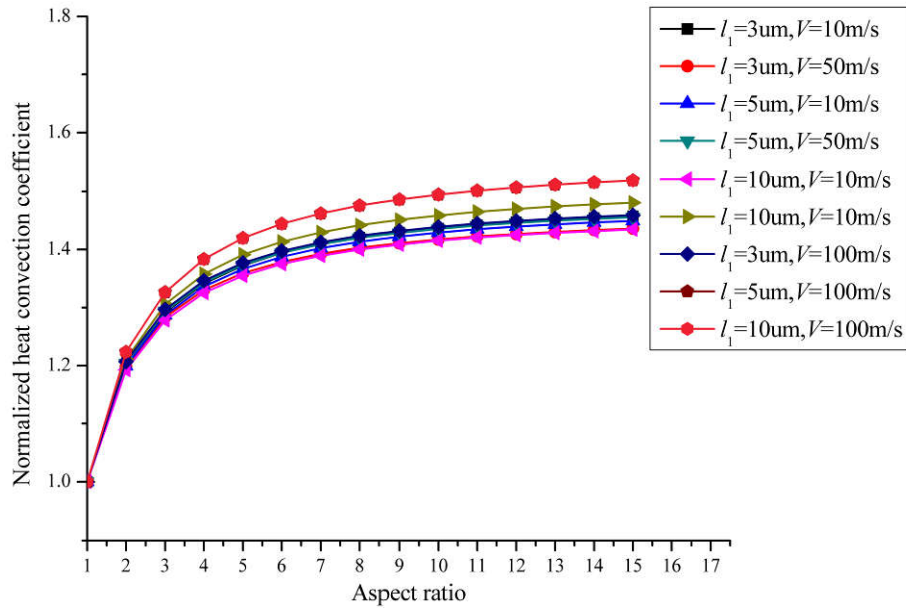
Figure 3-9: The heat convection coefficient for different aspect ratios.

3.2.4. Flow direction effect on convection coefficient

The velocity field around the conventional hot wire with a circular cross-section is regardless of flow direction. As a result, the heat convection coefficients corresponding to different flow directions are nearly identical. However, the rectangular hot wires can affect the velocity field distribution of them, as illustrated in Figure 3-10. Therefore, it gives rise to the dependence of the heat convection coefficient on the angle.
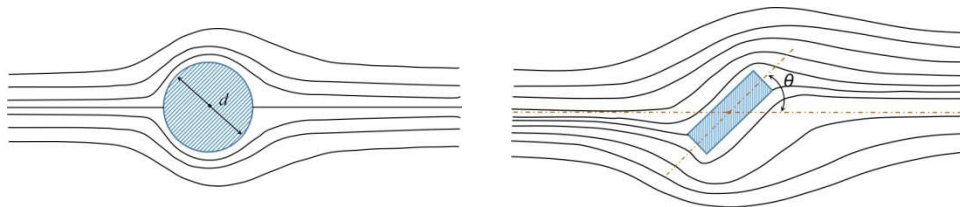

Figure 3-10: Schematic streamlines of hot wires with a circular or rectangular cross-section.

The angle between the reference line (width direction) and the incoming flow is noted as the flow angle θ. The dependence of the convection coefficient on θ was investigated by simulating the convection coefficient at flow angles of $0°-90°$ at a constant flow velocity of 10 m/s. The results are shown in Figure 3-11. The obtained values of the coefficients are normalized by dividing through the maximal coefficient, which corresponds to the values at the flow angle of $0°$. Figure 3-11 shows that the flows which are normal and bi-normal to hot wires always have the largest and smallest coefficient, respectively.

Comparing the wires at different aspect ratios of 10, 16, and 33, the smallest aspect ratio gives the least variation of convection coefficient when the flow angle varies from 0° to 90°. Meanwhile, comparing the wires at different widths of 3 μm, 5 μm, 10 μm, the smallest width also has the smallest fluctuation. It seems that both reductions in width and aspect ratio can diminish the dependence of the coefficient on the flow angle. In addition, one should be aware that a 3 μm wide wire, even with an aspect ratio of 33, has less variation of the coefficient than the 5 μm or 10 μm ones with an aspect ratio of 10. It implies that the dependence of convection coefficient on flow angle can be more effectively reduced by width deduction.
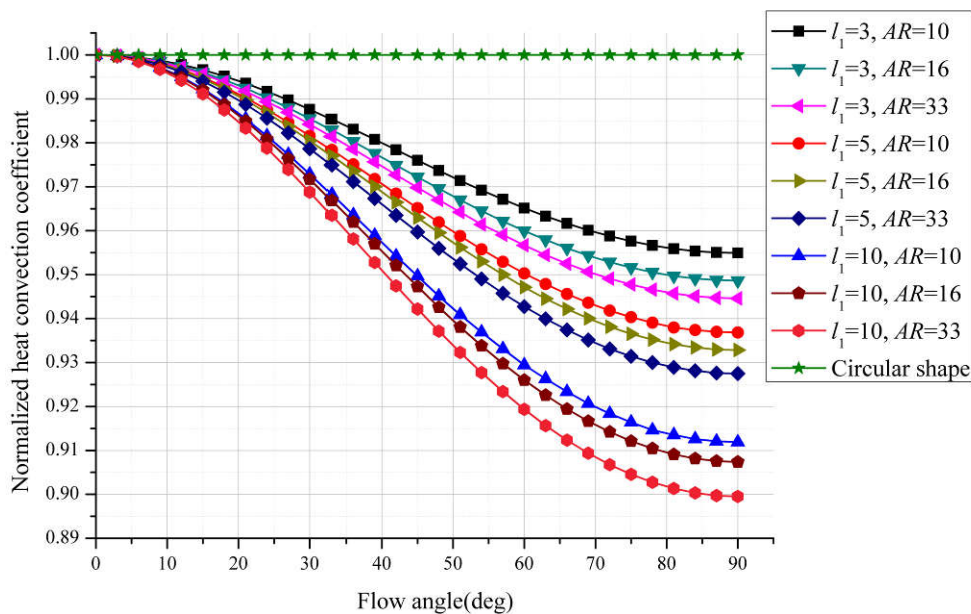

Figure 3-11: The relation of heat convection coefficient and yaw angle of flow.

3.2.5. Correlation of heat coefficient and flow velocity

The Figure 3-8 illustrates at a fixed flow velocity the relation between width, aspect and convection coefficient. When flow velocity is changed, the resultant convection coefficient of a prescribed geometry is also varied. As shown in Figure 3-12, forced heat convection of hot wires with 3 μm, 5 μm, 10 μm at aspect ratio of 15, 10, 5 were simulated at velocities from 1-100 m/s. Their resultant curves were fitted by a sample curve, $\lg(y - c_3) = b\lg x + a$. The fitted lines show very good linearity under logarithmic axis. Note that, all values of the coefficient in Figure 3-9 have been offset by different constants c_3 before they were fitted. The slope of the fitted lines is approximate to 0.47, which means the relation between

convection coefficient and flow velocity can be expressed in the form $h_c \propto V^{0.47}$. It implies that the rectangular hot wire may also comply with King's law as the circular hot wires.
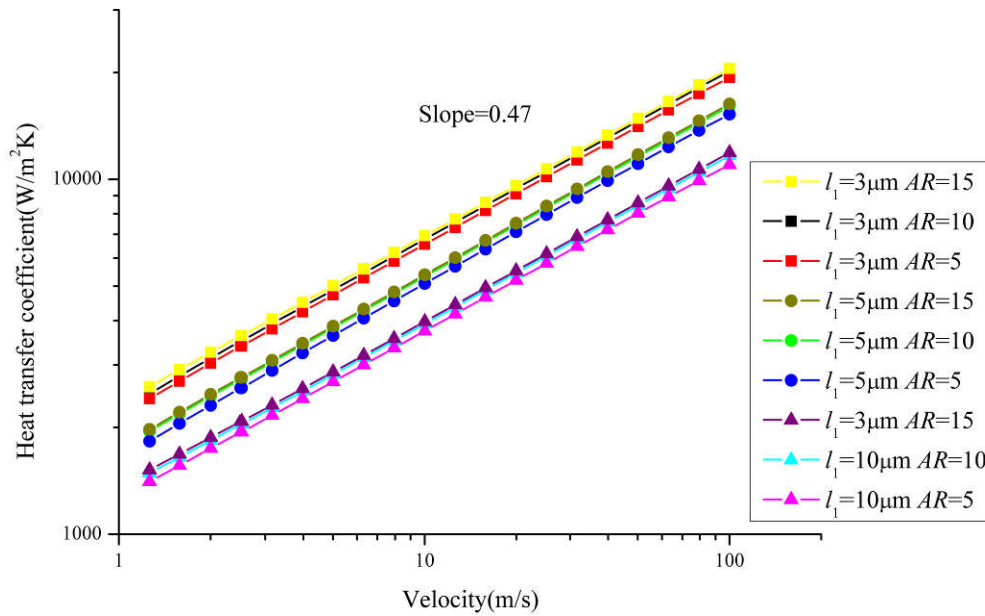

Figure 3-12: Heat convection coefficient varying with the flow velocity.

3.3. Modeling of constant temperature hot wire

The heat convection of micromachined hot wire has been discussed in the previous section. In this section, the focus is to quantify the correlation between flow velocity and voltage output of CT hot wires by numerical modeling.

3.3.1. Modeling methodology

Multiple and coupled physics indeed govern the behavior of CT hot wire. It is obviously impractical or costly to create a full dimension model and simulate it in the full coupled physics. Alternatively, we create a low dimension model and segregate the simulation into multiple steps: (1) Solving heat convection between fluid and solid; (2) Solving Joule heating; (3) Simulating constant temperature control. All simulations are implemented in finite element method software, COMSOL.

In the first step, the heat convection coefficient needs to be solved. When end conduction losses and interference of prongs on the flow field are ignored, then the distribution of temperature and velocity along the hot wire's length direction are homogeneous. Hence, heat convection coefficients along the length are regarded to be identical. The heat

convection problem in three dimensions can be simplified to a 2D conjugated heat transfer simulation. It can significantly reduce computational time. Once the coefficient is obtained, the resultant coefficient is input to the Joule heating model. In the Joule heating simulation, the driving current that heats the wire to its working temperature is required to be solved. A 1D line model was used to represent the hot wire. Since the Biot numbers of hot wires are far smaller than 0.1, the temperature gradients inside the cross-section can be neglected, and the temperature only varies along the hot wire's length direction. The governing equation of a 1D Joule heating model is indeed Eq. (2-12). It describes the relationship between the hot wire's temperature and the heating current.
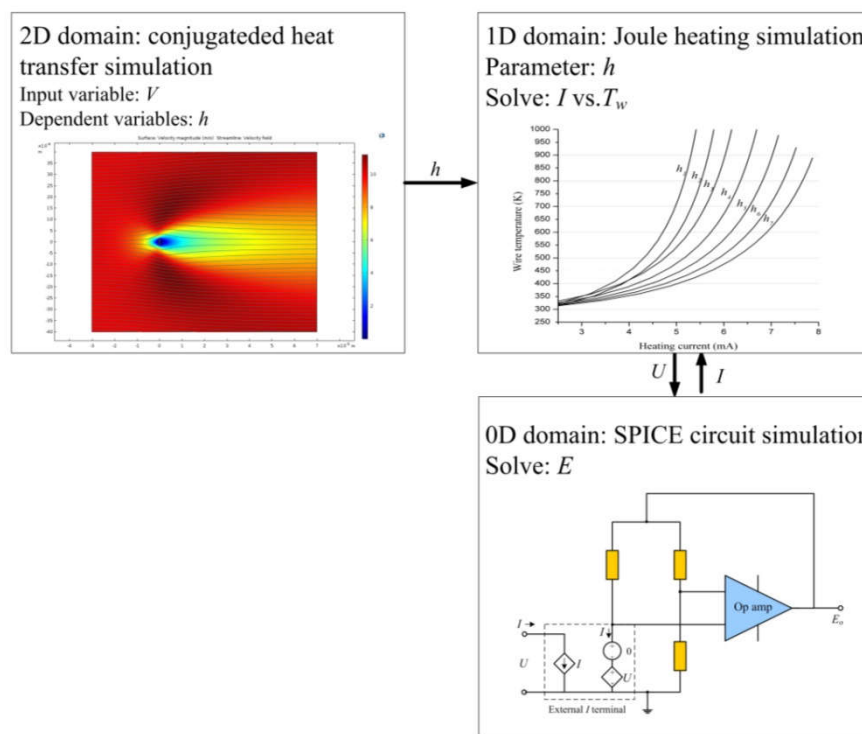

Figure 3-13: Schematic diagram of multiphysics simulation of CT hot wire sensor.

If the output of a CT circuit is required to be estimated, then the hot wire and the temperature control circuit are simulated together. The circuit can be defined by a netlist file and simulated by SPICE program, which is already integrated into COMSOL. The circuit is comprised of a Wheatstone bridge, a first-order operational amplifier, and an "external I terminal" device. The device in COMSOL assigns a voltage measured from outer modeling (here, it measures the voltage drop of a current source for heating hot wire in the Joule heating modeling) to the controlled voltage source in the circuit modeling. The resultant current across the voltage source is coupled back to Joule heating modeling as the

prescribed current source. Thereby, an interactive coupling between the two models of Joule heating and temperature control are established.

3.3.2. Time constant

3.3.2.1. Geometry effect

Eq. (3-1) gives an expression of time of hot wire, which describes how perimeter-to-surface area ratio and convection coefficient determine the time constant. The subsequent analysis hinted that the geometry of hot wire, especially the wire's width, can affect convection coefficient and time constant. Figure 3-14 shows the time constant of several hot wires with different width and aspect ratios. They are simulated in the air with a velocity of 10 m/s. The simulation results indicate a relation of $\tau_w \propto c_4 \cdot l_1^{c_5}$, where c_4 and c_5 are positive constants. They are the intercepts and slopes of the inclined lines in Figure 3-14. The simulation results echo previous analyses of the relation between time constant and characteristic size, $\tau_w \propto L^{2-m}$ (accordingly, $2 - m = c_5$).
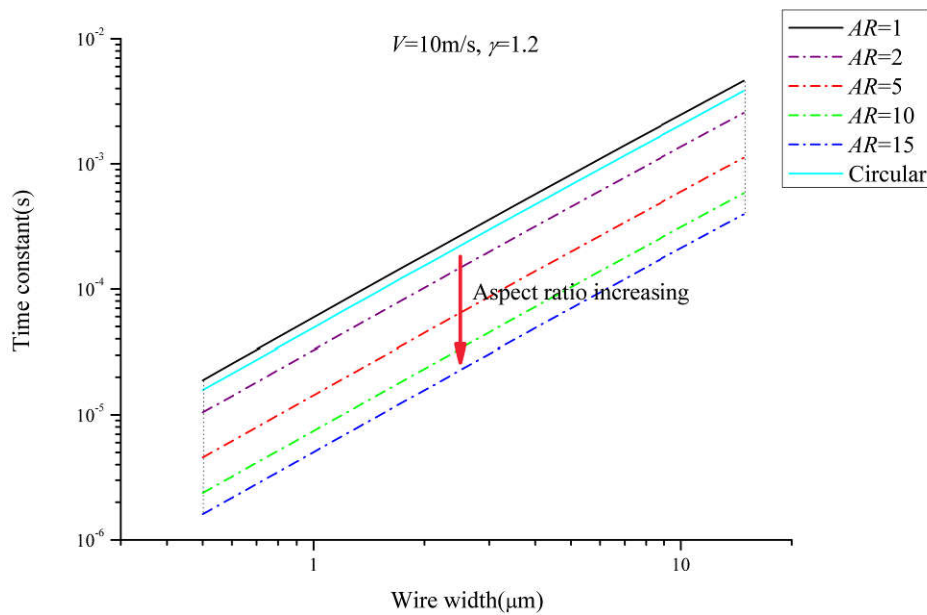

Figure 3-14: Geometry effect on the time constant of hot wires.

3.3.2.2. Flow velocity effect

Since the convection coefficient is increased when averaged flow velocity rises, the time constant is reduced according to Eq. (3-1). The time constants of 300 nm thick Pt wires with different width were also simulated. An overheating ratio of 1.2 was assigned to them, and

the flow velocity is varied from 5 m/s to 100 m/s. Figure 3-15 presents simulation results of the time constant. It shows the time constants of a few hot wires with small width can reach less than 50 μs, and the time constant is further reduced when the flow velocity is increased.
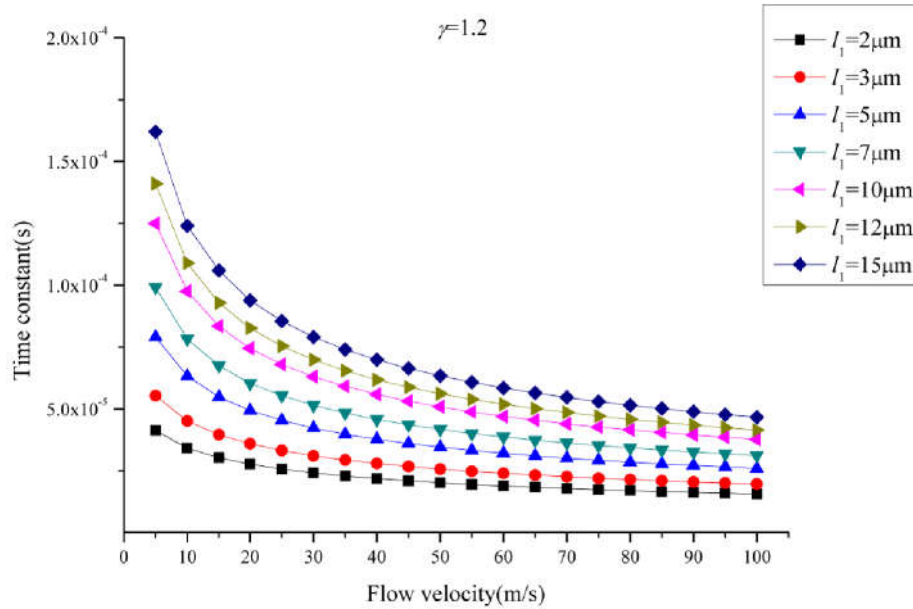

Figure 3-15: Time constants of hot wires at different flow velocities.

3.3.3. Output voltage

The output voltages of CT circuit connected to several alternative hot wires have been simulated. These wires have the same thickness of 300nm, but different length and width. They are assumed to be operated at an overheating ratio of 1.2 and $R_1 = R_2 = R_3$ for Wheatstone bridge. Airflow ranges from 5 m/s to 100 m/s. The simulation results are illustrated in Figure 3-16. It shows the output voltages of these wires are in the range of 0.1 V to 7 V. This range can be driven by a regular operational amplifier. Moreover, the square of the output voltage is approximately proportional to 0.5 times of flow velocity. It implies King's law might still be in effect for the micromachined wires with a rectangular cross-section.
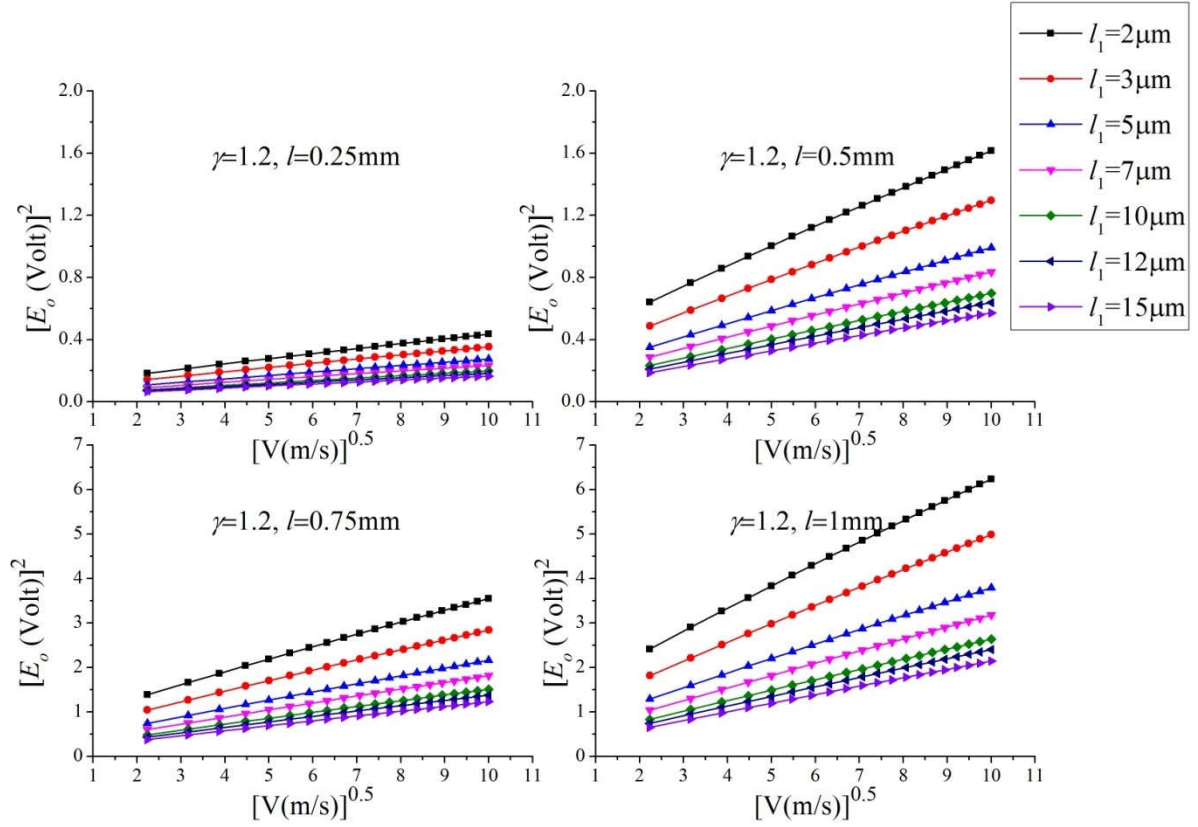
Figure 3-16: The output voltage of CT circuit at different flow velocities.

When a hot wire is operated in constant temperature mode, the output voltage of CT circuit is expressed by Eq. (2-60). Usually, ambient temperature is set to 20 ℃; for a platinum material, its TCR is 0.00385 /℃. Hence, $R_a \approx R_0$. With necessary substitution, Eq. (2-60) can be simplified as follows:

$$E_o \approx l \sqrt{\frac{h_c A_p \rho_0 \gamma (\gamma - 1)}{A_c \alpha}} \cdot \frac{R_w + R_1}{R_w}, \qquad (3\text{-} 8)$$

It shows the wire length l, the perimeter-to-surface area ratio A_p/A_c, and the resistance configuration of Wheatstone bridge's arms can affect CT circuit output. The geometry effect on the output of the designed hot wires is simulated by the modeling methodology as mentioned. Figure 3-17a presents the effect of the length of hot wires. They are assumed to be operated at an overheating ratio of 1.2, and Pt thickness is 300 nm. It shows the voltage is almost linearly increased with the wire length. Figure 3-17b illustrates the effect of the width and aspect ratio of hot wires. They are assumed to be run at the same overheating ratio. Airflow speed is fixed at 10 m/s, and Pt wire length is 1 mm. It shows that reducing wire width or increasing aspect ratio will raise the output of CT circuit.
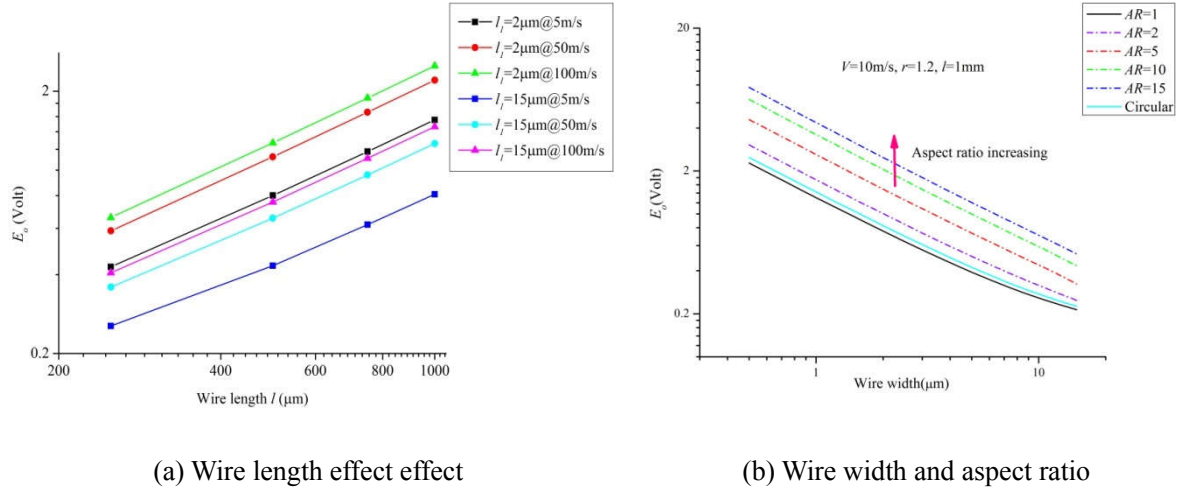
| (a) Wire length effect effect | (b) Wire width and aspect ratio |

Figure 3-17: Hot wire's geometry effect on the output voltage of CT circuit.

3.3.4. End conduction loss of micromachined hot wire

It should be noted that the line that represents the voltage result of a 15 μm wide hot wire at 5 m/s in Figure 3-17a (the blue line) has a little deviation from a straight line. It implies that the voltage of hot wire is not always linearly reduced with the decreasing of the wire's length. The end conduction loss may result in it. Eq. (3-8) is based on the assumption that the end conduction loss is ignored. To distinguish the voltage U and resistance R_w that were derived under the assumption of ignoring end conduction loss, voltage and resistance with loss are denoted by U_{loss} and $R_{w,loss}$. Their power consumption ratio is of the form

$$\frac{U_{loss}^2/R_{w,loss}}{U^2/R_w} = \frac{h_c A_p l(R_{w,loss}-R_a)/(1-\sigma)}{h_c A_p l(R_w-R_a)} .$$
(3-9)

When the circuit is working in constant temperature mode, regardless of how much end conduction ratio is, Wheatstone bridge always tends to be balanced, in which the resistance of a hot wire is almost equal to γR_a. That is $R_{w,loss} = R_w = \gamma R_a$. Thus, Eq. (3-9) is simplified to

$$\frac{U_{loss}}{U} = \frac{1}{\sqrt{1-\sigma}} .$$
(3-10)

It shows the end conduction loss ratio σ plays a critical role in determining the voltage ratio. When σ is increased, the voltage difference with/without end conduction loss is enlarged. To mitigate the end conduction effect, the percentage of end conduction loss in the total

transferred heat, σ, should be reduced [82][114]. The empirical formula of conduction loss ratio that is proposed by Hultmark can not be applied to evaluate non-circular hot wires [116]. Recalling the expression of conduction and convection of hot wires, the conduction loss ratio is simplified to

$$\sigma = \frac{1}{\gamma} \cdot \frac{\tanh(0.5l/l_c)}{0.5l/l_c}, \qquad (3\text{-}11)$$

where l_c is the cold length that has been mentioned in Eq. (2-15). According to the definition of l_c, it is a function of the parameter I, h, A_p/A_c, k_w, and $\rho_0\alpha$, which are related to a hot wire's operation condition, geometry, and material properties. Eq. (2-15) shows σ is a hyperbolic function of $0.5l/l_c$. Hence, it is difficult to establish a brief expression between σ and these parameters. Nevertheless, at least some qualitative relation can be obtained by the modeling methodology as mentioned above. We estimated the end conduction ratios of several Pt hot wire alternatives, and their simulation results are presented in Figure 3-18.
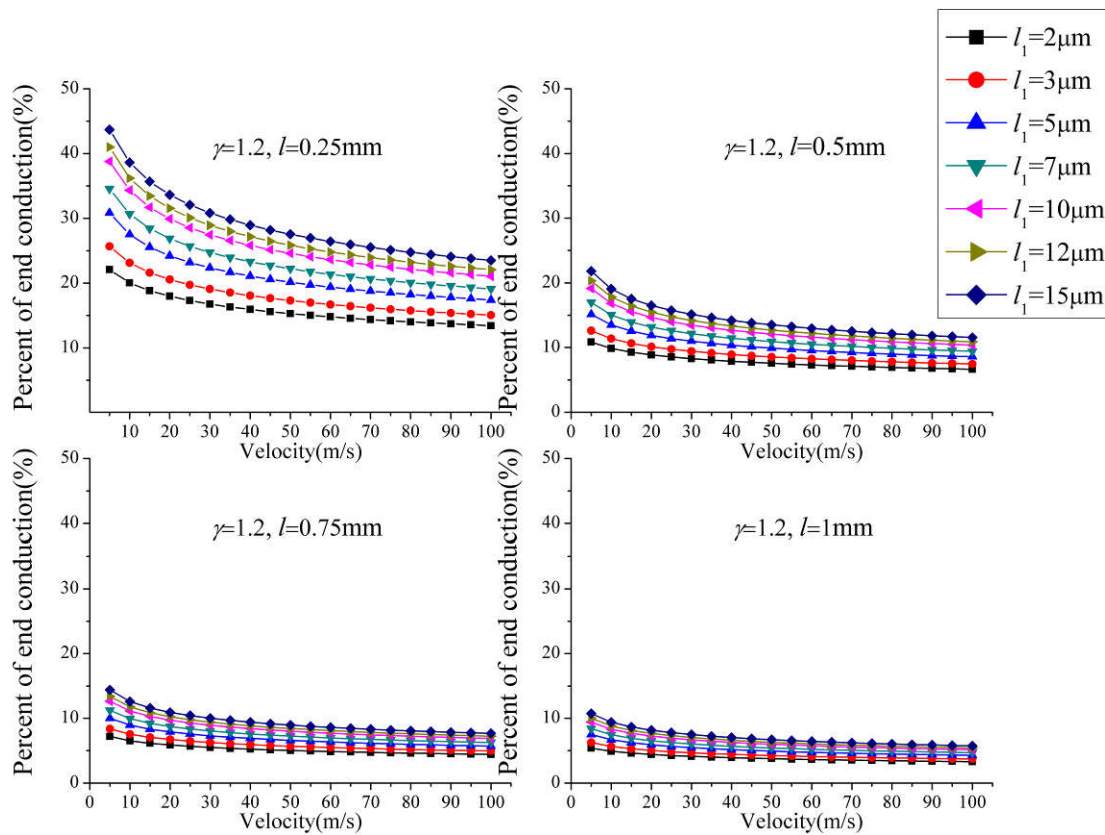

Figure 3-18: End conduction loss ratios of hot wires with different width at different flow velocities.

It shows σ is reduced with the increasing of flow velocity and with the decreasing of with

width. Note that the end conduction loss can be reduced more effectively by increasing the wire length. On the other hand, it will cause a reduction in spatial resolution in return. Hence, a feasible way to reduce end loss conduction is to reduce the wire width.

Chapter 4 Fabrication of hot wire sensors

The benefit of reducing characteristic sizes of hot wire sensors on improving their dynamic response has been discussed in the previous chapters. In our work, MEMS manufacturing technology is used to achieve such small characteristic dimensions.

4.1. Conventional Wollaston technology for thin wire fabrication

Many methods have already been invented for reducing hot wire dimensions. The most representative manufacturing method is the Wollaston process [122], which is named for employing a so-called "Wollaston wire" as the starting material of the hot wire. This invention was made by the English scientist Wollaston already at the beginning of the 19th century. The thin wire is obtained by combining a metal core with a cladding layer. Pt or other metals with temperature sensing function are selected as the core material, and silver or other metals with a good ductility are selected as the cladding material. When a Wollaston wire is stretched in its longitudinal direction, its core will be stretched simultaneously. Thus, the diameter of the core can be reduced substantially. Due to the protecting by the cladding material, the core can be extended very long, and its diameter can become very thin without breaking. The core will be exposed to air acing as a hot wire when some part of the cladding is selectively removed by chemical etching [123][124][125].

Although Wollaston technology has been widely used to fabricate hot wires for several decades, the thinnest dimension that has been achieved so far is limited to 0.65μm [126]. Challenges are encountered when a smaller geometrical size of hot wires is desirable, or several hot wires need to be integrated into one sensor.

4.2. The basic techniques of manufacturing MEMS

Many different kinds of innovative sensors and actuators manufactured by MEMS technology are widely applied in consumer electronics, automobiles, life science, etc. [127], which proves the potential of this manufacturing technology in minimizing the dimensions of a device. MEMS manufacturing technology is evolved from process technology in semiconductor devices. The basic techniques are film deposition, lithography, and material etching.

4.2.1. Film deposition

The fabrication of MEMS devices usually involves several steps of thin film deposition. Various materials are homogeneously deposited on a substrate, with film thicknesses varying from several nanometers to tens of micrometers. These films serve as a conductive layer, dielectric layer, diffusion barrier layer, or as a hard mask for a subsequent etching step. There are two main types of deposition processes: physical vapor deposition (PVD) and chemical vapor deposition (CVD).

In PVD, materials' vapor is taken off from its target by a physical mechanism, such as evaporation, the bombardment of electrons, ions, or photons. In manufacturing our hot wire sensors, two films, Pt and WTi, were deposited by magnetron sputtering deposition, which is one of the typical PVD. A schematic diagram of the magnetron sputtering is shown in Figure 4-1. Argon acting as chemically inert (noble) working gas is filled in a vacuum chamber, in which two parallel electrodes are placed. When the electrodes are connected to a DC or RF source, plasma can be generated by DC or RF glow discharge, and the plasma density is enhanced by the external magnetic field. The sheath voltage is able to accelerate the positive Ar ions to bombard an object, which is the potential difference existing between bulk plasma and any object immersed in plasma. By properly configuring: the relative area size of two electrodes, source amplitude, and frequency, the voltage on the cathode side can reach very high values so that the energy of the bombarding ions can cause the ejection of atoms from the target surface. These atoms go through the bulk plasma and arrive at the substrate. In the process of migration, nucleation, and growth, the atoms form a thin layer on the substrate.
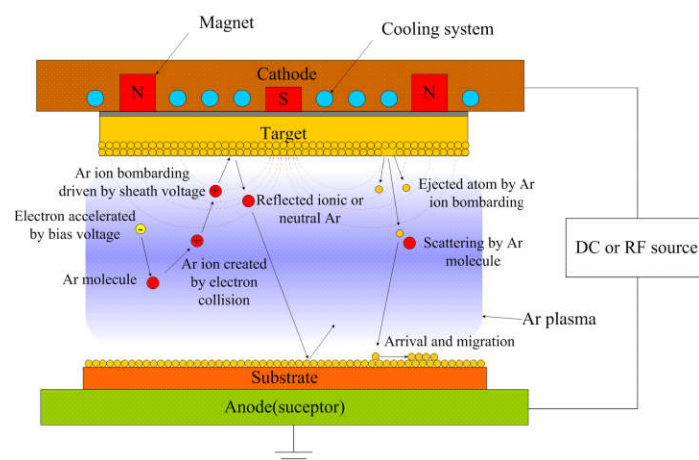

Figure 4-1: Schematic diagram of magnetron sputtering.

In CVD, the deposited material is synthesized by the chemical reaction of volatile precursors or the reaction of precursors and substrates. The hot wire sensor utilized one typical CVD, plasma-enhanced chemical vapor deposition (PECVD) process, to produce SiN_x as hard mask layers for subsequent etching. The basic construction of a PECVD machine consists of a heated susceptor and a gas distributor, which acts as the bottom and top electrodes, respectively. The silane and ammonia gas are mixed and filled in the process chamber. When an RF electrical field is applied between the two electrodes, the gas mixture decomposes into the plasma state, generating various highly reactive intermediate species. Some of these species produce nitride by complex chemical reactions [128]. At the same time, volatile byproducts and other species that are not involved in the reaction are pumped out.
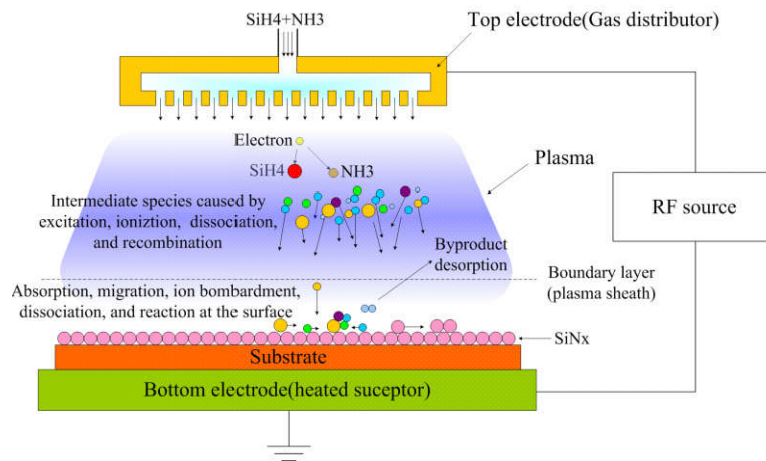

Figure 4-2: Schematic diagram of a PECVD deposition for nitride.

4.2.2. Lithography

Lithography is the most critical process for downscaling patterns. The spatial resolution of lithography determines the minimum critical size of MEMS devices. It uses photoresist (PR) and photomasks. A photoresist is a photosensitive material that changes its solubility in a developer after being exposed to UV light at some specific optical wavelength. A typical photomask is a quartz plate, which has been partially coated by chromium patterns that represent the 2D layout of the intended device. After selectively exposing the photoresist (PR) through a photomask, the exposed and unexposed PR exhibit significantly different chemical resistance to the developer. When being immersed in a developer, the soluble part is thereby removed. It is capable of producing very fine photoresist features on the substrates. The shapes of those features are almost exactly similar to the patterns that have

already been defined in the photomask. These resultant patterns act as temporary masks to protect the underlying layers from subsequent etching. A complete lithography process goes through the following steps:1) coating thin PR film on a substrate by spinning; 2) baking the film to remove solvent; 3) exposure; 4) removing the undesired part of PR by developing; 4) stabilizing the PR patterns by hard baking; 5) checking patterns, as illustrated in Figure 4-3.
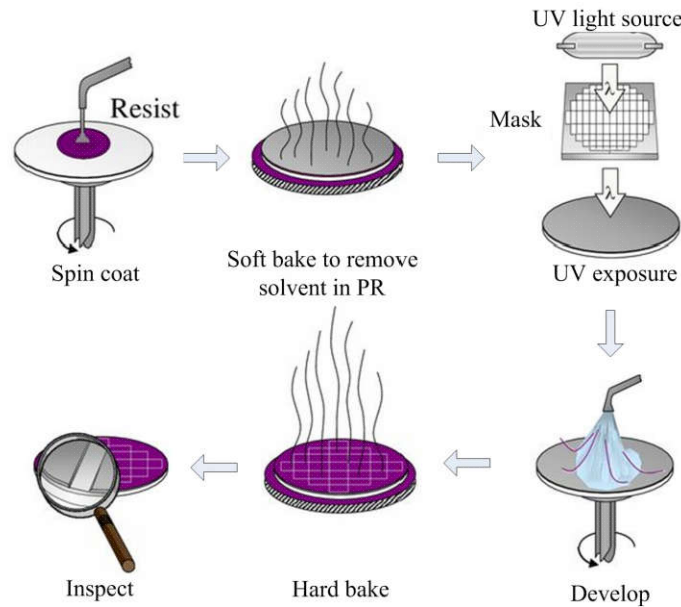

Figure 4-3: Lithography procedure.

There are two different types of PR: negative tone PR and positive tone PR. The former becomes insoluble while the latter gets soluble after exposure, which will result in two different PR profiles after development, as shown in Figure 4-4. It should be noted that an inverse trapezoidal profile is formed at the opening area of negative PR, while, a trapezoidal profile corresponds to positive PR. The reason for the inclined sidewall is that the light received by the top of PR is more than the bottom in the presence of PR absorbance.
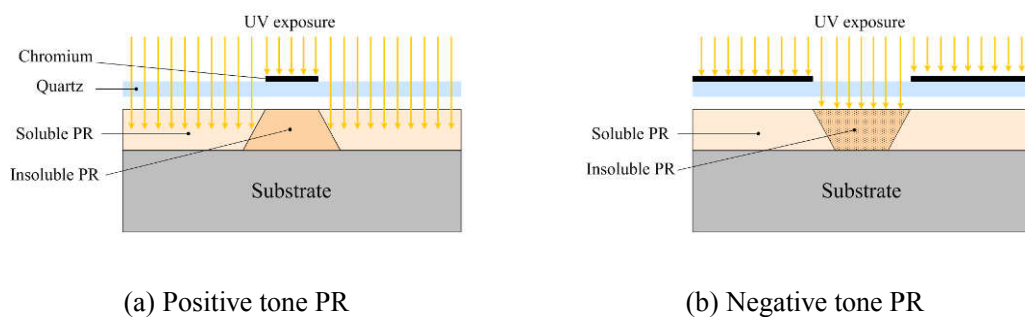

(a) Positive tone PR   (b) Negative tone PR

Figure 4-4: Positive and negative tone photoresist.

4.2.3. Etching

Etching makes use of chemical reaction or physical attack to remove the undesired part of the deposited films or the substrate, where there is no protection of photoresist or hard mask. There are two basic categories of etching: wet etching and dry etching. For the former, the solution of the etchant is involved in the chemical reaction, and the product is solvable; for the latter, corrosive vapor or plasma is involved, and the products are volatile.

In wet etching, generally, several steps take place: 1) The etchant flux is transported through a boundary layer to the surface of the target material in the opening region by convection, diffusion, or an electric field; 2) the surface reacts with the etchant (absorption, chemical reaction, desorption); 3) the product species are transported away by convection or diffusion, the circulation of these processes is thus sustained. The slowest step among them is called the rate-limiting step, which determines the overall etching rate.
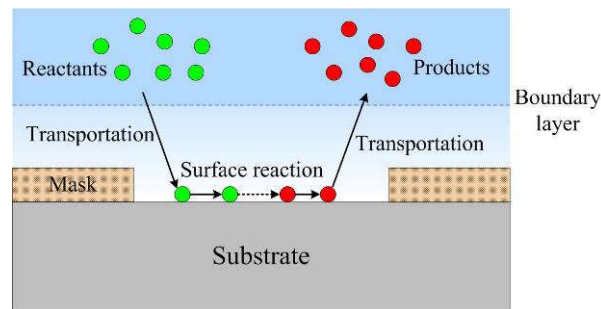

Figure 4-5: Basic processes in wet etching.

The rate of an actual etching is determined by many factors, such as etchant concentration, stirring, temperature, surface adsorption, and condition of target film. Among them, the temperature has a very significant effect, which usually follows Arrhenius law:

$$r = r_0 e^{-E_a/R_g T} \tag{4-1}$$

where r_0 is a rate constant that depends on the collision frequency of each reaction; E_a is the activation energy, and R_g is the universal gas constant. The parameters above are usually obtained by fitting actual experimental data of etching rate and temperature. After wet etching, the possible profiles of the target material are illustrated in Figure 4-6, which correspond to two different etching modes, so-called isotropic and anisotropic etching, respectively. For the former, the etching rates in all directions of the target material are equal. It usually produces rounded sidewalls where undercutting occurs. For the latter, the etching

rates are orientation-dependent, the undercutting is usually negligible.

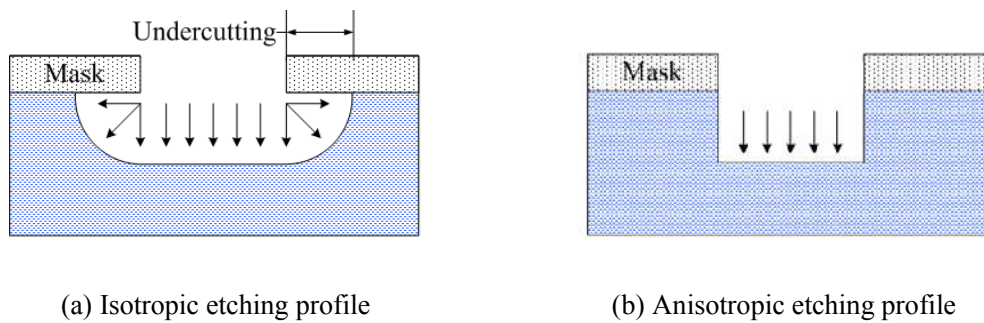(a) Isotropic etching profile   (b) Anisotropic etching profile

Figure 4-6: Isotropic and anisotropic etching profile

When the surface reaction is the rate-limiting step, the etching rate is very likely to be sensitive to surface orientations [129]. Some specific crystallographic orientations of target material exhibit a more rapidly etching rate than others.

Dry etching also experiences similar steps as wet etching: etchant transportation, surface reaction, and product transfer. Emphasis is given to plasma dry etching, which is an important process for micromachining. In plasma dry etching, free radicals and positive ions are generated. The chemical properties of free radicals are active and react with the target material. The transportation of the free radicals from bulk plasma to the opening surface is almost unidirectional, which may result in isotropic etching. Positive ions are used to realize physical etching. Accelerated by sheath potential or a bias voltage, the positive ions in the plasma sheath bombard the surface of the target material. The incident energy of these ions can be increased to high values so that the bombardment sputters the target material away. The incident angle is typically almost vertical to the substrate. Not only giving rise to physical etching, but the ions' attacks are also able to enhance chemical etching rate on the incident surface (the possible mechanism is explained that highly energetic ions damage the surface or promote byproduct removal). The sheath potential or bias voltage can be artificially increased so as to make the total etching rate dominant in the vertical direction, which will result in an anisotropic etching profile, as illustrated in Figure 4-7a. In order to reduce the etching on the lateral wall, some plasma dry etching process introduces extra gases, for instance, chlorofluorocarbon, to promote the formation of polymer inhibitor on the lateral wall during etching, as illustrated in Figure 4-7b. These polymers substantially lower the lateral etching rate and result in more vertical sidewalls.
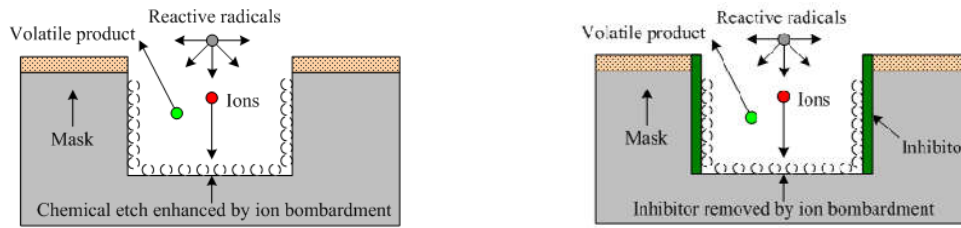
(a) Isotropic radicals etching and ion enhanced etching in a vertical direction.

(b) Lateral passivation and ion enhanced etching in a vertical direction.

Figure 4-7: Two types of anisotropy mechanism of plasma dry etching.

The basic techniques of MEMS manufacturing processes have been introduced above. Unlike conventional CMOS devices, the process steps for different MEMS devices are often unique and remain an art of techniques to some extent, which closely depends on the employed materials system and structures of intended devices, as well as on the designers' experiences. In the following sections, the fabrication process of Pt wire and the prongs will be presented, respectively.

4.3. Fabrication of Pt wire

In this section, we focus on the patterning techniques of a Pt film and on the manufacturing process of a freestanding Pt wire based on these techniques.

4.3.1. Patterning techniques of Pt layer

For patterning a metal layer of a MEMS device, the combination of single lithography and etching is a practical and universal approach. Lithography is used to create the photoresist mask on the metal layer, and the subsequent etching process is used to remove the unwanted metals. However, Pt is a noble metal rather inert in chemical reactions, which results in some difficulties in its patterning.

4.3.1.1. Wet etching of Pt

Some researchers use hot aqua regia to etch Cr/Pt/Ti layers [130], which is an aggressive solution mixed by nitric acid and hydrochloric acid in a molar ratio of 1:3. Cr is used as a hard mask that can resist aqua regia, and Ti is employed as an adhesion layer of Pt to the substrate. Unfortunately, since the vertical etching rate of Pt is significantly smaller than the

lateral rate, the undercutting of a sidewall of Pt is unacceptable for some applications that require a very narrow linewidth of Pt patterns. Two modified methods have been figured out to accelerate the vertical etching rate: plasma treatment and diffusing impurities [131][132]. In the former, the Pt in the region covered by mask is treated by Ar plasma. Thus its surface energy state is activated, which can increase Pt etching rate in aqua regia. Meanwhile, the Pt in the uncovered region is not exposed to Ar plasma. Thus, its etching rate is not changed. This method is applicable to etch thin Pt layer due to the limitation of penetrating depth of Ar plasma in Pt film. In the latter method, Ti or Al film is deposited on the top of Pt layer and annealed. Ti atoms are thereby diffused into Pt to form a Pt-Ti or Pt-Al alloy, which has a relatively higher etching rate than pure Pt film. It can reduce lateral etching, but the alloys have lower TCR than pure Pt.

4.3.1.2. Dry etching of Pt

Dry etching is a regular alternative to pattern Pt [133]. Typically, chlorine and Ar plasma are employed in this process. The active free radicals in chlorine plasma are able to chemically react with Pt and produce nonvolatile $PtCl_x$. The accumulation of the nonvolatile product in the reaction surface tends to retard etching. Ar plasma is added to remove $PtCl_x$ by sputtering effect of Ar ions. One challenge of Pt dry etching is a low etching rate and low selectivity of Pt to PR or hard mask. Physical sputtering is the rate-limiting step of the etching process. Although the etching rate can be improved by increasing the sputtering power of Ar, it will rapidly sputter PR or hard masks as well. Another challenge is ear-like, or fence residues that appear at the pattern edge [134][135], as presented in Figure 4-8. It is caused by the redeposition of Pt on the sidewalls of photoresist or hard mask.
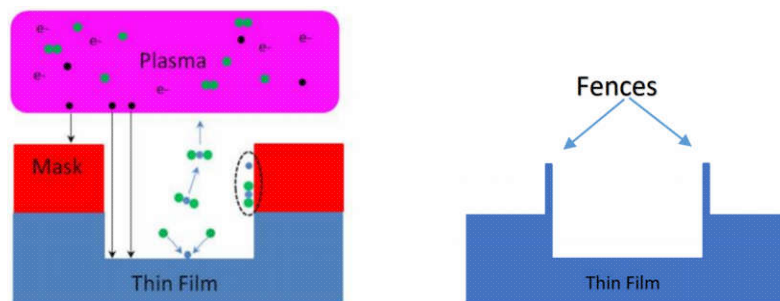
(a) Fence formation
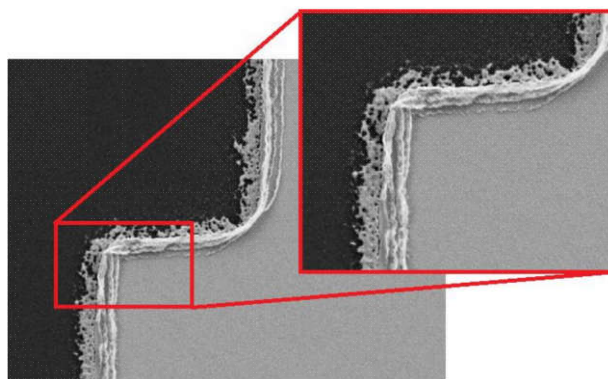
(b) SEM photo of Pt fence.

Figure 4-8: The fence defects in dry etching Pt [136].

4.3.1.3. Liftoff process of Pt film

Liftoff process may be one of the most popular manufacturing approaches for patterning a Pt film of MEMS device [137]. Its process flow is quite simple and short. Generally, it is comprised of three main steps: lithography, film deposition, and PR stripping.
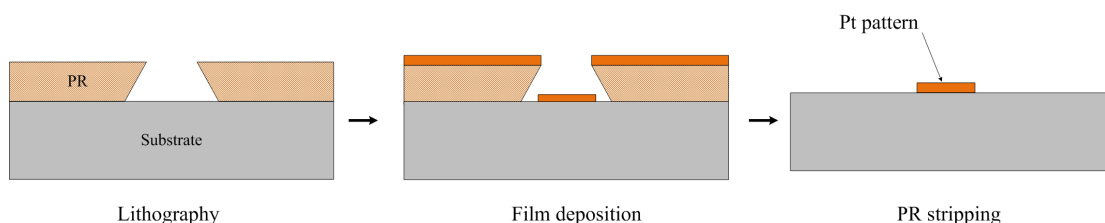

Figure 4-9: A typical liftoff process flow.

(1) **Lithography** The inverse trapezoidal PR patterns form on the substrate through lithography, which is inverse to the desired patterns.

(2) **Film deposition** The target film is deposited on the PR patterned substrate. In the uncovered region, Pt adheres to the substrate or adhesion layer, while, on the other region, Pt and substrate are separated by PR.

(3) **Resist stripping** The PR is immersed in a solvent with ultrasound agitation. PR is dissolved, and Pt attached on PR is stripped away simultaneously. In contrast, the Pt attached to the substrate or adhesion layer remains.

The key to the liftoff process is the proper step coverage of the film deposition. The definition is illustrated in Figure 4-10. High step coverage is usually expected in the film deposition. For example, the via filling process of a CMOS device, high step coverage of

the metal film is essential for the electric connection. However, for a liftoff process, low step coverage is expected. A discontinuity of the deposited film is created at the PR sidewall. Only in this way, the film can be swept away easily during PR stripping.

The film deposition approach and undercutting amount at the bottom of PR are the main factors to determine step coverage. Generally, evaporation deposition has lower step coverage than sputter deposition. Thus it is supposed to be more suitable for the liftoff process. Due to the accessibility of film deposition tools, sputtering deposition is actually employed in the Pt film in our work. Negative PR can usually form an inverse trapezoidal sidewall, which is used to create undercutting to reduce step coverage [138][139].
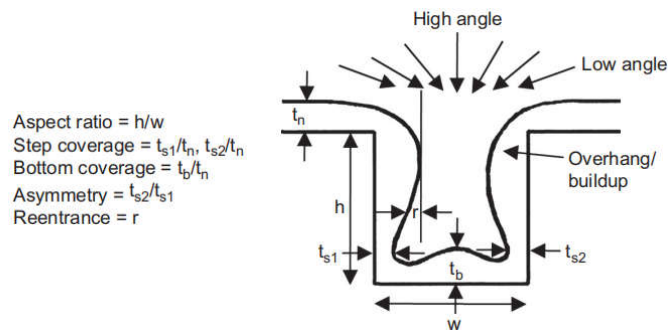

Figure 4-10: Schematic illustration of step coverage [140].

4.3.1.4. Liftoff process with positive PR for Pt wire patterning

Since negative PR can naturally create an inverse inclination sidewall, it is frequently employed in liftoff processes. To obtain a pattern smaller than 5 µm linewidth is not an easy target for regular negative photoresists exposed by a mask aligner with 365 nm wavelength, working in contact mode. On the other hand, it is relatively less complicated when using positive PR. In our work, Pt film is patterned by the lift-off process, and a positive PR is utilized. The inverse trapezoidal sidewalls are achieved by image reversal lithography. The process makes use of AZ5214E that is a positive tone photoresist for image reversal purpose with a very good resolution and high glass point (more than 130ºC). Compared with the usual lithography procedure, as mentioned in Figure 4-3, the image reversal procedure has a PR baking step that follows the first exposure and a flood exposure without the mask. The procedure is illustrated in Figure 4-11. During the reversal baking, the substrate is heated

after the first exposure. Thus the exposed area is cross-linked and becomes inert to the developer, while the unexposed area remains photoactive. The flood exposure can expose the whole wafer. Indeed, the area that has not been exposed in the first exposure is exposed and becomes soluble in the developer. The flood exposure does not change the solubility of the PR that has already been exposed in the first exposure since the already exposed area is no longer photoactive due to reversal baking. By this method, PR patterns obtained in the first exposure remain on the substrate, which has the inverse trapezoidal profile just like negative resist but also keeps proper resolution almost as good as a positive resist. Figure 4-12 presents some results that were obtained after liftoff. It shows that the positive PR liftoff process can achieve Pt wires with dimensions as small as 2 μm line width.
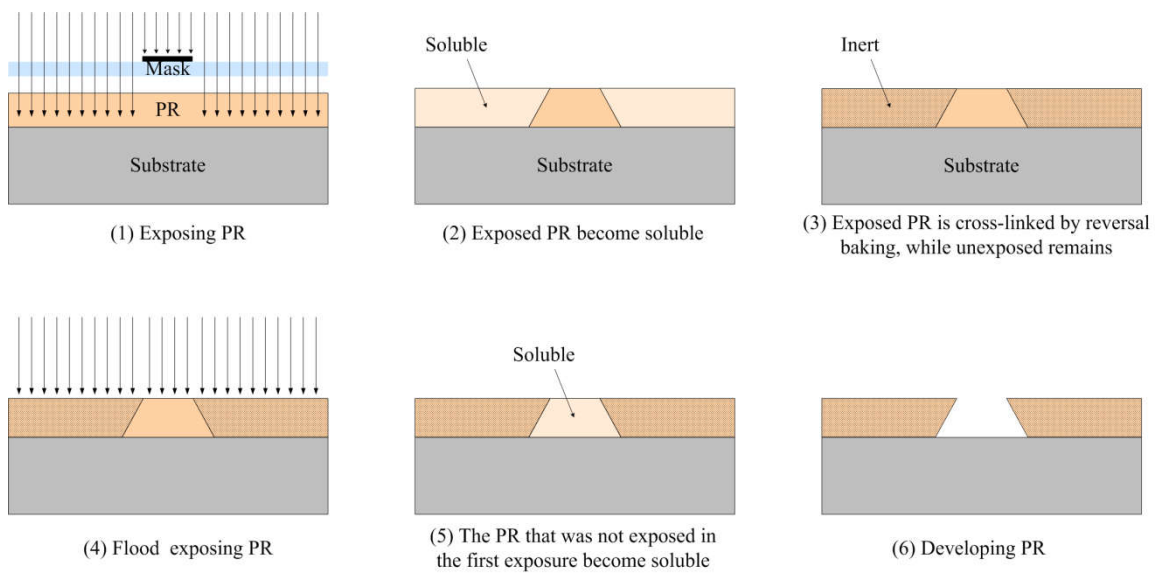

(1) Exposing PR

(2) Exposed PR become soluble

(3) Exposed PR is cross-linked by reversal baking, while unexposed remains

(4) Flood exposing PR

(5) The PR that was not exposed in the first exposure become soluble
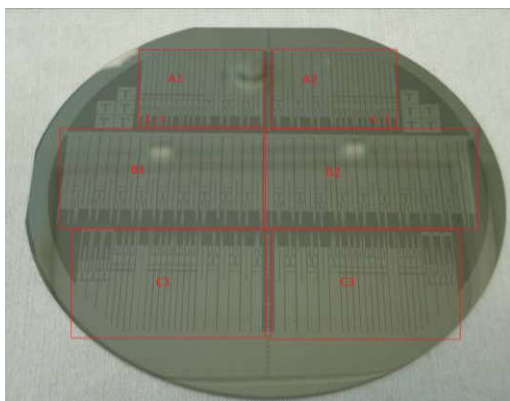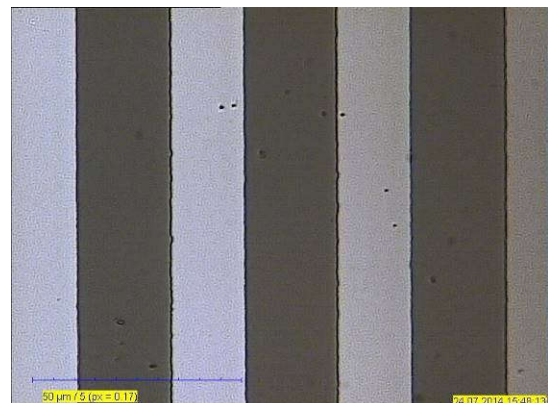
(6) Developing PR

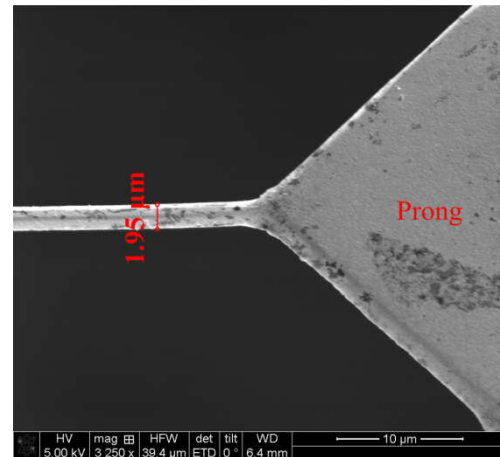Figure 4-11: The inverse trapezoidal profile fabricated by positive PR.

(a) The hot wire sensor wafer after Pt liftoff.

(b) Test patterns for Pt liftoff.

| (c) Smallest test patterns obtained after Pt liftoff. | (d) Smallest resultant Pt wire in a resultant hot wire sensor. |

Figure 4-12: The results of Pt liftoff process with positive PR.

In addition to step coverage issues, another consideration in the liftoff process with positive PR is substrate temperature control in the Pt deposition. The sputtering process is always accompanied by heat generation, the flux of which mainly depends on the sputtering power [141]. Most of the sputtering heat is dissipated to the sputtering chamber and substrate susceptor by thermal conduction and radiation. Besides, a part of the heat is stored in the substrate, which may induce temperature rising of the substrate. In the whole deposition process, the maximum temperature of the substrate should always be lower than the glass transition temperature of PR, above which the physical property of PR changes from a hard and glassy state to a viscous and soft one. Otherwise, PR reflow may take place, by which the inverse trapezoidal sidewall of the already obtained PR patterns becomes rounded under the effect of PR surface tension. At a higher temperature, PR may be highly cross-linked and carbonized. All of these effects will give rise to liftoff failure. Figure 4-13 illustrates some results that inappropriate substrate temperature may give rise to. In Figure 4-13a, test patterns of the liftoff process cannot be stripped even though it has been immersed for a long time. The pattern has swelled up, and PR under Pt becomes partially carbonized. The Pt film at the rounded PR sidewall exhibits good step coverage. In Figure 4-13b, the liftoff residues of Pt remain on the edge of the intended Pt patterns. It implies that improper step coverage occurs in Pt film sputtering.
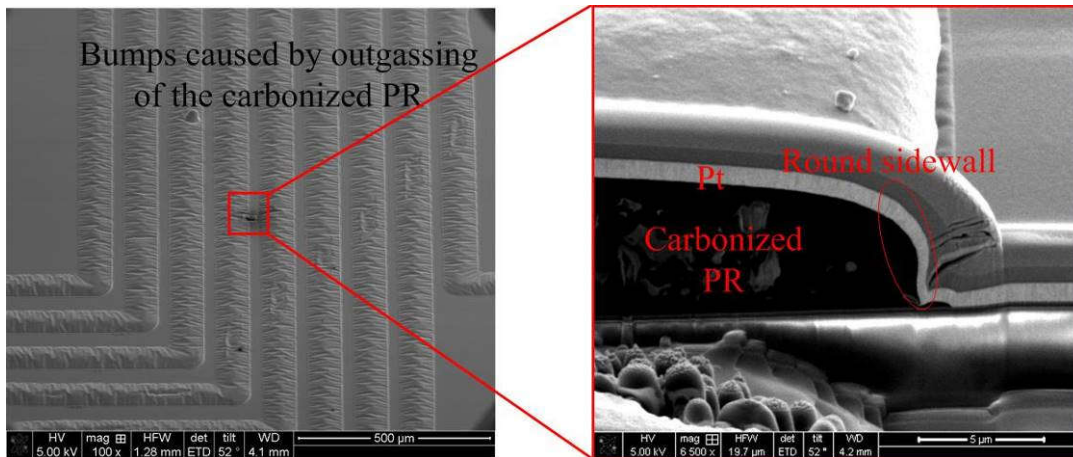
(a) PR carbonization during Pt sputtering.
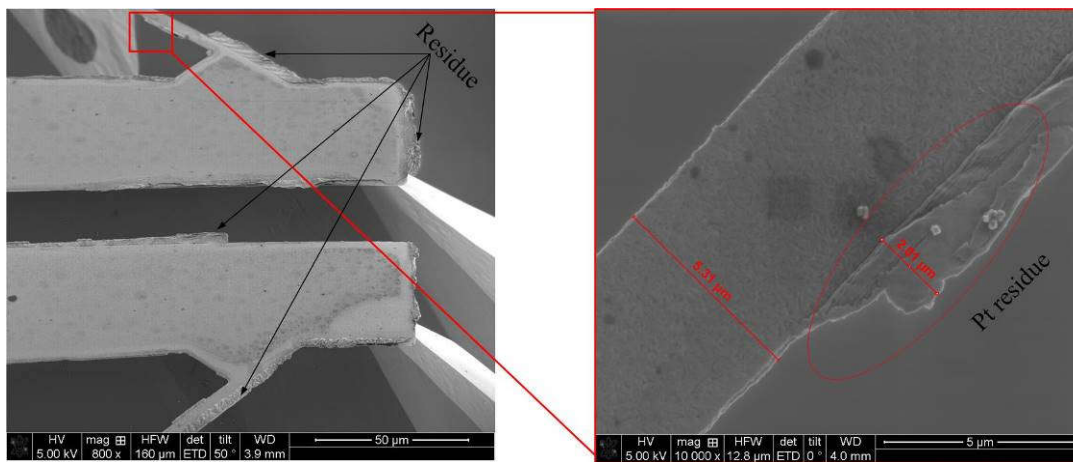
(b) Residue on the edge of Pt pattern after liftoff.

Figure 4-13: Liftoff defects caused by high substrate temperature.

Since the accumulated heat is approximately proportional to the sputtering duration, a non-stop sputtering may cause the substrate temperature to rise continuously. To avoid this, a complete deposition process is separated by several cooling steps. During the deposition pausing, the substrate is cooled by thermal conduction and radiation. To adjust the sputtering duration and the ratio of sputtering duration to cooling time or called the duty cycle, the temperature peak may be reduced to a lower value than the glass transition temperature.

AZ5214E has a 130ºC reflow temperature. The longest duration of a single sputtering cycle to ensure that PR reflow does not take place was investigated. At a constant sputtering power of 100 W, the maximum temperatures that have already reached under a set of the

different sputtering time were recorded by a temperature indicator. In our process, a reasonable choice of duty cycle was found to be every 30 seconds sputtering followed by 5 minutes cooling.

4.3.2. Fabrication of a suspended Pt wire

4.3.2.1. Surface micromachining technology of a suspended film beam

Suspended thin film beams are the basic structures applied in MEMS devices, serving as mechanical resonators, RF switches, thermal actuators, cantilever sensors, etc. Such structures are usually achieved by surface micromachining technology, which makes it possible to build freestanding thin film structures over a rigid substrate [142][143]. Two types of materials are utilized: structural material and sacrificial material. The former is the material needed for the component being constructed, such as doped polysilicon, nitride, or metals. The latter is to provide the desired gap between two structural layers, such as silicon oxides, photoresist, some metals. The sacrificial layer is etched isotropically to enable the lateral undercutting and the final release of the structural layers. Taking a free-standing polysilicon cantilever as an example, the typical fabrication process consists of several main steps: 1) depositing the sacrificial and structural layers in turn on the substrate; 2) pattern transfer by lithography and etching of the structural material; 3) etching the sacrificial layer to release structural patterns. By this method, a suspended film beam can be created over the substrate.
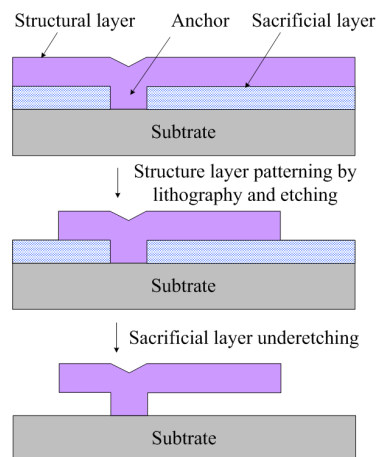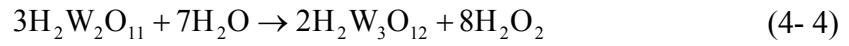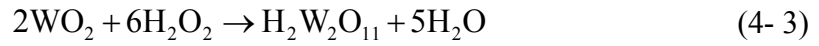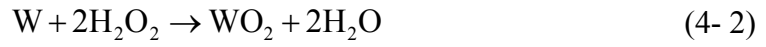
Figure 4-14: Outline of a typical surface micromachining process.

4.3.2.2. Surface micromachining process for freestanding Pt wire

As illustrated in Figure 3-1, the Pt wire is mostly freestanding over its substrate. This structure is achieved by a surface micromachining process, where Pt is the structural material, and WTi is selected as the sacrificial layer. Initially, the Pt film is patterned by a liftoff process. Subsequently, the WTi film underneath the Pt wire pattern is undercut by isotropic etching. The main procedure is illustrated in Figure 4-15a.

Hydrogen peroxide (H_2O_2) is utilized to etch WTi, which is an eco-friendly oxidant. It is known that it can readily dissolve WTi [144][145], while the etching mechanism of WTi alloy is not clear. W can react with H_2O_2 through a redox reaction; a proposed dissolution mechanism is of the form [146]:

$$W + 2H_2O_2 \rightarrow WO_2 + 2H_2O \qquad (4\text{-}2)$$

$$2WO_2 + 6H_2O_2 \rightarrow H_2W_2O_{11} + 5H_2O \qquad (4\text{-}3)$$

$$3H_2W_2O_{11} + 7H_2O \rightarrow 2H_2W_3O_{12} + 8H_2O_2 \qquad (4\text{-}4)$$

Ti can be etched by ammonia-added or HF-added H_2O_2, and the oxide of Ti can react with H_2O_2 to form soluble complexes [147][148].

Since the deposited Pt film is opaque, it is hard to decide the etching endpoint of WTi by real-time observation. In practice, etching time is used to predict the etching endpoint in the absence of a dedicated endpoint detection tool. The resultant undercutting of WTi, U_{WTi}, is estimated by the following expression:

$$U_{\text{WTi}} = r_{\text{WTi}} \cdot t_{\text{WTi}}, \qquad (4\text{-}5)$$

where r_{WTi} is the average etching rate of WTi in H_2O_2 and t_{WTi} is the actual etching time. By precise control of the etching rate of WTi and etching time, a specified amount of WTi is removed while other parts remain. As illustrated in Figure 4-15b, the desired undercutting amount of WTi requires

$$U_{\text{WTi}} \approx \frac{l_1}{2}, \qquad (4\text{-}6)$$

where l_1 is the width of the Pt wire.

(a) The main steps of surface micromachining of Pt wire

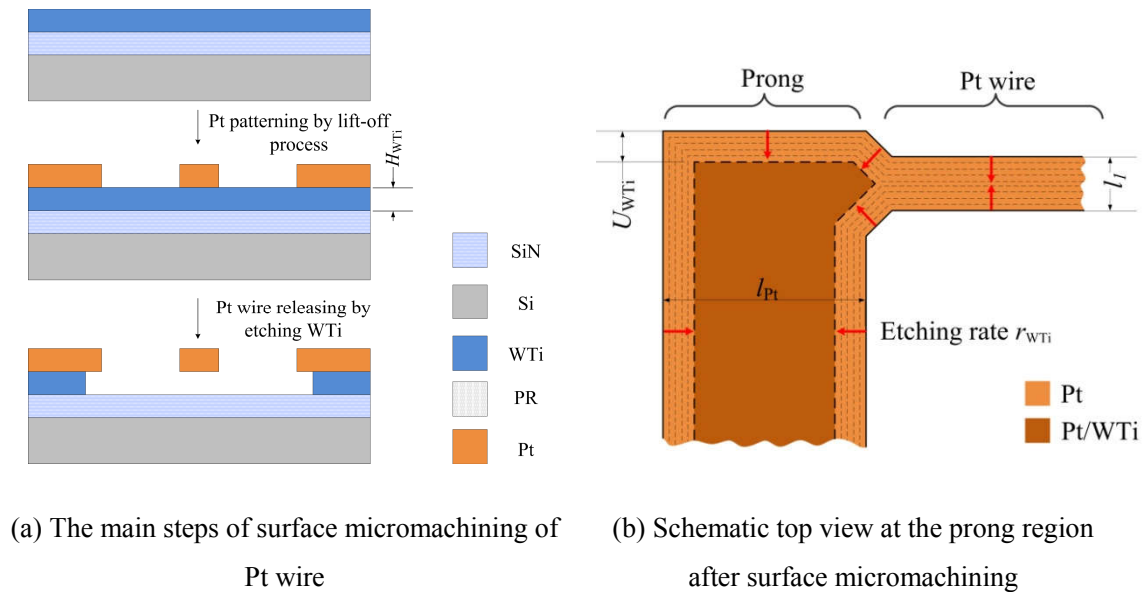(b) Schematic top view at the prong region after surface micromachining

Figure 4-15: The surface micromachining process of a suspended Pt wire.

4.4. Fabrication of the prongs

The manufacturing of a suspended Pt wire has been introduced in the previous section; the following refers to the fabrication process of Si prongs.
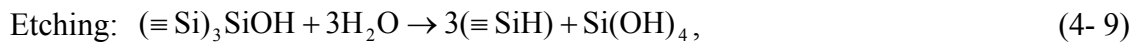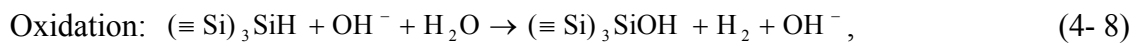
4.4.1. Bulk Si micromachining

Bulk Si structures, such as Si beams and Si membranes, which take advantage of the excellent mechanical properties of Si crystal, are widely applied to various MEMS devices, such as inertial devices, pressure sensors, AFM probes, micro grippers, etc. They are usually realized by bulk Si micromachining, which is an alternative concept to surface micromachining. Unlike surface micromachining, where the materials to be etched are thin films on the Si substrate, the target material of bulk Si micromachining is the Si substrate itself, where a significant amount of Si, ranging from a few microns to hundreds of microns, is selectively removed so as to create three-dimensional structures. Besides Si etching, the selective removal of Si also necessarily contains other basic MEMS processes, such as the deposition of Si etching mask and patterning.

Anisotropic wet etching of Si is the priority option in bulk silicon micromachining due to its low fabrication cost, despite the widespread application of dry etching in bulk Si micromachining. KOH and TMAH are the most used etchants for anisotropic wet etching of

Si. KOH solutions can achieve a very high etching selectivity of 600:400:1 for <110>, <100>, and {111} Si planes, and provide etching rates of up to 2 μm/min with excellent selectivity for oxide, nitride, and highly boron-doped Si. TMAH is a quaternary ammonium compound. It does not contain mobile alkali ions that are serious contaminants for CMOS devices. Si atoms can react with water and OH^- ions of the above solutions and become water-soluble. The overall reaction is expressed as

$$Si + 2H_2O + 2OH^- \rightarrow Si(OH)_2 O_2^{2-} + 2H_2. \tag{4-7}$$
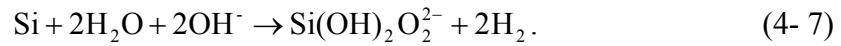
The etching can be further divided into two steps: oxidation and etching. Making an example of the etching at {111} planes, the sequential reactions take place:

Oxidation: $(\equiv Si)_3 SiH + OH^- + H_2O \rightarrow (\equiv Si)_3 SiOH + H_2 + OH^-,$ \hfill (4-8)

Etching: $(\equiv Si)_3 SiOH + 3H_2O \rightarrow 3(\equiv SiH) + Si(OH)_4,$ \hfill (4-9)

where the symbol "$\equiv$" represents three back bonds of Si. Similar equations can be applied to the etching at the {110} planes and {100} planes. The Si crystal has a diamond lattice structure. When the outermost Si atoms on the crystal surface are exposed to the solution, due to the presence of active dangling bonds on the outermost atoms, the atoms are quickly terminated with H in the solution. In the oxidation step, OH^- ions are attached to H-terminated Si atoms by replacing of H. O has a larger electronegativity than Si; Si-Si bonds are weakened and become vulnerable. Therefore, as long as the attachment of Si and OH^- take place, it will trigger the subsequent process that the residue back bonds of the outermost Si atoms are further attacked by OH^- ions. Consequently, Si atoms are fully terminated with OH^- to form the product Si(OH)$_4$. The product is dissolved in the solution to achieve the removal of Si. The complete process is illustrated in Figure 4-16.
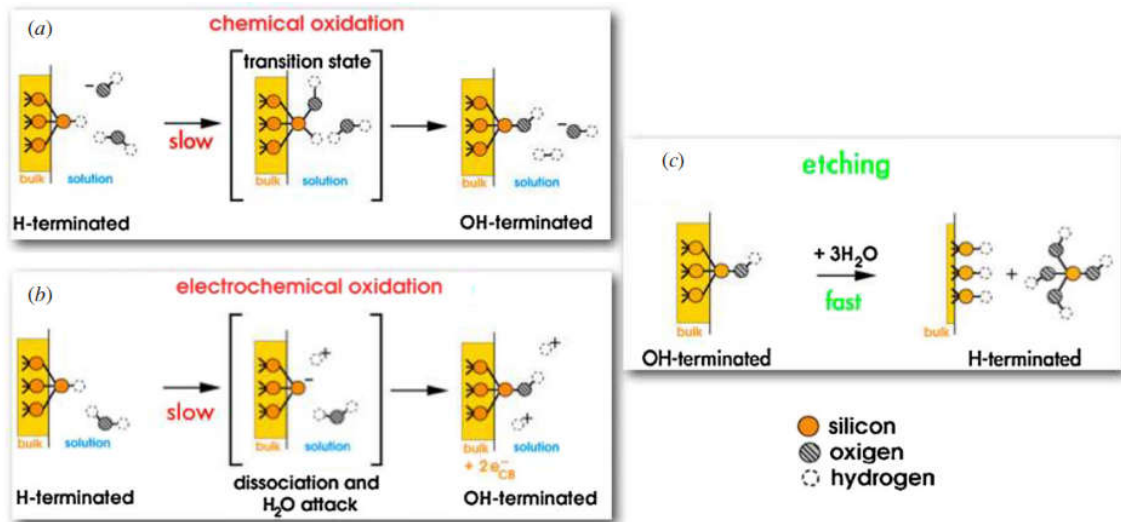
Figure 4-16: Schematic representation of the sequential Si oxidation and etching reactions taking place in alkaline solution [149].

In the above two steps, the oxidation is rate-limiting. The oxidation process plays a critical role in determining Si etching rate. It implies that the surface density of H-termination or dangling bonds on the Si crystal surface may affect the Si etching rate. Figure 4-17 illustrates an actual etching rate for different crystallographic planes and concentrations, resulting in anisotropic etching.
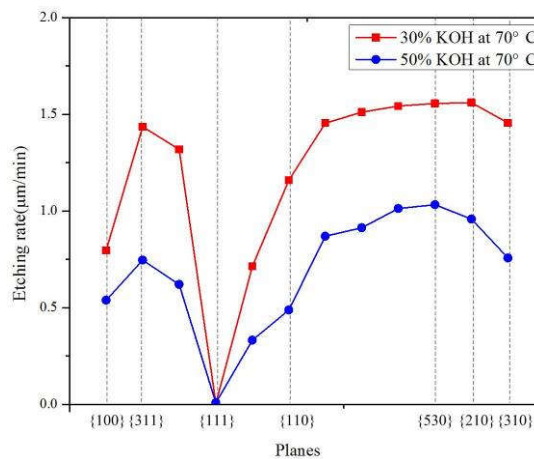

Figure 4-17: The etching rate for different crystal planes (The data is from [150]).

Anisotropic Si wet etching is able to form various regular geometries, such as V-grooves, pyramids, cavities, as illustrated in Figure 4-18. The profiles are created in a {100} Si substrate, and their mask edges are aligned to the <110> directions. {100} and {110} planes have much higher rate than {111} planes. After the initial {100} facets at the mask edge are dissolved, the slow etching {111} facets are thus revealed, which will hinder subsequent fast

etching facets. Therefore, specific etching profiles occur at the mask edges. For any two crystallographic planes, (x_1, y_1, z_1) and (x_2, y_2, z_2), their intersection angle θ_{Si} is calculated by the following mathematical operation:

$$\arccos\theta_{Si} = \frac{x_1x_2 + y_1y_2 + z_1z_2}{\sqrt{x_1^2 + y_1^2 + z_1^2} \cdot \sqrt{x_2^2 + y_2^2 + z_2^2}} \qquad (4\text{-}10)$$

Note that the intersection angle of {100} and {111} planes, as illustrated in Figure 4-18, is 54.7º. More angles and complex structures can be created by employing various orientations of etching mask edges and crystalline orientations of Si wafers.
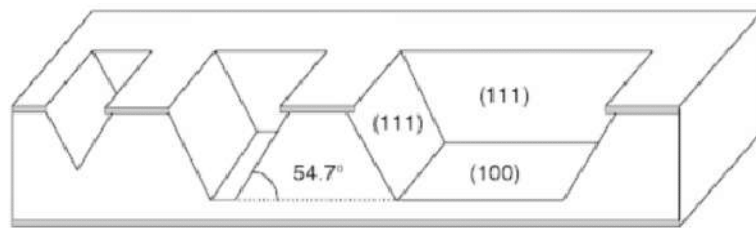

Figure 4-18: Example profiles of anisotropic wet etching on {100} Si.
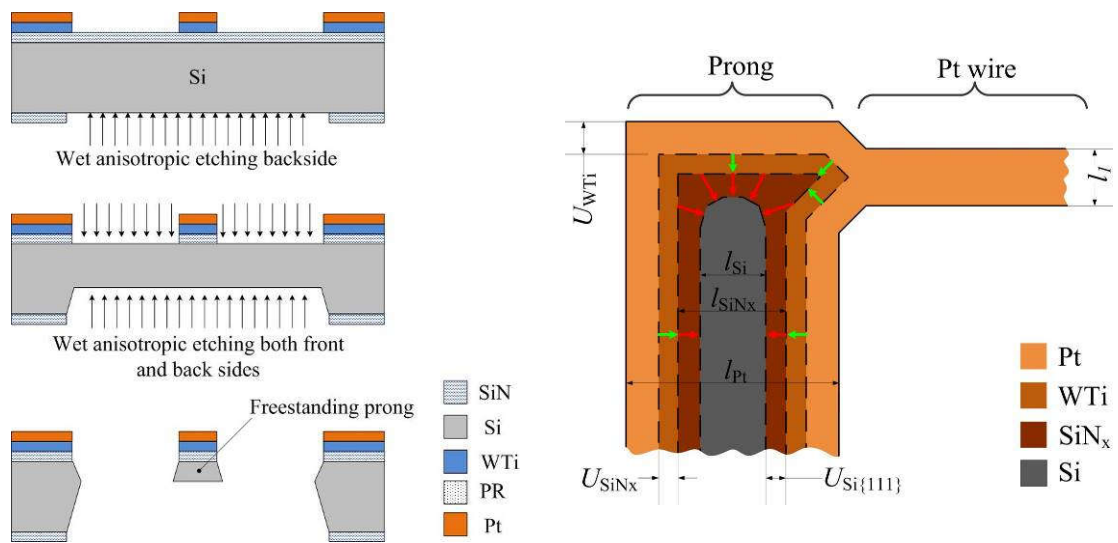
4. 4. 2. The micromachining process of prongs

As illustrated in Figure 3-1, the intended hot wire sensor consists of two freestanding Si prongs to support the Pt wire, with the thickness on the order of a hundred microns. The prongs were achieved by bulk Si micromachining. Two anisotropic wet etching steps on a {100} Si wafer were involved. The primary processes are presented in Figure 4-19a. Nitride acting as the mask layer is firstly deposited on both sides of the wafer by PECVD and patterned on the backside. The edges of the mask patterns are aligned to the <110> directions. Then the wafer is immersed in a KOH solution. The Si on the opening area of the wafer backside is etched away in order to create a cavity. The residue Si on the bottom of the cavity forms a thick Si membrane, the thickness of which is equal to the required thickness of the prongs. After nitride on the front side is patterned, the wafer is immersed in a TMAH solution. The etching starts from the top and bottom surfaces of the membrane simultaneously. This process is stopped manually when the two etching facets of the membrane encounter. The residual Si of the membrane forms the wires' prongs. The topside width of the resultant Si prong, l_{Si}, is calculated by the expression:

$$l_{Si} = l_{Pt} - 2U_{WTi} - 2U_{SiNx} - 2U_{Si\{111\}}, \qquad (4\text{-}11)$$

where l_{Pt} is the Pt width after the liftoff process; U_{SiNx} is the undercutting of nitride under the WTi layer; $U_{\mathrm{Si\{111\}}}$ is the etching rate of {111} Si planes. Note that, in order to avoid undercutting of the Si prong, residue nitride on the prong region, l_{SiNx}, should essentially meet the condition:

$$l_{\mathrm{SiNx}} = l_{\mathrm{Pt}} - 2U_{\mathrm{WTi}} - 2U_{\mathrm{SiNx}} > \frac{2r_{\{111\}}t}{\sin 54.7^\circ} , \qquad (4\text{-}12)$$

where $r_{\mathrm{Si\{111\}}}$ is the etching rate of {111} Si planes in TMAH, and t is the etching time.


(a) The main steps of bulk micromachining of the Si prong.

(b) Schematic top view at the prong region after bulk micromachining.

Figure 4-19: The bulk Si micromachining process of the prong.

It should be mentioned that if the second anisotropic etching is not terminated immediately when the expected etch stop is reached, then new etching front planes appear, as explained in Figure 4-20. The new planes are supposed to be mainly (311) [151].
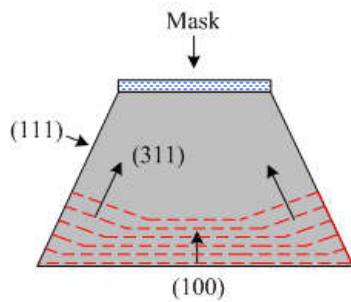
(a) Schematic cross-section of a prong
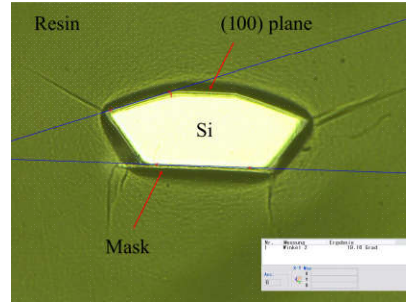
(b) The polished cross-section of a resultant prong encapsulated by resin

Figure 4-20: Crystal profile of an overetched prong.

4. 5. The overall fabrication process flow

The individual processes of Pt wire and prongs have been introduced above. The integrated process flow to fabricate the hot wire sensor is presented in Figure 4-21. Its distinguishing features are that only two photomasks are used, thus reducing the process complexity and cost considerably. The details of the process flow are:

(a) 0.5 μm thick nitride is deposited by PECVD on both sides of a double- side-polished {100} Si wafer with 500 μm thickness.

(b) 1 μm WTi is deposited on the front side of the substrate by DC magnetron sputtering. It is the adhesion layer of nitride and Pt, as well as the conduction layer.

(c) 1.3 μm thick positive PR, AZ5214E is spin-coated onto the substrate.

(d) Through reversal image lithography, PR patterns with inclined sidewalls form on the wafer.

(e) 300 nm Pt is deposited on the surface of WTi by DC magnetron sputtering.

(f) The wafer is immersed in acetone and stirred by ultrasonic. Pt film on the PR is lifted off, and the others remain on the substrate.

(g) 1.3 μm thick AZ5214E is spin-coated on the backside of the wafer.

(h) PR is patterned by conventional positive lithography. The residue PR patterns are the etching mask of nitride.

(i) The nitride without a PR mask on the backside of the wafer is etched by a diluted HF solution.

(j) The residue PR is stripped.

(k) The wafer is immersed in a KOH solution. 300 μm Si is etched on the backside. During this step, the front side is protected by the WTi layer.

(l) The wafer is immersed in H2O2 solution. WTi on the area that is not protected by Pt patterns is etched. By accurately controlling the etching time, the undercutting of WTi only appears in the Pt wire region. The Pt wire is thereby released.

(m) Nitride in the opening area of the front side is etched by a diluted HF solution. The front side Si is exposed.

(n) The wafer is immersed in the diluted TMAH solution. The Si etching starts from both sides. When the wafer is etched through, the etching is terminated.
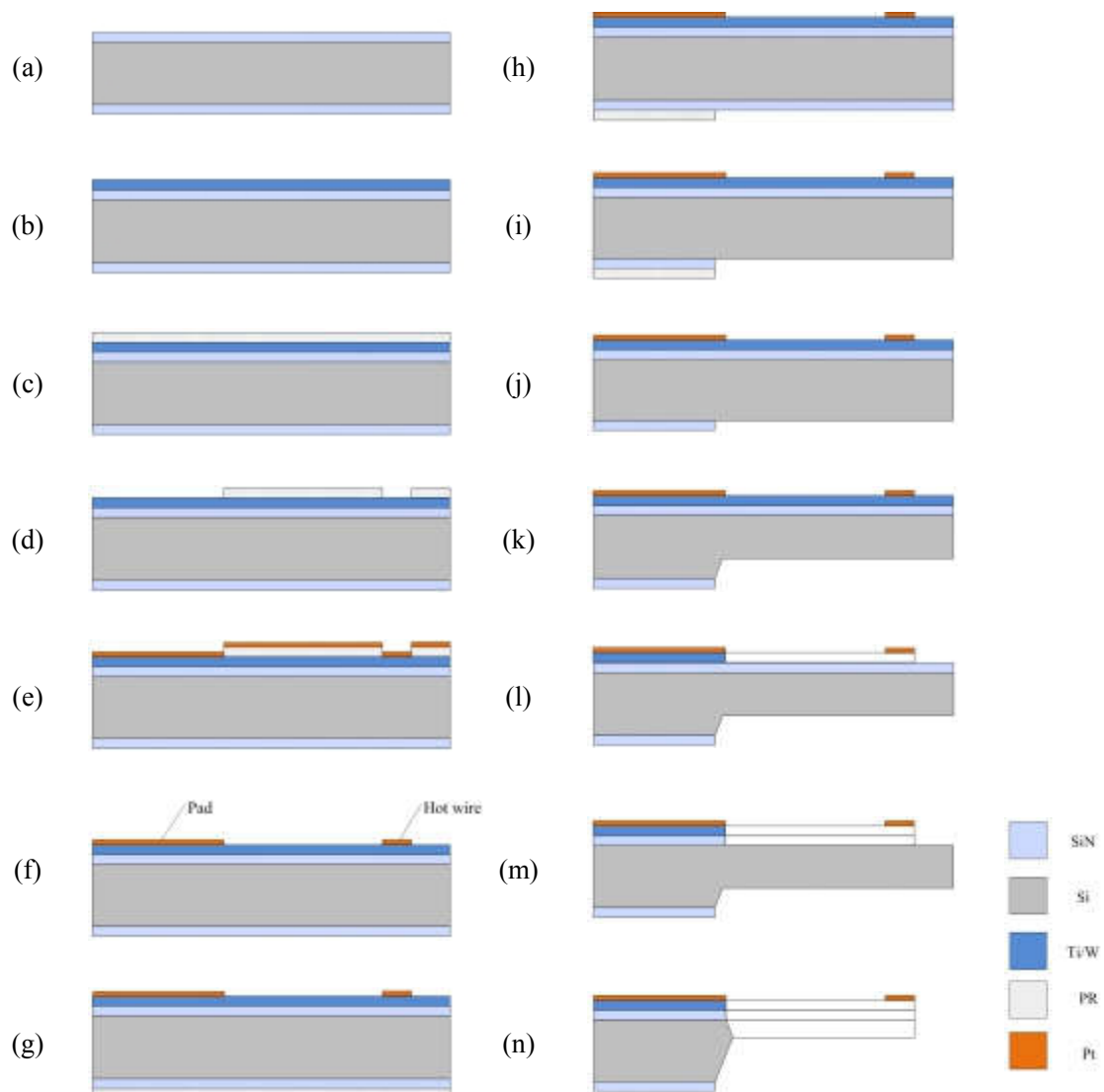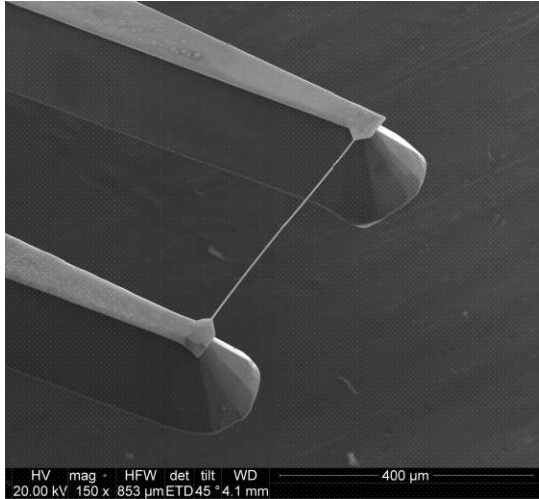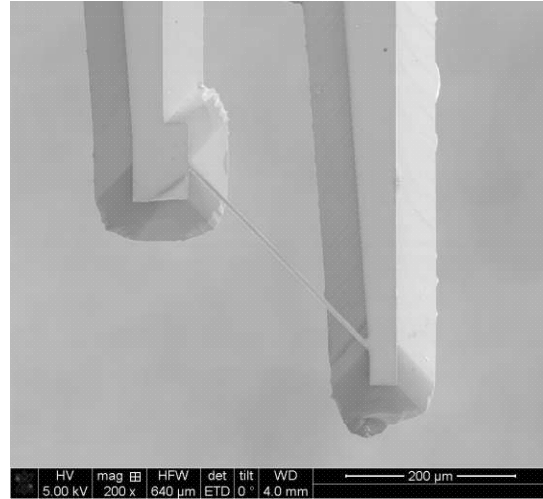

Figure 4-21: The main process flow of hot wire sensors.

Making use of the MEMS processes mentioned above, various hot wires sensor with different shapes and dimensions were fabricated, as illustrated in Figure 4-22. The thinnest Pt wire reached around 3 μm in width and 300 nm in thickness (in Figure 4-12d).
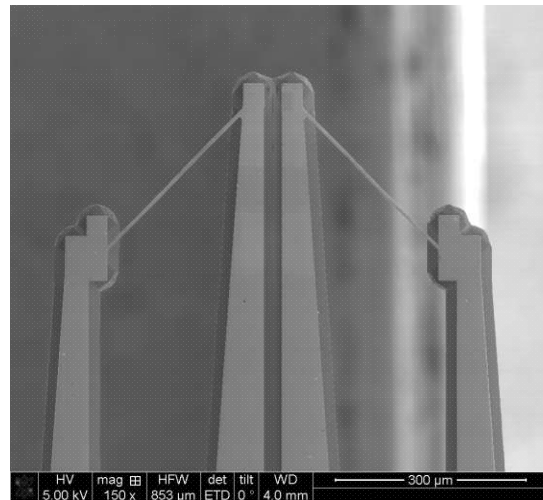

(a) Single hot wire for flow velocity measurement.

(b) 45º single hot wire for flow velocity measurement.
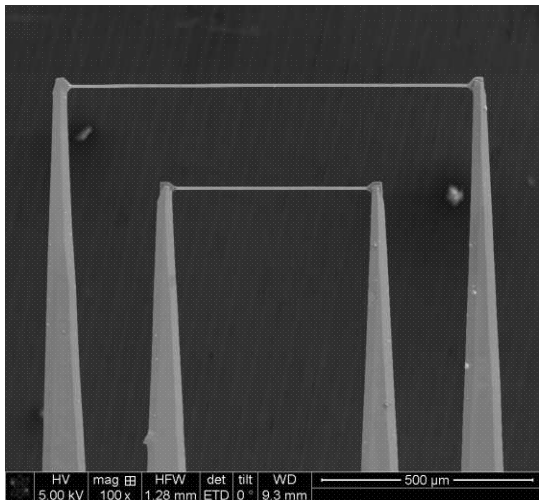
(c) Two parallel hot wires for shear stress measurements.

(d) Two hot wires for 2D velocity measurement.

Figure 4-22: Examples of fabricated hot wire sensors.

4.6. Process issues of hot wire sensor fabrication

During the fabrication of hot wire sensors, there are some issues that need to be taken into

consideration.

4.6.1. WTi film stress

Film stress is an important variable that needs to be considered in the film deposition process. Inappropriate film stress can result in adhesion problems or in significant deformation of the final structure. The frequently encountered problem during film deposition is the presence of too high compressive stress in WTi films. It may cause film delamination of WTi, as shown in Figure 4-23.
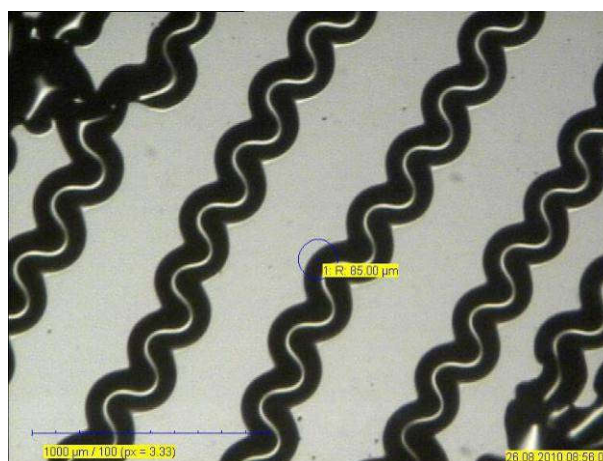

Figure 4-23: Film delamination patterns caused by compressive stress in the sputtered WTi film.

Thermal stress and intrinsic stress are two contributions to film stress. Thermal stress is attributed to the difference between the thermal expansion coefficients of the substrate and the sputtered film. Intrinsic stress is defined to be the stress that arises during the deposition but does not belong to thermal stress. It has strong relevance to the film microstructure. Thornton proposed a structure zone diagram to estimate the film microstructure, which mainly considers the effect of atoms' mobility on the film microstructure during film growth. This model selects the working gas pressure and the substrate temperature as the most crucial deposition parameters [152]. A typical Thornton diagram of sputtering deposition is illustrated in Figure 4-24. It consists of four regions:

Zone I: Porous and columnar structure due to lacking atom mobility.

Zone T: Dense and fibrous grain. Atoms' mobility is high enough to develop grain, but not enough to move grain boundaries further.

Zone II: Columnar grain. The grains grow throughout the whole film thickness.
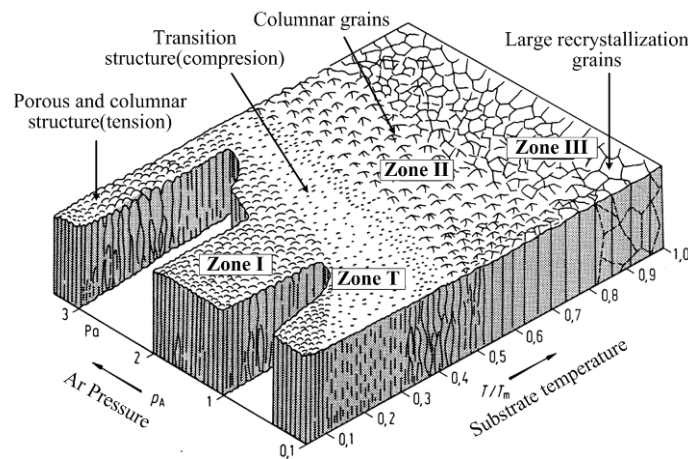
Zone III: Large grains due to recrystallization.

Figure 4-24: Schematic representation of Thornton zone diagram for sputter deposition[152].

The porous structure tends to shrink, which gives rise to tensile stress. Hence, zone I usually exhibits tensile stress. In contrast, zone T often exhibits compressive stress, which implies the structure is compressed by a striking effect of highly energetic atoms. From zone I to zone T, the film stress undergoes the transition from tensile state to compressive state, which corresponds to the transition of the working gas pressure from high values to low ones. Since the collision's probability between working gas molecules and ejected atoms is proportional to the gas pressure, the collisions can reduce the atoms' momentum arriving at a substrate. The stress transition can be explained that the striking effect that the substrate suffers is continuously reduced when pressure increases. It needs to be emphasized that the pressure point that can induce stress transition is not unique. This is because sputtering power can affect ejected atoms momentum and the substrate temperature; both of them will change film stress as well.

WTi films are deposited on bare Si wafers by a magnetron sputtering tool. In order to reduce the stress of the WTi film, the Ar pressure of the sputtering recipe was tuned to search the transition point of film stress at low sputtering power. The increment of wafer bow before and after deposition was measured by a dedicated tool. The induced stress can be calculated by Stoney's equation [153]. Figure 4-25 shows the relation of Ar pressure and the stress of 1 μm WTi at 250 W. It shows when Ar pressure is reduced from 0.03 mbar to 0.001 mbar. The stress of the WTi film is changed from a compressive state to a tensile state. The stress of WTi film deposited at the pressure of 0.03 mbar almost reaches the minimum, 10 MPa. It was selected as the working pressure for sputtering WTi.
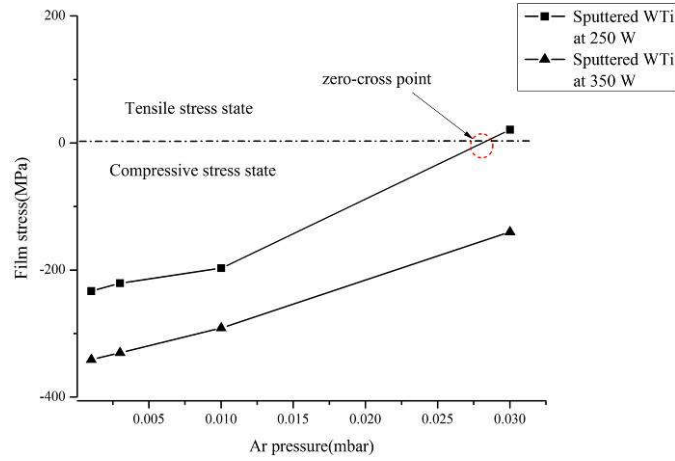
Figure 4-25: The relation of WTi film stress and Ar pressure for the sputter deposition.

4. 6. 2. Resistivity and TCR

Resistivity and its temperature coefficient are the critical material properties that affect sensor performance. As discussed in the previous chapter, a high TCR of Pt film is advantageous for high sensitivity measurements of hot wire sensors. In contrast, a low TCR is desired for the WTi film, thus reducing the variation of the prongs' resistance.

The classic explanation of resistivity is based on the carrier scattering that reduces carrier mobility. For metals, the carriers are free electrons. When a voltage is applied to a metal conductor, the free electrons are driven by the voltage, but decelerated by collisions with obstacles, like the lattice vibrations (phonons) of the metal. The Drude model gives an expression of electrical conductivity, which is the reciprocal of resistivity:

$$\sigma_e = \frac{ne^2}{m}\tau_e, \tag{4-13}$$

where n, e, m are the density of free electrons, the electron's charge, and electron's mass; Analogous to the definition of mean free path, τ_e refers to the statistical mean free time of the carrier between two scattering events. Obviously, the collisions will shorten the free time so as to increase resistance. The contributions of different types of collisions to overall average scattering time τ can be expressed as follows

$$\frac{1}{\tau_e} = \frac{1}{\tau_{phonon}} + \frac{1}{\tau_{defect}}, \tag{4-14}$$

where τ_{phonon} represents average scattering time of phonons, which is positively related to

the temperature; τ_{defect} represents the contribution of defects that exist inside grains and between grain boundaries. Combining Eq. (4-13) and Eq. (4-14), the resistivity is of the form:

$$\rho = \frac{m}{ne^2} \cdot \left(\frac{1}{\tau_{phonon}} + \frac{1}{\tau_{defect}} \right) . \qquad (4\text{-}15)$$

The defect of the metal film is further subdivided into different sources: impurities, inner grain, the grain boundaries surface [154][155][156], thus the expression of resistivity can be written in another form,

$$\rho = \rho_P + \rho_I + \rho_D + \rho_G + \rho_S , \qquad (4\text{-}16)$$

where $\rho_P, \rho_I, \rho_D, \rho_G, \rho_S$ represent the individual contributions of phonons and different sources of defects to the total resistivity. It is also called Matthiessen's rule [157]. Only ρ_P contributes to the temperature coefficient of resistance, while the others are almost irrelevant to the temperature. Thus ρ_p / ρ can represent TCR to some extent. It implies that in the presence of defects, the resistivity will be higher, and the TCR will be lower than the values of its single-crystal bulk material.

Thin films usually exhibit much higher defect concentrations than the bulk material, hence the film has higher resistivity and lower TCR than bulk Pt [158]. Figure 4-26 illustrates the surface morphology of Pt wire in a finished hot wire sensor. The wire is filled with crystalline grains with an average size of 300 nm－500 nm, and there are massive defects in Pt crystalline grains. These defects are closely related to the deposition process. The film has a TCR of 2482 ppm/K, smaller than the TCR of pure bulk Pt, 3920 ppm/K.
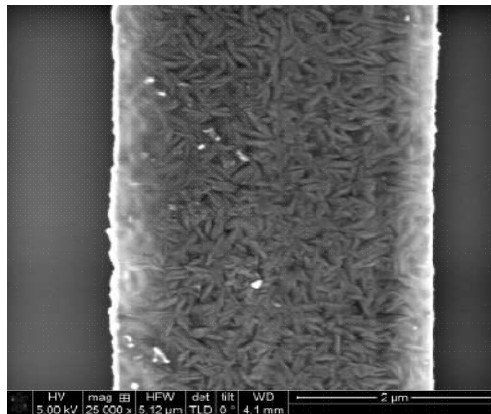

Figure 4-26: Surface morphology of a Pt wire.

Many methods have been used to reduce the defect density in order to improve the TCR. Increasing film growth temperature, increasing film thickness, and annealing above the metal recrystallization temperature are widely accepted methods [159] [160][161][162]. In order to improve Pt TCR, the thickness effect of Pt film on TCR has been verified. Different thicknesses of Pt were deposited by DC magnetron sputtering on Si substrates, with a 30 nm WTi adhesion layer and a SiN_x passivation layer underneath the Pt. The sheet resistance of Pt film at a series of temperature set points was measured by the four-probe method [163][164][165]. The results of the TCR are shown in Figure 4-27. When the thickness exceeds 600 nm, the TCR of as-deposited Pt film can reach 74% of pure bulk Pt.
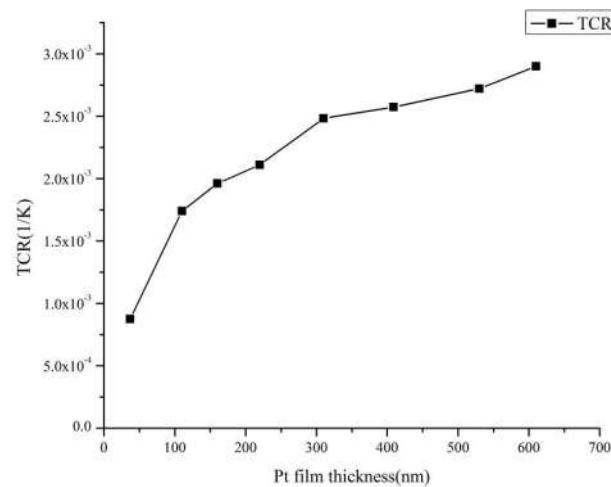

Figure 4-27: The relation of TCR and thickness of an as-deposited Pt film.

Although a thicker Pt film can improve the TCR, it may give rise to a difficulty in Pt film stripping in the liftoff process. In addition, a thicker film will reduce the time constant of the sensor. In practice, we adopted 300 nm thickness of Pt film as a good compromise for fabrication. Its sheet resistance at different temperatures is measured by the four-probe method, and the resistivity is derived by the product of the sheet resistance and film thickness. The result shows it has 2482 ppm/K TCR.

For WTi film, Ti atoms can be regarded as the impurities of W, so, the TCR is supposed to be reduced. The TCR of 1 μm WTi film is measured with the same method as Pt film. The result shows it has 495 ppm/K TCR, significantly smaller than both pure W, 4500 ppm/°C and Ti, 4200 ppm/K. The resistivity of both Pt and WTi film at different temperatures are shown in Figure 4-28.
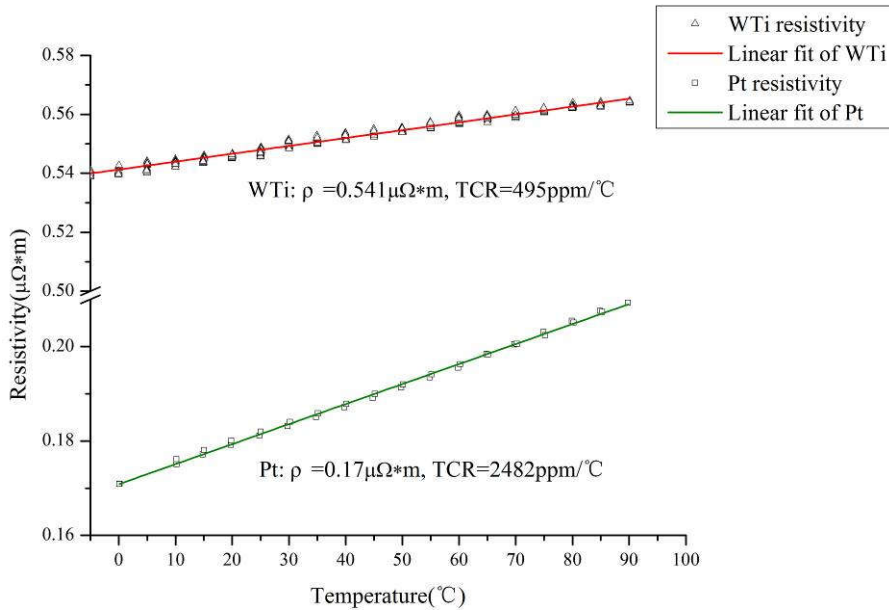
Figure 4-28: The resistivity and TCR of WTi and Pt films.

4.7. Challenge of undercutting in prongs fabrication

4.7.1. The undercutting problem

During etching Si prongs, some lateral undercutting of Si usually occurs at the prongs, as illustrated in Figure 4-29. In consequence, the Pt wires lose mechanical support from the prongs. These problems are mainly related to WTi over-etching and Si undercutting at convex corners.
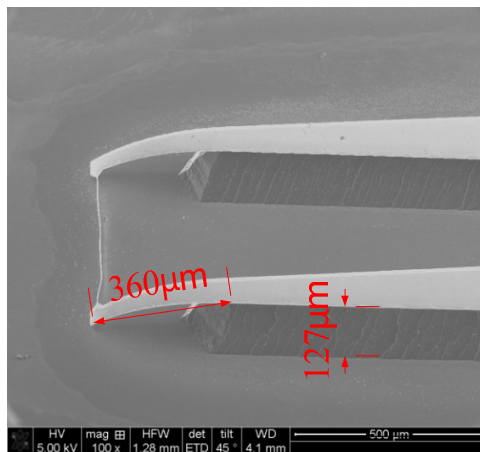

Figure 4-29: Severe undercutting at the Si prongs.

As illustrated in Figure 4-15b, the optimum amount of WTi undercutting is equal to the half-width of Pt wire, $0.5l_1$. However, if the actual undercutting amount exceeds this value

too much, namely, the condition that is specified by the inequality in Eq. (4-12) will not be satisfied anymore. Consequently, the residual nitride mask after HF etching is insufficient to protect the underlying Si from the TMAH attack. Therefore, undercutting at the Si prongs is inevitable.

In fact, inequality (4-12) is essential but not a sufficient condition to avoid undercutting. Figure 4-30 shows an SEM photo of a prong tip that has undergone a complete fabrication flow. It shows that the undercutting of WTi and SiN_x are almost on target. Even so, the undercutting of Si at the prong tip has still occurred under the nitride mask. It is known that undercutting usually takes place at the convex corner of Si structures, while it will rapidly deteriorate in some inappropriate designs. In the following section 4.7.3, we will give a criterion for being free of Si undercutting deterioration and measures.
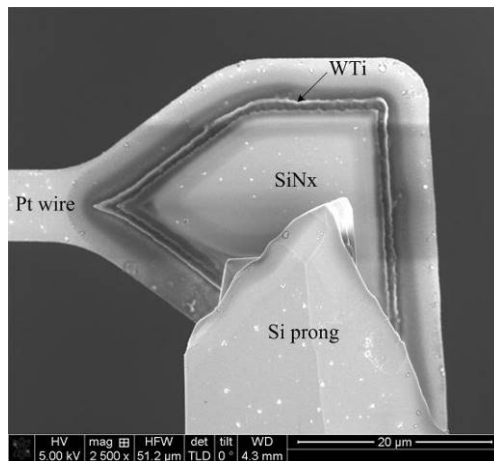

Figure 4-30: Si undercutting at a prong tip without excessive WTi undercutting.

4.7.2. Overetching of WTi

WTi over-etching can be overcome as long as the required etching time is accurately estimated in advance. For this attempt, test structures comprising of WTi and Pt patterns are fabricated on a glass substrate so that the undercutting amount of WTi under Pt prong is conveniently observed. However, this method does not always work well in practice. The undercutting amounts obtained on the glass substrates with the same etching time are not reproducible. A dramatic fluctuation of the WTi etching rate during the process is responsible for this.
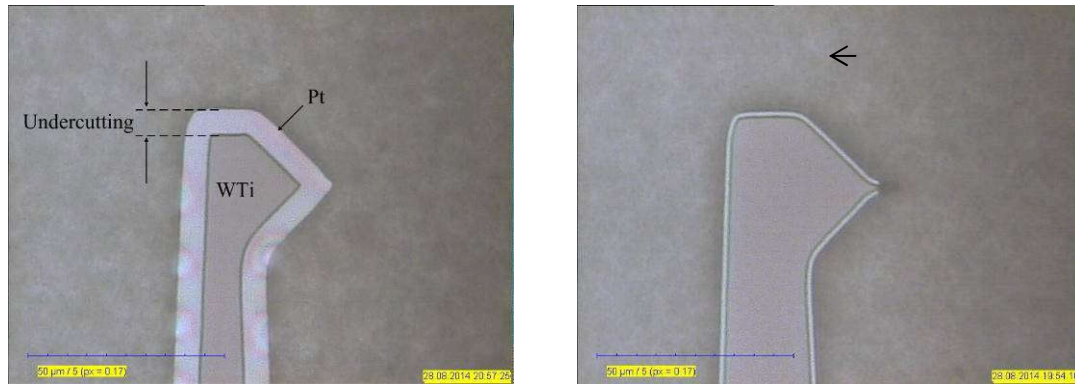
(a) Severe over-etching of WTi on a glass substrate.

(b) Negligible over-etching of WTi on a glass substrate.

Figure 4-31: Test patterns for estimating the undercutting amount of WTi.

4.7.2.1. Catalysis effect of Pt

It is highly suspected that the etching rate fluctuation is related to temperature increasing due to abnormal decomposition of H_2O_2. WTi etching process of the hot wire employs a commercially available 35% aqueous solution. The solution usually decomposes very slowly, less than 1% per year [166], but it is susceptible to transition metals and their ions that can catalyze the decomposition [167][168][169][170]. The decomposition formula is of the form:

$$H_2O_2(l) \rightarrow H_2O(l) + \frac{1}{2}O_2(g).$$ (4- 17)
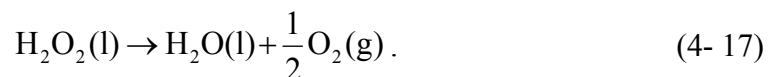
It is an exothermal reaction with an enthalpy of 98 kJ/mol [171]. Both materials comprising of hot wire sensors, Pt and WTi are able to catalyze the decomposition. It is reported that Pt is an efficient catalyst for H_2O_2. The intermediate product formation, Pt(O), can significantly reduce the activation energy of H_2O_2 decomposition [172][173]. The metallic W and W^{5+} peroxocomplexes that exist in the reaction product of H_2O_2 can also accelerate H_2O_2 decomposition [174][175]. In addition, Ti^{4+} is a known catalyst of a few chemical reactions where H_2O_2 involves [176].

Furthermore, Pt-catalyzed decomposition seems more active than WTi, which has been indicated by the difference in temperature rising rate in Pt-catalyzed H_2O_2 and WTi-catalyzed. The temperature of H_2O_2 is usually caused by the thermal imbalance

between the heat generation rate of H_2O_2 decomposition and the heat dissipation rate of the etcher. Figure 4-32 shows the temperature variation of 100 ml 35% H_2O_2 solution in a glass beaker without external heating source, where a WTi coated wafer and a Pt coated wafer are immersed, respectively. In the presence of Pt, the temperature of H_2O_2 solution rapidly rose by more than 50° C in 165 seconds, much faster than the occasion of the presence of WTi. It implies that Pt catalyzes H_2O_2 decomposition more aggressively than WTi, and Pt catalyzing effect is required to be considered.
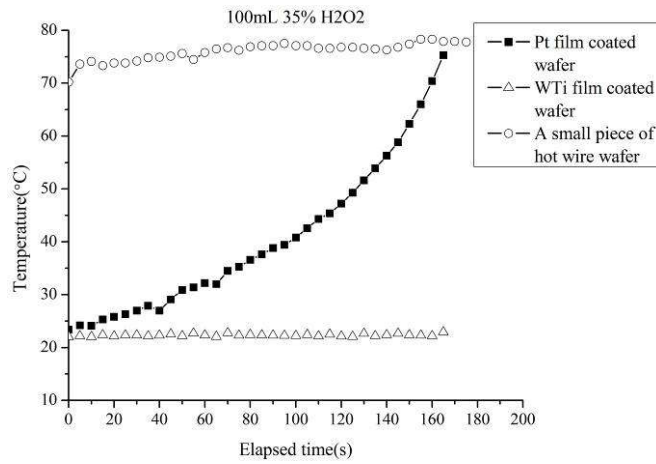

Figure 4-32: Temperature rise induced by catalyzed H_2O_2 decomposition.

The decomposition catalyzed by Pt is a first-order reaction that the reaction rate is linearly proportional to H_2O_2 concentration C_{H2O2} [172][177][178]. Therefore, the heat generation rate of H_2O_2 decomposition on the wafer is of the form:

$$\dot{Q}_{\mathrm{chem}} = A_{\mathrm{r}} e^{-E_a / R_g T} C_{\mathrm{H2O2}} A_{Pt} \Delta H_{\mathrm{chem}} \tag{4-18}$$

where A_r is the pre-exponential factor of the chemical reaction. The decomposition has an activation energy $E_a = 40 \pm 10$ kJ/mol [173], A_{Pt} is the surface area of Pt film to be exposed to H_2O_2; ΔH_{chem} is the reaction entropy.

The catalyzed decomposition may give rise to two contradictory effects on the etching rate of WTi in the H_2O_2 solution. One result is that the decomposition will reduce the H_2O_2 concentration so as to decelerate the etching rate. The other opposite effect is that the decomposition heat results in temperature rising so as to accelerate the etching rate. Whether the overall etching rate is up or down depends on which effects are dominant.

In practice, it more frequently occurs that the WTi etching rate is accelerated. Therefore it is

reasonable to assume that temperature rising effect dominates the overall process. To verify the assumption, the individual effect of temperature and concentration on the etching rate are estimated. Figure 4-33a shows the WTi etching rate at different solution temperatures and H_2O_2 concentrations. The temperature effect on the WTi etching rate complies with Arrhenius behavior, with an activation energy of 59 kJ/mol. Figure 4-33b shows that the rate is approximately proportional to the square root of H_2O_2 concentration. Figure 4-32 shows that Pt-catalyzed H_2O_2 was self-heated from 23° C to 76° C. Correspondingly, their decomposition rates are expected to increase more than 20 times. Meanwhile, the concentration caused by the decomposition merely declined by about 7% so that the WTi etching rate decline would be less than 11%. Therefore, temperature rising caused by Pt-catalyzed decomposition is the primary concern for the WTi etching process of the hot wire, other than concentration variation.
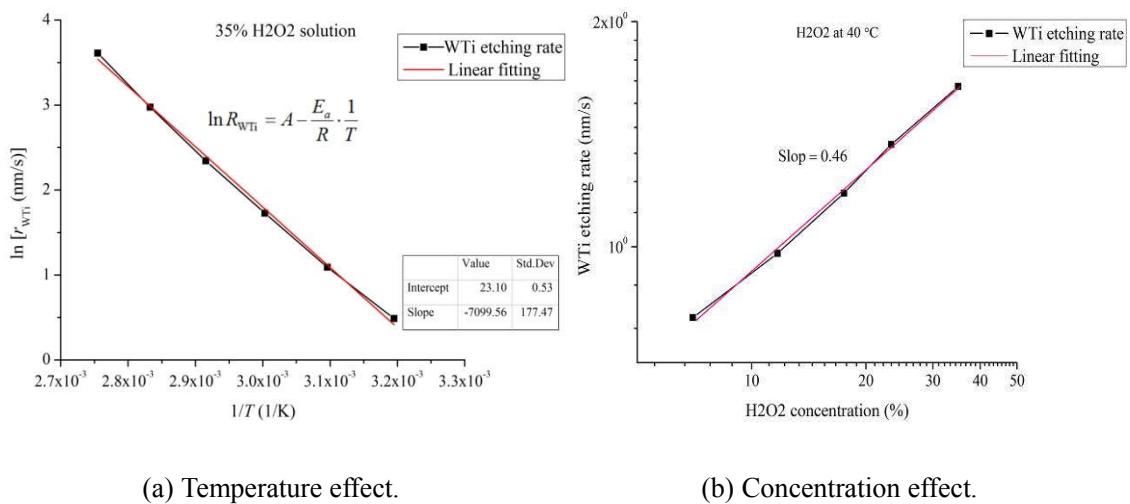

(a) Temperature effect. (b) Concentration effect.

Figure 4-33: The dependence of the WTi etching rate on temperature and concentration of H_2O_2.

4.7.2.2. Temperature controlling of WTi etching process

Semenov's thermal explosion methodology is an assistant of analysing thermal stability of an exothermic reaction system. It uses Semenov diagram to illustrate how the system responds to a temperature perturbation at equilibrium points between heat generation rate and dissipation rate. Figure 4-34 exemplifies the Semenov diagram of a typical exothermic chemical reaction. Anypoint at the red lines and blue lines represent the real-time heat generation rate and heat dissipation rate, respectively. They are the function of temperature. Since the temperature effect on the reaction rate complies with an Arrhenius behavior, the

heat generation rate of the reaction depends exponentially on the temperature. The slopes of the blue line are equal to the thermal conductance, and the intersection on the horizontal axis is equal to the ambient temperature. In Figure 4-34, the red line $\dot{Q}_{chem\,1}$ has no intersection with any blue lines, which means the heat generation rate is always more massive than the dissipation rate. The system temperature will keep rising; thus, the reaction rate will be exponentially increased further. It is called runaway reaction. The red line $\dot{Q}_{chem\,2}$ is tangent to the blue line U_3S_3 at an equilibrium point C. It means the temperature will permanently deviate from point C if it suffers any perturbation. The lines $\dot{Q}_{chem\,3}$ intersect with the blue lines U_3S_3 and U_2S_2 at the equilibrium points, A, B, A′, and B′, where the system is in equilibrium of heat generation and dissipation. Point A and A′ are the stable points of the system, and Point B and B′ are not. Any temperature below point B and B′ will spontaneously converge to point A and A′. Any disturbance around point B and point B′ will either ignite a runaway reaction or bring the temperature back to point A.

Therefore, point A and A′ are the preferred working temperature for an etching process. When a high etching rate is expected, a preferred setpoint of the etching tool should be below point B or B′. Usually, an external heat source is used to supplement the gap between blue lines and red lines. Thus, the temperature can be artificially kept at the set point. Otherwise, if any point above B or B′ is set to the working temperature of the etching tool, the etching rate will never be stable.
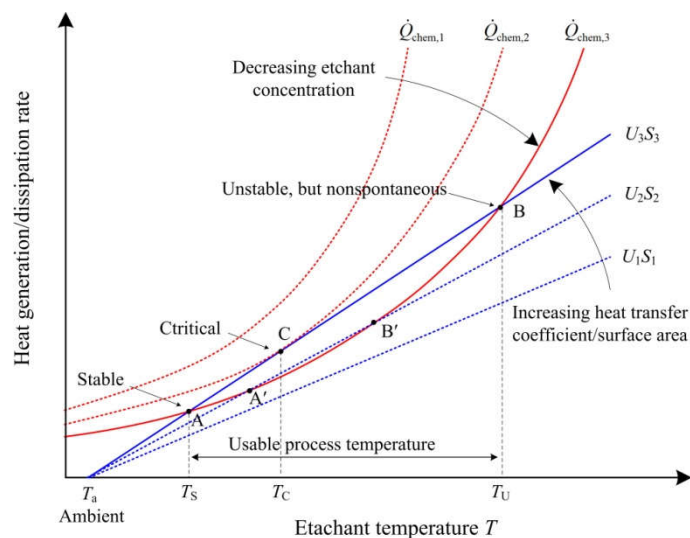

Figure 4-34: Semenov diagram of thermal stability of exothermic reaction.

We employed the Semenov diagram to analyze the WTi etching process. The primary aim is

to find the corresponding condition to achieve "point B" of WTi etcher. WTi etching is performed in a simple wet etcher, comprising of a glass beaker and a hot plate heater. The overall heat transfer diagram of the etcher is shown in Figure 4-35. It is assumed that solution evaporation is negligible below its boiling point, the etcher is cooled by convective as well as conductive heat transfer. Thus, the total heat dissipation rate is of the form:

$$\dot{Q_c} = \sum_i U_i S_i (T - T_a),$$
<div align="right">(4- 19)</div>

where U_i and S_i are thermal conductance and the cross-sectional area of every pathway of heat convection or conduction. The hot plate heater employs a PID temperature controlling algorithm to keep the temperature constant through tracking the difference of the setpoint and the real-time temperature of the H_2O_2 solution.
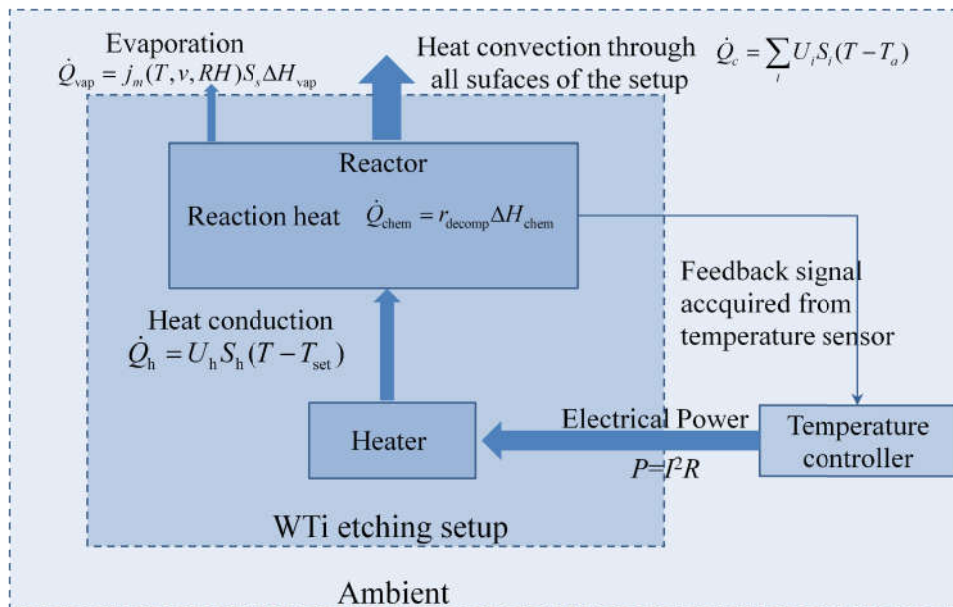

Figure 4-35: Heat transfer of schematic WTi etcher.

Obviously, there is no intersection for WTi etching under the previous condition, 35% H_2O_2, Nevertheless, according to H_2O_2 decomposition formula, as expressed by Eq. (4-18), the decomposition rate is proportional to H_2O_2 concentration, in this way, the slope of the decomposition heat rate can be reduced so that the intersection occurs. Out of this purpose, we start a trial that H_2O_2 concentration is reduced from 35% to 7%. When a test wafer coated with 78.5 cm^2 Pt film was immersed into the etcher filled with 300 ml 7% H_2O_2. The temperature monitoring results are shown in Figure 4-36. It shows the etcher has a stable point at 34°C. Because the WTi etching rate is too slow at this temperature, the process

temperature is increased to 45ºC to increase the etching rate. In this case, H_2O_2 temperature can be stabilized at the initial setpoint, 45ºC. Therefore, we choose this temperature as the setpoint of WTi etcher. Figure 4-37 shows the WTi undercutting amount of the test patterns under the chose condition. The undercutting amount increases in an approximately linear way with the etching time. A repeatable profile of test pattern is achieved under this condition, as shown in Figure 4-31b.
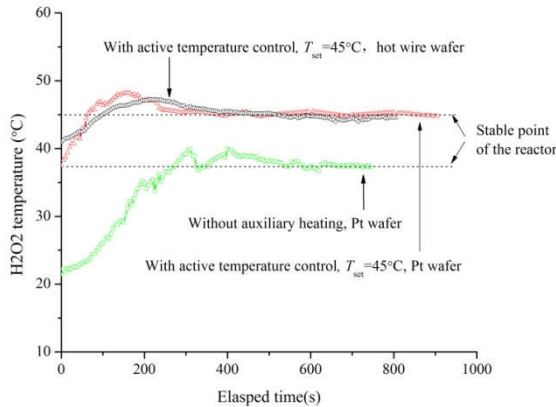

Figure 4-36: Temperature variation of H_2O_2 decomposition under different heating conditions.
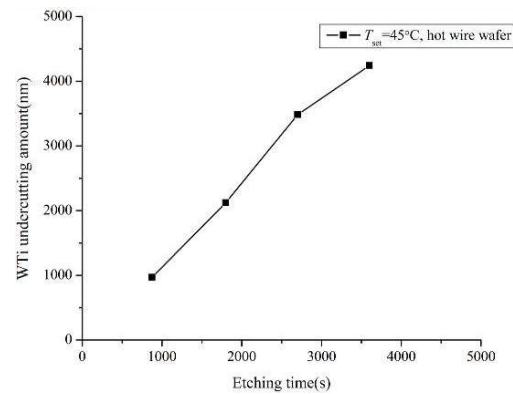
Figure 4-37: WTi undercutting with etching time at a stable point of the etcher with active temperature control.

4. 7. 3. Undercutting problems of Si prongs

Undercutting is one of the most common challenges in the anisotropic wet etching of Si. As a result of undercutting, the dimensions of the obtained structures have significant deviations from the original mask definition. In some cases, undercutting can be a favorable effect for releasing a suspended structure. In many other cases, just as in the example of prong fabrication, it should be reduced to the minimum. Generally, when an etching mask contains convex corners, or the mask edges do not align with {111} planes, undercutting will appear at the corners and edges. The emergence of fast etching planes at these sites is regarded as the root cause of undercutting [179][180]. The fastest etching planes forming the undercutting fronts, thus determine the profile of the resulting Si structures.

The fabrication of the hot wire sensor is performed on a {100} Si wafer. The mask edges of prong align to <110> directions and intersect to construct convex corners, where undercutting starts. If there were no undercutting, then the intersection lines of two adjacent {111} planes at a convex corner would be along <110> directions, and {110} planes would

be tangent to the protruded corners. The lines also belong to the vicinal planes of {110}, such as {221}, {331}, or {441}, which exhibit much higher etch rates than {111} planes. Therefore, the fastest etching plane among them becomes the etching front at the corners.
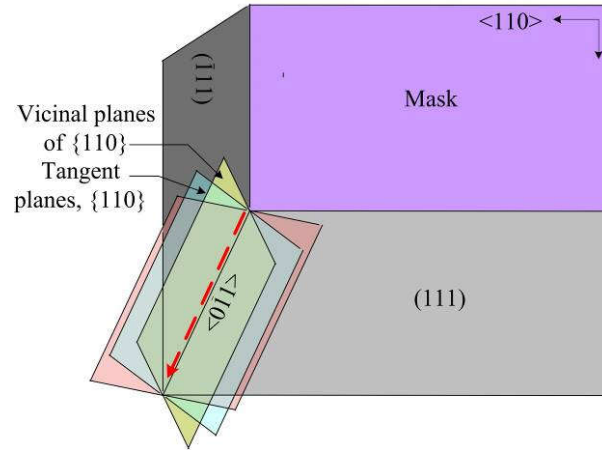

Figure 4-38: An explanation of undercutting at a convex corner of {100} Si.

In order to quantify the extent of undercutting of Si prongs the undercutting ratio of the etching is defined as

$$r_u = \frac{d_{<110>}}{d_{\{100\}}}$$

(4- 20)

where $d_{<110>}$ is undercutting distances along the <110> direction; $d_{\{100\}}$ is the depth that has been already etched in {100} planes, as illustrated in Figure 4-39. The fastest planes that emerged at the convex corner of two {111} planes are denoted by {*hkl*}, where the exact values of *h, k, l* are determined by actual etching conditions, such as concentration, temperature, and surfactants. The intersection angle of the fastest etching planes and the substrate are denoted by θ_3. Thus, the undercutting ratio r_u is further expressed as

$$r_u = \frac{d_{<110>}}{d_{\{100\}}} = \frac{r_{\{hkl\}}}{r_{\{100\}}} \cdot \frac{1}{\sin\theta_1 \sin\theta_3}$$

(4- 21)

where $r_{\{hkl\}}$ and $r_{\{100\}}$ are the etching rates at the {*hkl*} and {100} planes; and θ_1 is the angles between <110> and <0*lk*>.
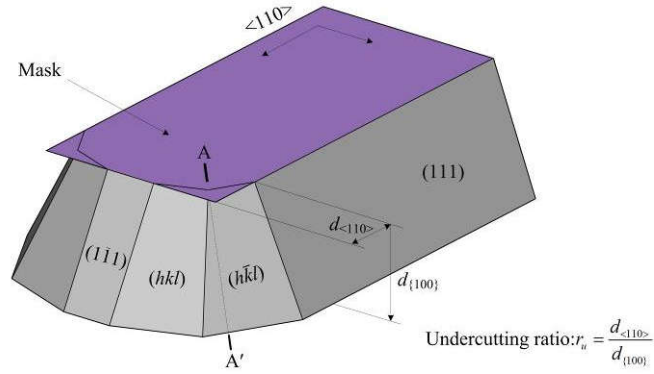
(a) The schematic undercutting of a convex corner.
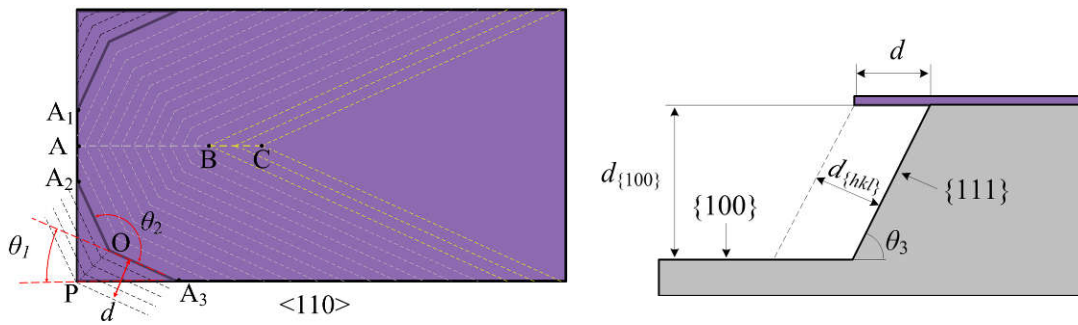
(b) Top view   (c) A-A' cross-sectional view

Figure 4-39: The schematic definition of the undercutting ratio.

In Figure 4-39b, it should be emphasized that if point A_1 and A_2 meet at point A, then undercutting will start from point A. Undercutting will be further accelerated since point B. Hence, the merging of point A_1 and A_2 at point A is the critical point to start undercutting of prong tip. The elapsed etching time to reach point A is

$$t_A = \frac{0.5 l_{\mathrm{SiNx}} \sin\theta_1 \sin\theta_3}{R_{\{hkl\}}}, \qquad (4\text{-}22)$$

and the critical etching amount of {100} plane at t_A is

$$d_{\{100\},c} = \frac{0.5 l_{\mathrm{SiNx}}}{r_u}. \qquad (4\text{-}23)$$

Therefore, as long as the desired thickness of the prong is larger than $0.5 l_{\mathrm{SiN_x}}/r_u$, the undercutting will take place.

Many compensation techniques have been developed to reduce or eliminate undercutting,

which adds some compensation shapes to the etching mask [181][182]. However, they are not applicable to the prongs of hot wire sensors, where the aerodynamic profiles of the sensors are taken into consideration. The extra compensation structure will occupy some part of the probing space and may interfere with the investigated flow field.
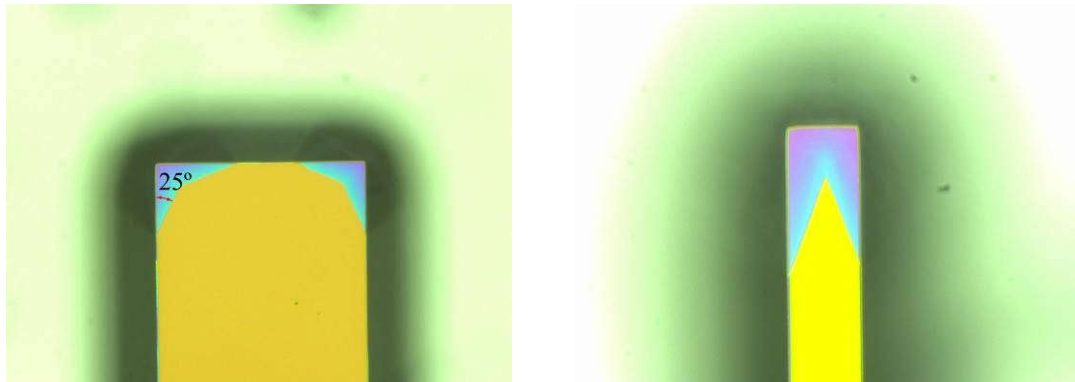
(a) Before the fastest etching planes merge at a horizontal edge.

(b) After the fastest etching planes merge and more severe undercutting develops.

Figure 4-40: Undercutting of the test structures of the prong when being etched by 25% TMAH at 75°C.

Eq. (4-21) reveals that when the etching rate ratio of the $\{hkl\}$ and $\{100\}$ planes is reduced, the undercutting of convex corners will be improved. Recent works suggest that the addition of small amounts of a surfactant in the TMAH solution can reduce undercutting significantly. The surfactant severely suppresses the etch rates of the fastest etching planes, thus reduces the rate ratio of $r_{\{hkl\}}$ and $r_{\{100\}}$. Various ionic and non-ionic surfactants have been investigated, such as ASPEG, alcohols, PEG, Triton, and X-100 [183][184][185].
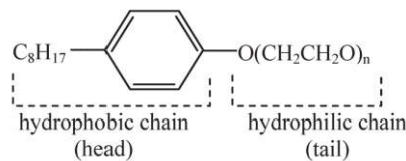

Figure 4-41: Triton X-100 molecular formula.

Triton X-100 has been reported to be able to significantly reduce the undercutting at mask-corners [186][187]. Triton X-100 is a non-ionic surfactant and has a chemical formula, as illustrated in Figure 4-41. It contains a hydrophobic head and a hydrophilic tail. The outermost atoms of fresh exposed Si surfaces are mainly terminated by hydrogen (H). The surfaces are highly hydrophobic. When a small amount of Triton is added to TMAH, the

hydrophobic heads are preferentially adsorbed to the hydrophobic surface, where several adsorption mechanisms may be involved, for instance, hydrophobic [188]. Obviously, the difference of Si surface properties will result in anisotropy of surfactant absorption. Relative hydrophobicity of Si surface is the first property to be considered, which is thought to be related to the surface density of H-termination on Si surface [189]. Gosalvez concluded that the surface density of H-termination was inversely proportional to absorbed surfactant density. For example, the surface density of H-termination {110} planes $2\sqrt{2}/a^2$, is larger than the density on {100} planes, $4/a^2$, where a represents the lattice constant of the Si crystal. Some measurements of Triton adsorption thickness and adsorption strength demonstrated {110} planes adsorbed thicker and denser Triton layer than {100} planes [190]. The surface densities of H-termination and absorption density at the different orientations are estimated, as shown in Figure 4-43.
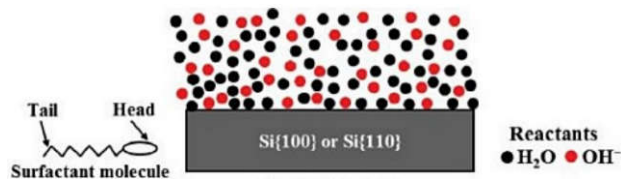
(a) TMAH only
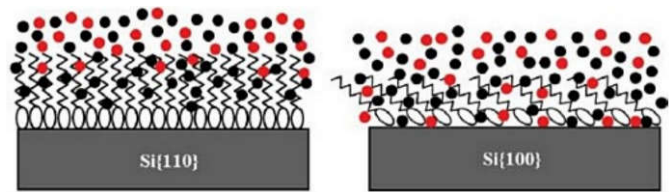
(b) TMAH+surfactant

Figure 4-42: A simple model representing the wet etching on Si surface in TMAH (a) without surfactant and (b) with surfactant [191].

As a result of the absorption, Si surface is covered by a thin Triton molecules layer. It retards the transportation of the etchant and products through the interface of Si and bulk TMAH solution. The etching rate is thereby reduced. Many experiments implied that the reduction depended on Si surface orientations due to the anisotropy of surfactant absorption densities. The etching rates were dramatically decreased at {110} and vicinal planes that are the fastest etching planes for pure TMAH, but declined relatively less at {100} and vicinal

planes. Namingly, the ratio of $r_{\{hkl\}}$ and $r_{\{100\}}$ is reduced. According to Eq. (4-21), the undercutting ratio r_u is therefore decreased.
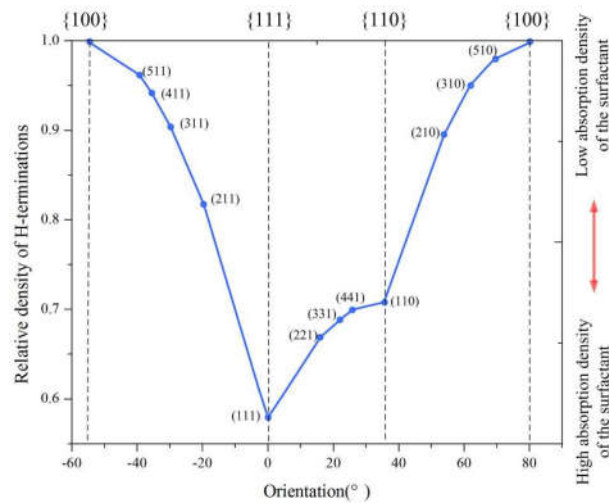

Figure 4-43: The density of H-terminations at different planes, normalized by the density at Si{100} plane [190].

In the bulk micromachining of the sensor prong, the surfactant Triton X-100 is added to TMAH solution in order to improve the undercutting at the prong tip. Since concentration and temperature are critical parameters to affect the species diffusion through the surfactant layer and etching rate, their contributions to the etching rate and undercutting ratio were tested as well.

The {100} Si wafers with rectangular test patterns of nitride were etched by 0.5% Triton-added and pure TMAH solution with concentrations of 5%, 15%, and 25%, respectively. Their etching rate and undercutting ratio were measured, and the results are presented in Figure 4-44. The resultant profiles of the test patterns are shown in Figure 4-45. Figure 4-44 shows when Triton is added to TMAH, both etching rates of {100} planes and the undercutting ratio at the convex corner are reduced. The undercutting ratio reduction is particularly significant at 25% TMAH. Fortunately, the rate declination is minor. It implies increasing the concentration of Triton-added TMAH is the preferential option to reduce the undercutting ratio.

To investigate the temperature effect on etching rate and undercutting, the test patterns were also etched by 0.5% Triton-added TMAH at the temperature of 60ºC, 80ºC, and 95ºC. The result is shown in Figure 4-46. When the temperature was raised, all etching rates of {100} planes are increased, but the undercutting ratio varies slightly. In conclusion, an optimum

condition for Si prong etching is obtained: Triton added 25% TMAH at 95º C.
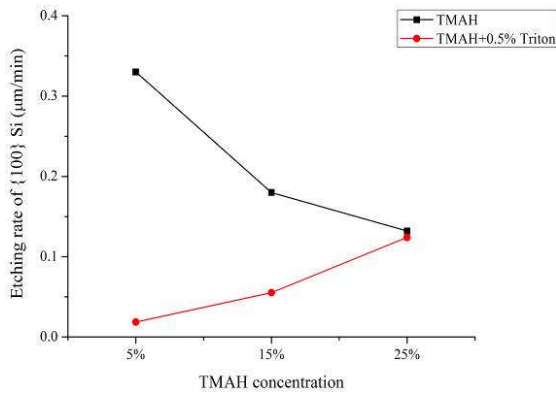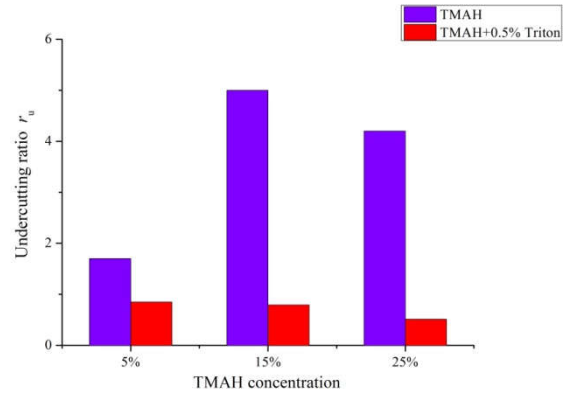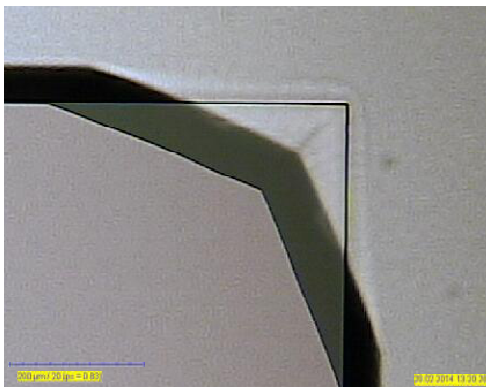

(a) Etching rate.   (b) Undercutting ratio.

Figure 4-44: Surfactant effect on etching rate and undercutting ratio.

(a) Pure TMAH   (b) 5% TMAH + 0.5% Triton
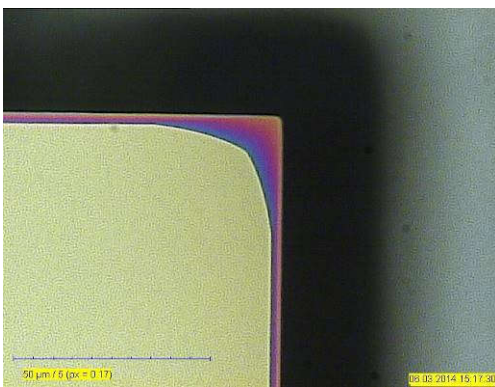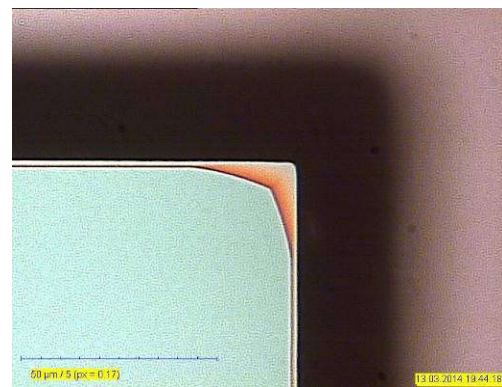
(c) 15% TMAH + 0.5% Triton   (d) 25% TMAH + 0.5% Triton

Figure 4-45: Surfactant effect on the undercutting of test patterns on {100} Si.
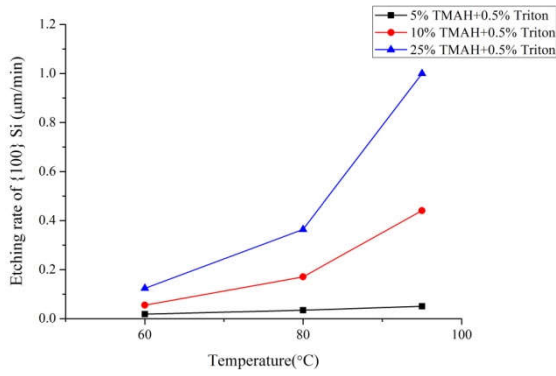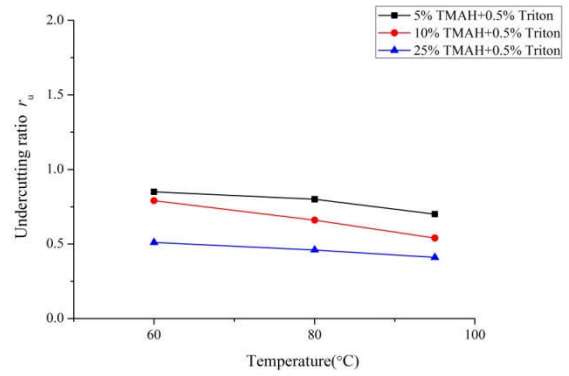
(a) Etching rate   (b) Undercutting ratio

Figure 4-46: The effect of temperature and concentration on etching

We applied this optimized etching condition to the actual fabrication process of hot wire prongs. The resultant profiles of prong tips are shown in Figure 4-47. Compared with the profile of the prongs etched by KOH in Figure 4-29, the undercutting is improved significantly.
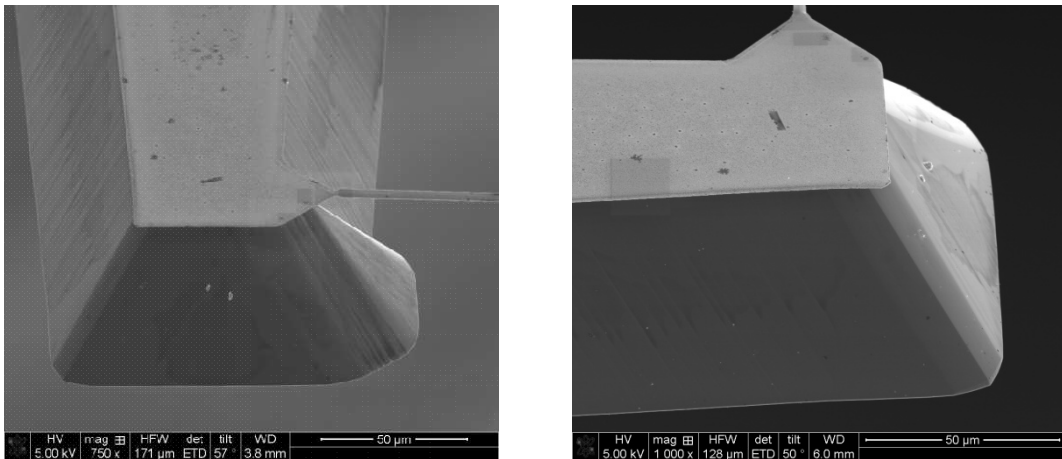
Figure 4-47: SEM images of a prong tip with improved wet anisotropic etching.

Chapter 5   Circuit design and analysis

5.1. Circuit design

5.1.1. Implementation of constant temperature circuit

When a hot wire sensor is working in constant temperature mode, its bandwidth can be expanded substantially[26]. In our work, the developed microfabricated hot wire is also driven by a constant temperature circuit. Figure 5-1 illustrates the schematic diagram and the finished circuit. In the circuit, an operational amplifier with multiple gain stages and tunable offset voltage is used to magnify the voltage difference of the Wheatstone resistance bridge. The circuit behaves as a high order system, where the system damping can significantly influence its performance. The circuit has a damping adjusting function. A square wave electrical signal is injected into the amplifier. The circuit damping is optimized by adjusting the offset voltage of the amplifier, meanwhile monitoring the response of the square wave.
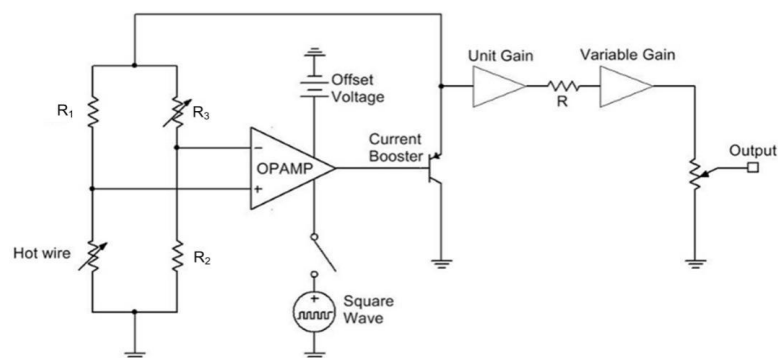
(a) Schematic diagram of constant temperature circuit.

(b) The completed constant temperature circuit.

Figure 5-1: Constant temperature circuit as designed.

5.1.2. Equivalent behavior model of hot wire

Electrical circuit design has been tremendously assisted by various electronic design automation (EDA) programs. In the stage of schematic design, signal prediction, and integrity verification usually employ SPICE, which is a general-purpose electronic circuit simulator. Every vendor of electronic components has built up their own models that describe their components' behavior. Based on the netlist file of the circuit that records how components were connected in a circuit, SPICE can automatically create a set of differential equations for the circuit by Kirchhoff's current law and solve them by numerical methods, e.g., by the Newton-Raphson method.

In our case, NI Multisim that contains a SPICE core, was used to execute DC, AC, and transient analysis for the intended constant temperature circuit. Unfortunately, the simulator did not contain such a model for a hot wire. COMSOL can fulfill simulation tasks for a simple circuit with a few components. When circuit complexity is increased, such as by including multistage amplification, or damping tuning, then SPICE simulation becomes a good alternative. Inspired by electro-thermal analogy, S. Yaakov used a resistor-capacitor device to establish a SPICE model for a heated tungsten wire [192]. R. Heyd took end conduction loss into account and proposed a transfer function controlled voltage source to simulate the temperature response of a hot wire excited by a transient current [193]. Both models presupposed a constant heat convection coefficient. We developed a variable resistor-capacitor device to simulate the hot wire, which can be used to estimate a transient heat convection coefficient of a hot wire and the dynamic response of the constant temperature circuit. Consequently, it significantly simplified the design complexity of a constant temperature circuit.

Considering the diffusion process of heat transfer driven by temperature difference and electrical charge driven by voltage difference, heat flux and temperature can be analogous to the current and voltage. Just as the electrical resistance is equal to the ratio of voltage to current, the thermal resistance is thereby defined as the ratio of temperature to heat flux. Furthermore, electrical current through a capacitor is expressed as $I = C \cdot \mathrm{d}U/\mathrm{d}t$, and heat transfer rate of a hot wire is $\dot{Q} = C_p m \cdot \mathrm{d}T/\mathrm{d}t$, Therefore, $C_p m$ is analogous to capacitance, which is called the heat capacitance.

Table 5-1: Analogy between thermal quantities and electrical quantities.

Thermal quantity	Electrical quantity
Temperature T	Voltage U
Heat flux $\dot{Q}$	Current I
Thermal resistance $1/h_c A$	Resistance R
Thermal capacitance $C_p m$	Capacitance C

In hot wire circuit simulation, a SPICE model is established, using already existing components in the NI Multisim library, as shown in Figure 5-2. A current source I2 is used as an input to the model, representing an arbitrary flow velocity. Two terminals, "HWA+" and "HWA-", are connected to the temperature controlling circuit. The controlled current source I1 and controlled voltage source V1 are used to calculate real-time heating power consumption and resistance of the hot wire, respectively. Capacitor C1 and controlled voltage source V0 represent the thermal capacitance and thermal resistance. The transient temperature of the hot wire can be acquired by measuring the potential on the top electrode of capacitor C1 (Temp meas terminal).
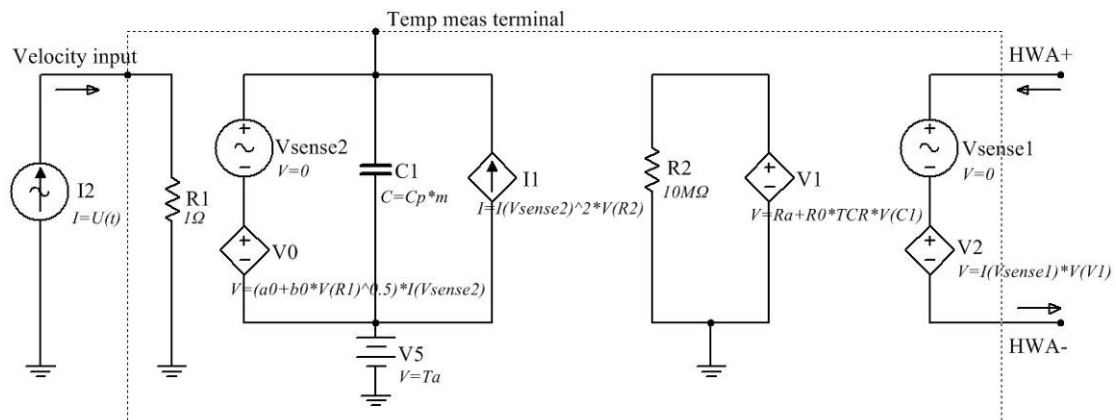

Figure 5-2: A SPICE model of the hot wire sensor.

The model is compacted to a single component, which is subsequently supplemented to the component library of NI Multisim. Figures 5-3a and 5-3b illustrate the temperature simulation result when constant voltages and a sinusoidal voltage (1 kHz, 5 mV) are

individually applied to a hot wire placed in airflow at 10 m/s. Figure 5-3c and 5-3d show static and transient response of a constant current hot wire when constant and sinusoidal velocities are applied to it. All figures show that the simulation results obtained from the SPICE model almost perfectly match the ones from COMSOL simulation.
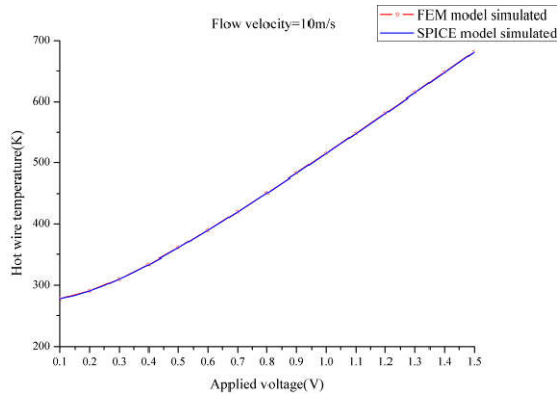
(a) The stationary temperatures of hot wire when voltages are applied to it (constant convection condition).
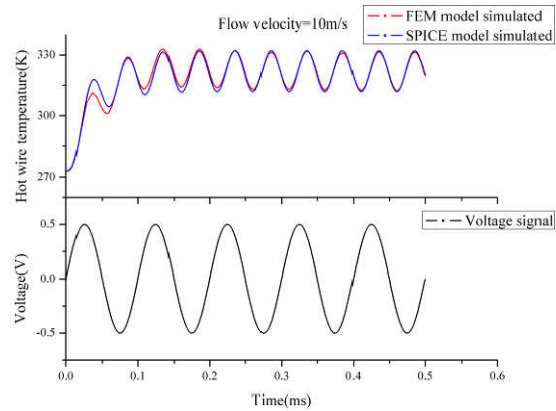
(b) The transient temperature of a hot wire when voltages are applied to it (constant convection condition).
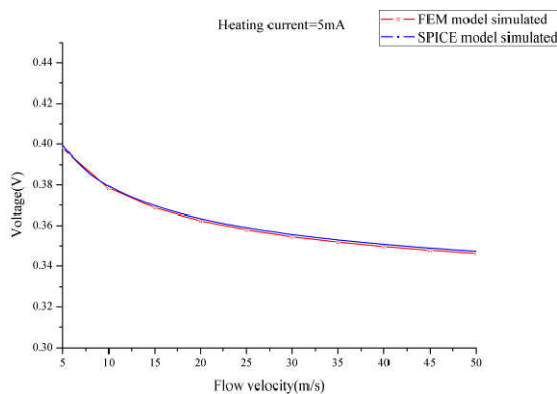
(c) The stationary response of hot wire to velocity (constant current mode).
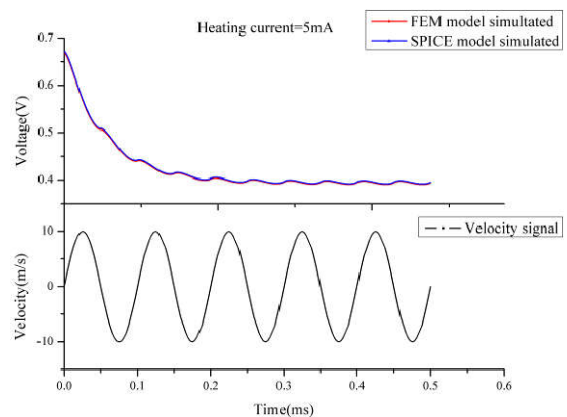
(d) The transient response of hot wire to velocity (constant current mode).

Figure 5-3: Comparison of results obtained by SPICE and by COMSOL simulation.

5.2. Circuit stability analysis

As mentioned in Chapter 2, a hot wire with constant temperature controlling behaves as a second or high order control system, mainly depending on the amplifier order. The system

may encounter instability problems when choosing inappropriate circuit parameter settings. It is reported that constant temperature circuit oscillation of miniaturized hot wires have frustrated many users [194]. To analyze circuit parameter effects on stability and bandwidth, a generalized locus root method, together with circuit simulation, are used.

5.2.1. Transfer function of constant temperature hot wire circuit with single pole amplifier

The simplest operational amplifier is a single-pole amplifier that behaves as a first-order system. Its transfer function is of the form:

$$A_a(s) = \frac{A_o}{\tau_a s + 1},$$ (5-1)

where A_o and τ_a are the open-loop gain of the operational amplifier and its time constant. The parameters in Eq. (2-63) are assigned: $K_a = A_o$, $P(s) = 1$, and $Q(s) = \tau_a s + 1$. Substituting A_o for K_a in Eq. (2-64), the current across the hot wire is expressed as

$$\overline{I}_1 = \frac{A_o E_b (R_2 + R_3)}{A_o \Delta R + \Sigma R}.$$ (5-2)

Substituting K_a, $P(s)$, and $Q(s)$ of Eq. (2-66), the transfer function of constant temperature circuit with a single-pole amplifier is of the form

$$\frac{E'(s)}{h'_c(s)} =$$

$$\frac{\overline{I}_1 A_o K_v R_1 (R_2 + R_3)}{\tau_a \tau_w \Sigma R s^2 + [(\tau_a + \tau_w)\Sigma R + \overline{I}_1 K_i \tau_a (R_2 + R_3) + \tau_w A_o \Delta R]s + \Sigma R + \overline{I}_1 K_i (R_2 + R_3) + A_o (\Delta R + \overline{I}_1 K_i R_3)},$$ (5-3)

5.2.2. Root locus and circuit analysis

Root locus method is a graphical approach to investigate the effect of a single variable on the system stability. Classical control theory asserts a system is stable only if all poles of the system transfer function are located at the left half s-plane. The root locus method constructs a root locus equation based on the transfer function in order to figure out a motion trail of the system poles in the complex s-plane as the variable is continuously changed. To visually observe the tail, whether cross over the image axis, the system stability with respect to the specific variable can be known. It also used to decide the critical condition of system

stability.

In reality, it is complicated to obtain an explicit expression of the transfer function of an actual amplifier in which multiple stage amplifiers, including many configuration parameters usually integrated. As a result, directly deriving the root locus equation becomes impractical. On the other hand, EDA tools can conveniently estimate the circuit output under a specific parameter configuration, but they rarely give a full view or trend of the parameter's effect. We combined these two methods: (1) Firstly, using root locus method to plot poles trail of a simplified circuit so as to estimate the effect of those concerned components' parameters on circuit stability. (2) After that, extrapolating rules obtained from the previous simple case to the actual circuit of design, and verifying them in EDA tools. Instead of directly deriving root locus equation to plot poles trail, it is achieved by the following procedure: (1) Numerical arrays composed of specific values were assigned to the variable to be investigated. Therefore, a bunch of transfer functions is constructed; (2) Solving poles of every transfer functions; (3) Plotting poles in the s-plane and connect poles with lines. The lines represent the poles trail when the variable is continuously changed. The procedure above was performed in Matlab.

Three parameters that may affect the circuit stability have been investigated: offset voltage E_b, gain-bandwidth product GBP and resistance ratio of Wheatstone bridge R_2 and R_3 arms. Figure 5-4a illustrates the root locus with respect to offset voltage variation. It is assumed a Pt hot wire with a dimension of 500 μm × 3 μm × 300 nm is operated at 1.05 overheating ratio and 10 m/s airflow. The figure shows when the offset voltage is decreased, the poles' locus of the hot wire's transfer function will move forward to the image axis of s-plane. It indicates that the damping is reduced when the voltage is decreasing. It also implies that there might exist an offset voltage, at which the optimum damping condition is achieved (For the second system, the optimum damping ratio is close to 0.707, at which a system stimulated by a step input fastest reaches its steady state within 2% overshooting tolerance).

As shown in Figure 5-4b, when the applied offset voltage on the amplifier is reduced, the output oscillations of the dedicated circuit decay more slowly until the circuit becomes unstable at 0.04 mV. For a flow velocity of 10 m/s, there is an optimum offset voltage at 0.9 mV, at which the circuit output with respect to a step velocity input rapidly reaches its steady state value.
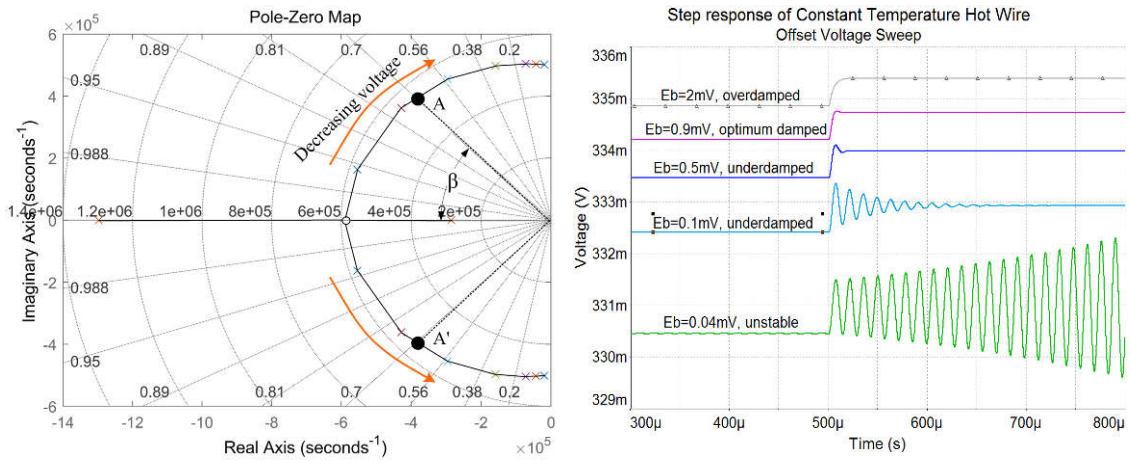
(a) Root locus with offset voltage variation.

(b) Step response of the circuit with offset voltage variation.
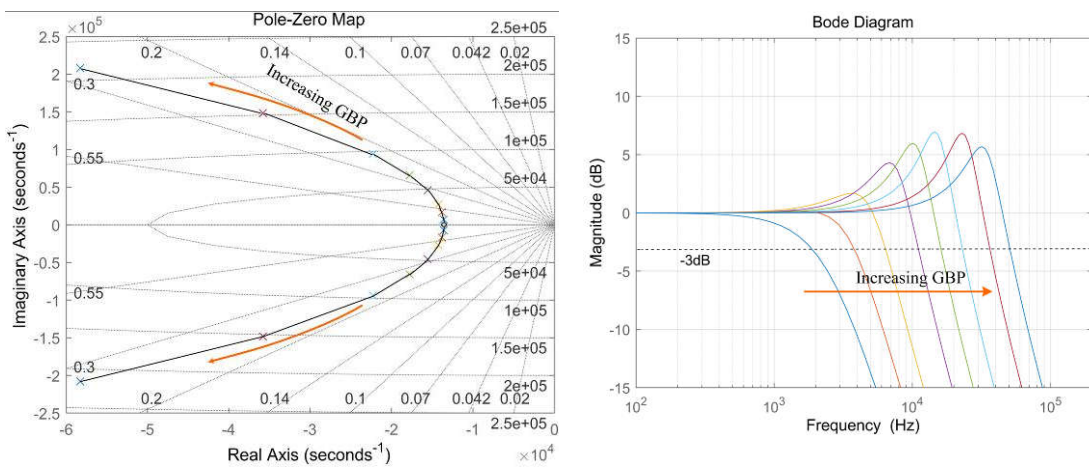
Figure 5-4: Effect of the offset voltage.

As discussed in Chapter 3, increasing overheating ratio can reduce the time constant of the hot wire, which can be realized by adjusting the resistance ratio of Wheatstone bridge arm of constant temperature circuit, $R_2 : R_3$. The gain of the operational amplifier is usually huge. Therefore, the bridge is almost in balance (perfect balance condition: $R_w : R_1 = R_2 : R_3$). Figure 5-5a illustrates the root locus of the circuit with respect to varying overheating ratio. When $R_2 : R_3$ is increased, the distance between the poles to the origin of s-plane is increased as well. It implies that the characteristic frequency is increased. Meanwhile, the poles are rapidly close to the image axis of s-plane. It represents the circuit will undergo more oscillations and need longer transition time before it reaches the stationary state. The circuit simulation also demonstrates that larger $R_2 : R_3$ ratios lead to less damping. Eventually, the circuit becomes unstable after exceeding a critical overheating ratio (for this case in Figure 5-5b, the ratio is approximately 1.31).

The gain-bandwidth-product (GBP) is an essential characteristic parameter for an operational amplifier. Its effect on stability is investigated, as illustrated in Figure 5-6a and 5-6b. When GBP increases, the system poles tend to the negative real axis, and the system obtains a broader passband. In addition, damping variation is less sensitive to GBP than offset voltage and overheating ratio.
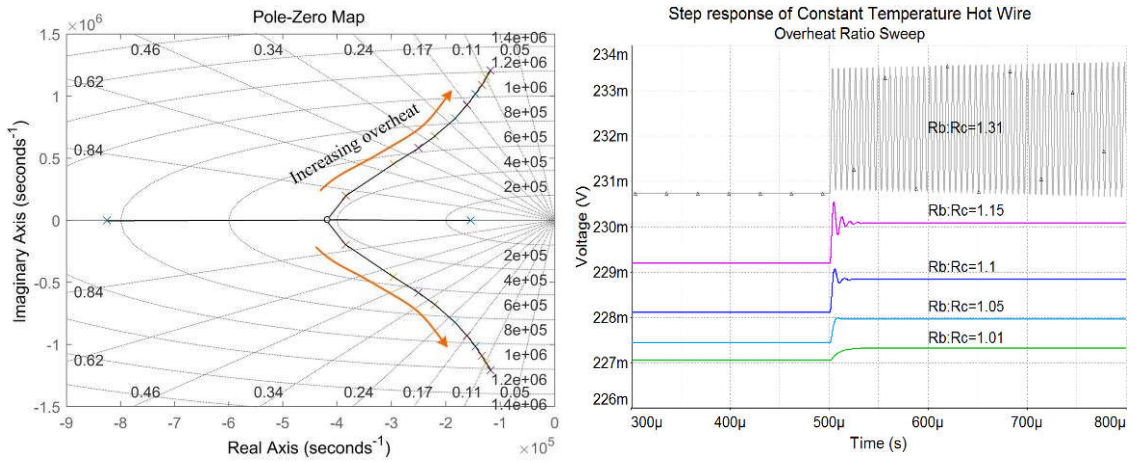
(a) Root locus with overheating ratio variation.

(b) Step response of the circuit with overheating ratio variation.

Figure 5-5: Effect of overheating ratio.

(a) Root locus with op-amp GBP variation.

(b) Step response of the circuit with op-amp GBP variation.

Figure 5-6: Effect of the gain-bandwidth product of the operational amplifier.

5.3. Damping optimization and square wave test

If the voltage offset that is applied to the amplifier (In Figure 2-15) contains a time-varying part E_b', the transient equation of Eq. (2-62) is expressed as

$$E'_o = I'_1(R_1 + \overline{R}_w) + \overline{I}_1 R'_w$$
$$E'_o = I'_2(R_2 + R_3)$$
$$E'_i = I'_1 R_1 - I'_2 R_3 + E'_b$$
$$E'_o = K_a E'_i$$

(5- 4)

Assuming flow convection has no fluctuation, $h' = 0$, in this case, the fluctuation of resistance is attributed to the current fluctuation, according to Eq. (2-55), there is

$$R'_w(s) = \frac{K_i}{1 + \tau_w s} I'_1(s).$$

(5- 5)

Combing Eq. (5-3) and Eq. (5-4), an expression of output voltage in the Laplace domain is solved:

$$\frac{E'_o(s)}{E'_b(s)} = \frac{(R_2 + R_3)[I'_1 K_i + (R_1 + \overline{R}_w)(\tau_w s + 1)]Q(s)}{\Sigma R(\tau_w s + 1)Q(s) + \overline{I}_1 K_i(R_2 + R_3)Q(s) + K_a P(s)\Delta R(\tau_w s + 1) + \overline{I}_1 K_i K_a R_3 P(s)}.$$

(5- 6)

Eq. (5-5) is the transfer function that regards voltage as the function of circuit output voltage, while Eq. (2-66) is the transfer function that regards velocity as the circuit output voltage. Both transfer functions have an identical denominator. Thus they have the same poles, which means they have the identical characteristic frequency and ringing frequency, damping ratio. It is the theoretical basis of a square wave test that a square wave voltage, to replace a step velocity, is input to the circuit to estimate cutoff frequency. Freymuth used it to optimize the damping of constant temperature circuit and proposed an empiric formula to calculate -3dB cutoff frequency [195][196]:

$$f_c = \frac{1}{1.3\tau_s}$$

(5- 7)

where τ_s is a time parameter that is obtained from the time response to a square wave perturbation. It is defined as the required time for the magnitude of the step response to falling to a value of 3% of its maximum peak under optimum damping conditions (see Figure 5-7).

$$f_c = \frac{1}{1.3\tau_s}$$
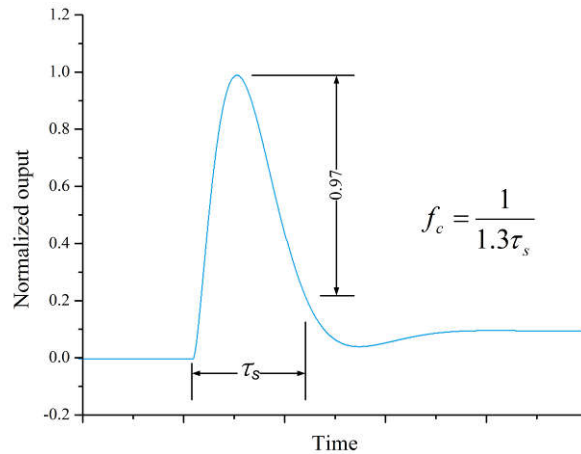
Figure 5-7: Time response to a voltage perturbation at optimum damping conditions.

To exemplify a square wave test, it is assumed that a Pt hot wire, as discussed in Figure 5-4b, is connected to the actual circuit of designed. The simulation is implemented in NI Multisim integrated a SPICE model of the hot wire. Figure 5-8a illustrates the response of the circuit in the time domain to square wave stimulation. By adjusting the offset voltage, the signal oscillation attenuation speed can be varied. At an offset voltage of 0.9 mV, the fastest response to a square wave within an allowable overshooting occurs. Meanwhile, at this offset voltage, the circuit signal in the frequency domain exhibits the maximum bandwidth with respect to the velocity stimulation, as shown in Figure 5-8b.
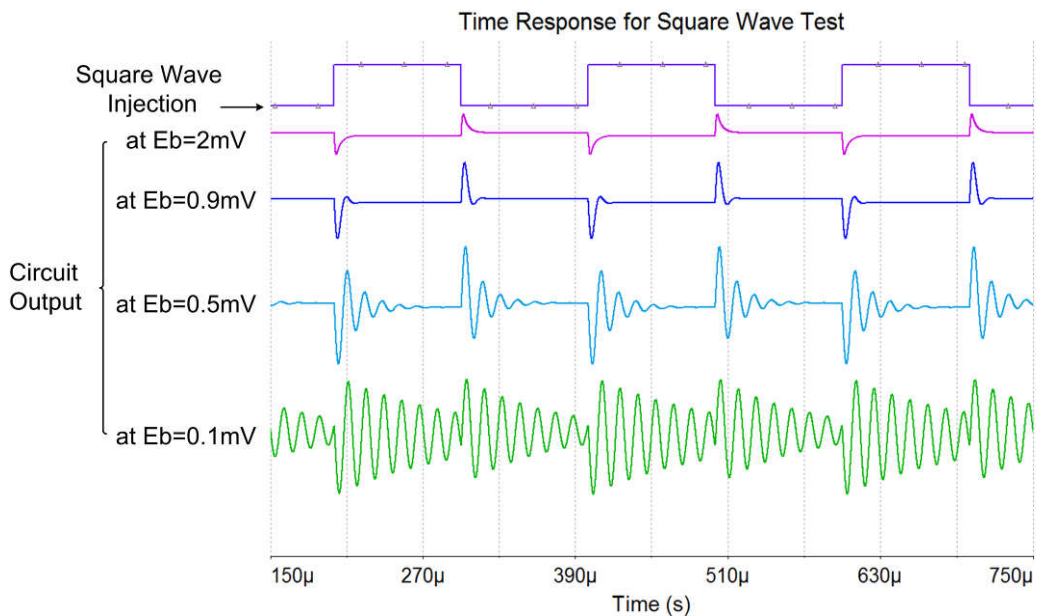
(a) Time response of the constant temperature hot wire circuit to an electrical square wave.
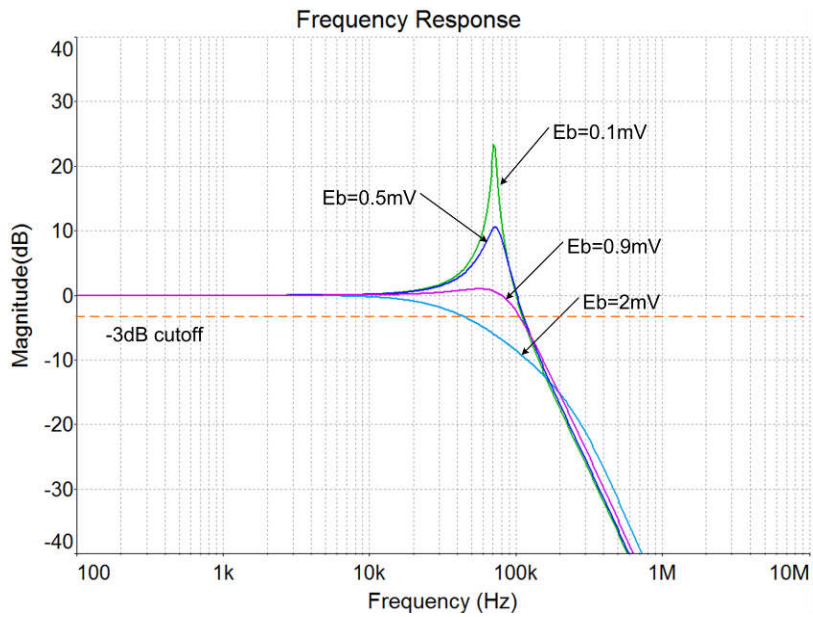
(b) Frequency response to flow velocity.

Figure 5-8: Damping of constant temperature circuit.

The offset voltage corresponding to the optimum damping condition of square wave stimulation coincides with the one corresponding to the optimum damping condition of velocity stimulation, as mentioned in Figure 5-4b. It indicates that the square wave test is a reliable method to inspect the damping status of a constant temperature circuit.

Chapter 6　Hot wire sensor characterization

6. 1. Calibration setup

The calibration of microfabricated hot wires has been performed in a wind tunnel apparatus. The response to velocity magnitude and direction of the airflow was measured, including a square wave test. The calibration setup is illustrated in Figure 6-1.

In the wind tunnel, a rotary mechanical arm is driven by a stepper motor, which has a rotation center at the left end of the arm. The arm itself can also be turned manually by 0º and 90º around its axis. Hot wire sensors of interest integrated on a sub-mounting package are attached to the left end of the arm and are rotated together with the arm. Referring to the definitions of "pitch" and "yaw" of aircraft flying attitude, the angles included by the arm's axis and the airflow are defined as the sensor's pitch and yaw when sensor substrate planes are set to 0º and 90º positions, individually. Two static pressure tubes with high accuracy pressure transducers are connected to the inlet to acquire its local static pressure. Bernoulli equation and the continuity equation are given by:

$$p_1 - p_2 = \frac{1}{2}\rho_{air}\left(V_{p2}^2 - V_{p1}^2\right),\tag{6-1}$$

$$d_1 V_{p1} = d_2 V_{p2},\tag{6-2}$$

where, p_1, p_2, V_{p1}, V_{p2}, d_1, d_2 are the static pressure, air velocity, and diameter of two acquisition positions at the inlet. ρ_{air} is the air density. Combining Eq. (6-1) and Eq. (6-2), velocity V_{p2} is expressed in the form:

$$V_{p2} = \sqrt{2}d_1\sqrt{\frac{p_1 - p_2}{\rho_{air}(d_1^2 - d_2^2)}}.\tag{6-3}$$

The differential pressure sensor can measure $p_1 - p_2$, and transform it into the inlet velocity. During calibration, the maximum pressure difference can reach around 10 mbar, which corresponds to the maximum air velocity of 40 m/s.

In addition, the calibration setup contains a square wave test module. It comprises a function generator and an oscilloscope, which are used to generate a square wave voltage to stimulate

hot wires working in constant temperature mode and observe their corresponding waveform, respectively.
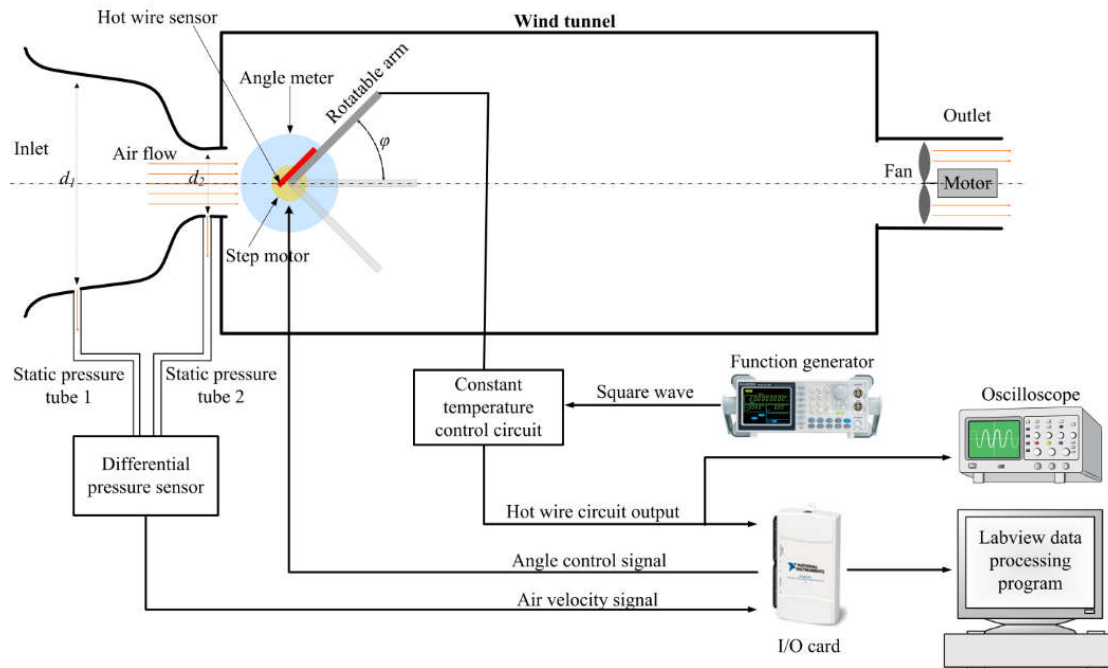
(a) Schematic diagram of the hot wire calibration apparatus.
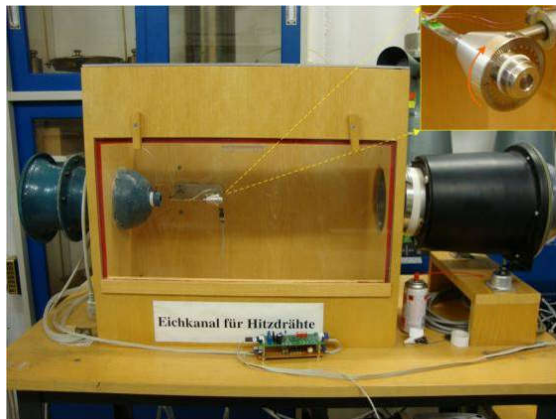
(b) The wind tunnel for hot wire calibration.   (c) A hot wire attached to a rotary arm at 0º pitch.

(d) A hot wire attached to a rotary arm at 45º pitch.

(e) A hot wire with the sub-mounting package.

Figure 6-1: Hot wire calibration apparatus.

6.2. Square wave test

One of the key issues for hot wire calibration is its bandwidth, which is decisive for the application scenario in turbulence measurement. However, it is quite difficult to calibrate the bandwidth directly. One barrier is due to the absence of a controllable oscillating flow source with sufficiently high frequency and known amplitude [197]. Therefore, indirect methods such as modulated microwave heating, square wave test, or modulated laser heating, have been invented to measure the frequency response of hot wire sensor [198][195][199]. Due to its ease of operation, the square wave test is the most popular alternative, which can indirectly estimate the cutoff frequency of a hot wire. In addition, as mentioned in Chapter 5, inappropriate damping condition for constant temperature circuit will cause circuit oscillation. The square wave test opens access to observe the damping condition of the circuit during damping optimization.

The square wave test of the fabricated hot wire sensors was implemented in the wind tunnel. A square wave signal of 10 kHz was generated by a function generator and was injected in the offset balance pin of the operational amplifier in the circuit, as illustrated in Figure 5-1. The voltage output of the constant temperature circuit under different offset voltages is demonstrated in Figure 6-2. The voltage overshooting decays with injected offset voltage varying, and the optimum damping can be achieved at a certain offset voltage.

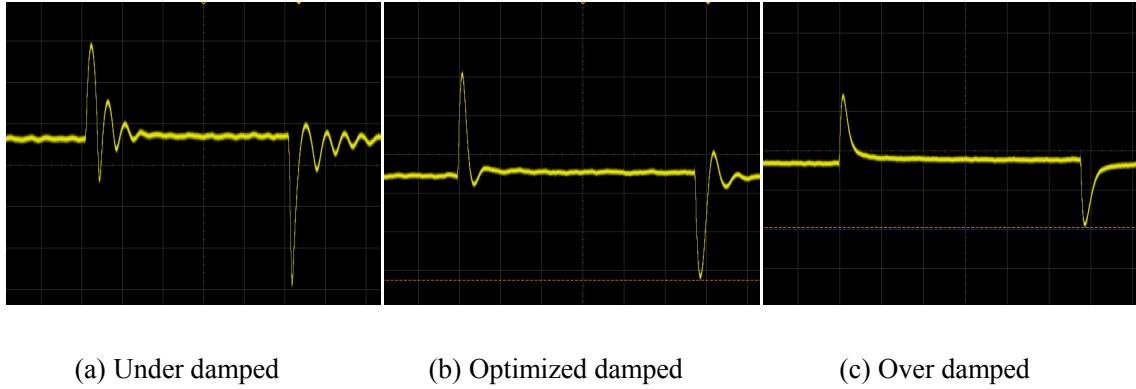(a) Under damped   (b) Optimized damped   (c) Over damped

Figure 6-2: Oscilloscope waveform of square wave test under different damping conditions.

The time constant of a bunch of hot wires with different geometrical designs was tested under different overheating ratios. All wires exhibited 300 nm thickness and 500 μm length with different wire widths of 3 μm, 5 μm and 10 μm, as shown in Figure 6-3a. According to the relation between the time constant of the square wave test and -3 dB cutoff frequency as expressed in Eq. (5-3), the cutoff frequency of these hot wires were calculated, as shown in Figure 6-3b. It shows that the cutoff frequency increases with Pt wire width reduction and overheating rising. It is consistent with the analysis of the factors that affect the time constant, as shown in Chapter 4: a smaller wire width has a more significant convection coefficient, and a larger overheating ratio creates a higher temperature difference between the hot wire and the ambient. They all can improve the frequency response of the hot wire.

(a) The measured time constant of square wave test.   (b) Estimated cutoff frequency of the fabricated hot wires.
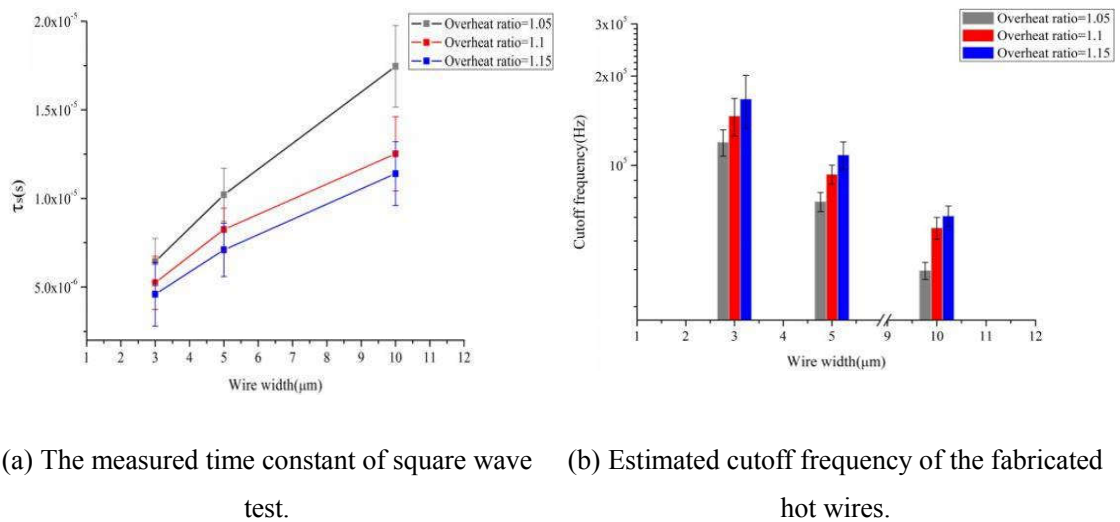
Figure 6-3: The cutoff frequency of hot wire with different dimensions and overheating ratios estimated by the square wave test.

The fastest response was obtained at a hot wire with a dimension of 300 nm × 3 μm × 500 μm at 1.15 overheating ratio. The time constant τ_s was found to be 3.54 μs, which corresponds to a cutoff frequency of 217 kHz. The waveform of the square wave test is illustrated in Figure 6-4.
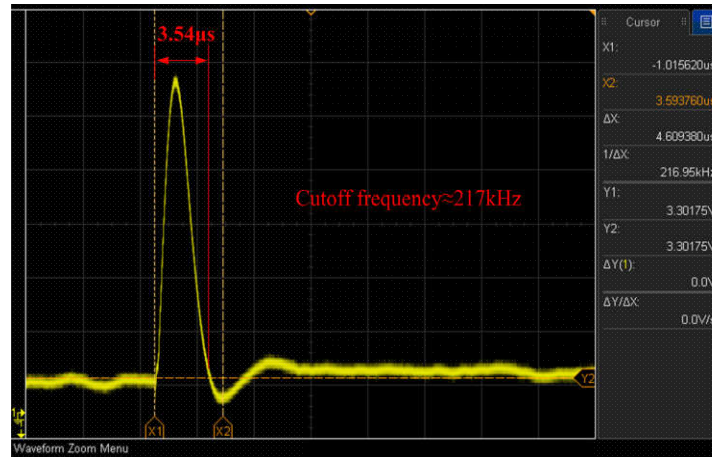

Figure 6-4: Response waveform of a hot wire with the smallest wire width of 3 μm.

6.3. Flow velocity response

The relation of the voltage output of the hot wire sensors and air velocity was calibrated in the wind tunnel. Here, the calibration is focused on eight micro-fabricated hot wires:(1) single hot wires, named hot wire 1—4; (2) double 45° hot wires, noted by hot wire 5—8. The air velocity at the inlet was varied from 0 to 40 m/s by adjusting the angular velocity of the fan at the wind tunnel outlet. These hot wires were operated in constant temperature mode. The output voltages of the circuit were acquired by an I/O card that contains a 16-bit digital A/D converter.

6.3.1. Single hot wire

Hot wires 1—4 have different wire lengths and prong thickness configurations, as illustrated in Figure 6-5. Their output voltage E is illustrated in.Figure 6-6a. As expected, the voltage E rises with increasing velocity. Figure 6-6b shows the curves $E^2 - E_0^2$ become almost straight under logarithmic coordinate, in which E_0^2 is the measured voltage at zero velocity. It implies that the micro-fabricated hot wires' output are almost perfectly consistent with King's law that the squared voltage is proportional to the fractional power of flow velocity. The measured voltages were fitted by the following expression:

$$E(V) = (A + BV^n)^{0.5},\qquad\qquad\qquad (6\text{-}4)$$

where *A*, *B*, and *n* are the parameters to be solved that have been introduced in Eq. (2-61).
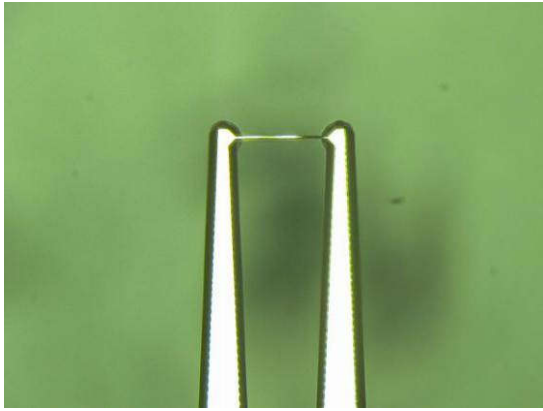
(a) Hot wire 1: wire length=250 μm, prong
thickness=52 μm.
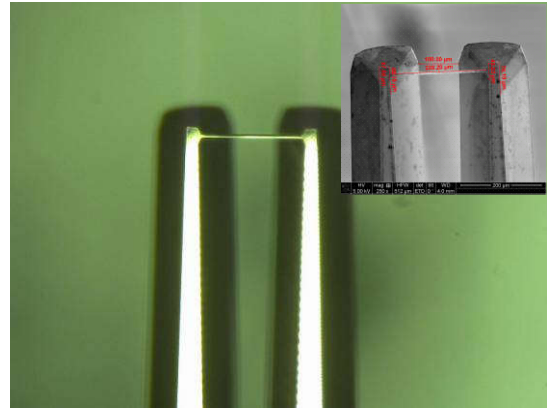
(b) Hot wire 2: wire length=250 μm, prong
thickness=115 μm.
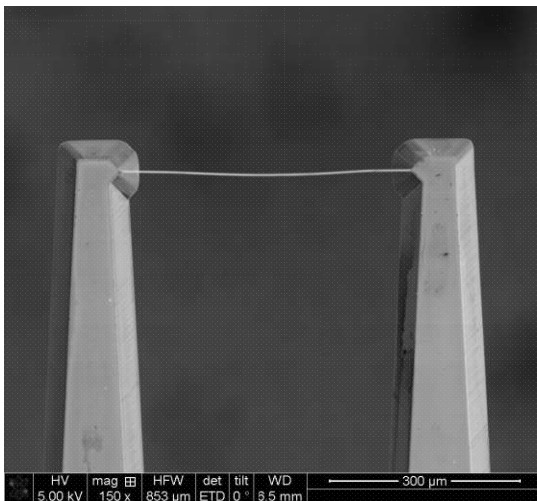
(c) Hot wire 3: wire length=500 μm, prong
thickness=44 μm.

(d) Hot wire 4: wire length=500 μm, prong
thickness=105 μm.

Figure 6-5: Single hot wire sensors used for calibration.

The curve fitting employed Levenberg-Marquardt algorithm [200]. The fitting result is listed in Table 6-1. It shows the power value *n* is slightly larger than 0.5, which has a small deviation from the typical value of *n*, 0.4-0.5. It is reported that *n* of conventional hot wires became larger than 0.5 at low velocities below 2 m/s, and the noise from natural convection at low velocities below 2 m/s is responsible for the error of fitting *n* [89][201]. For the

microfabricated hot wire under test, they undergo situations likewise. The measurement values of output voltages contain not only the contributions of forced convection but also natural convection's contributions. At low velocity, the latter contributions become dominant. It will increase n of King's law for curve fitting.
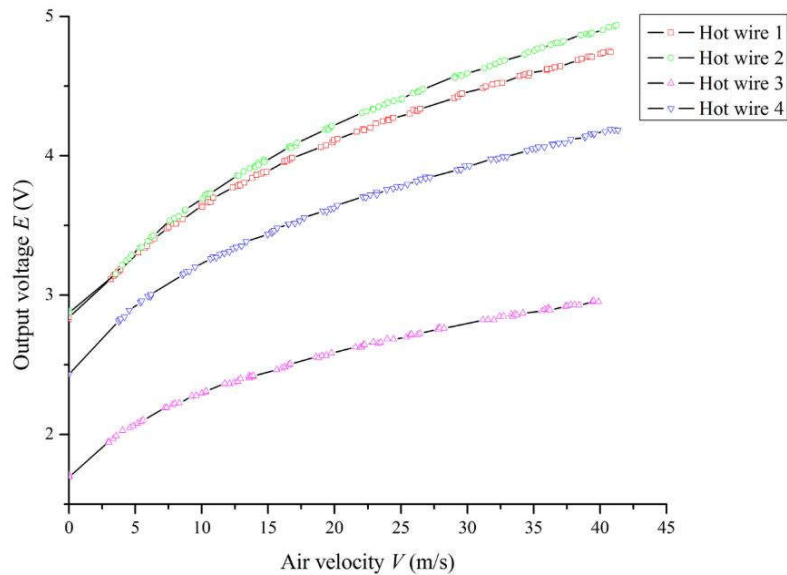
(a) Circuit output voltage at different velocities.
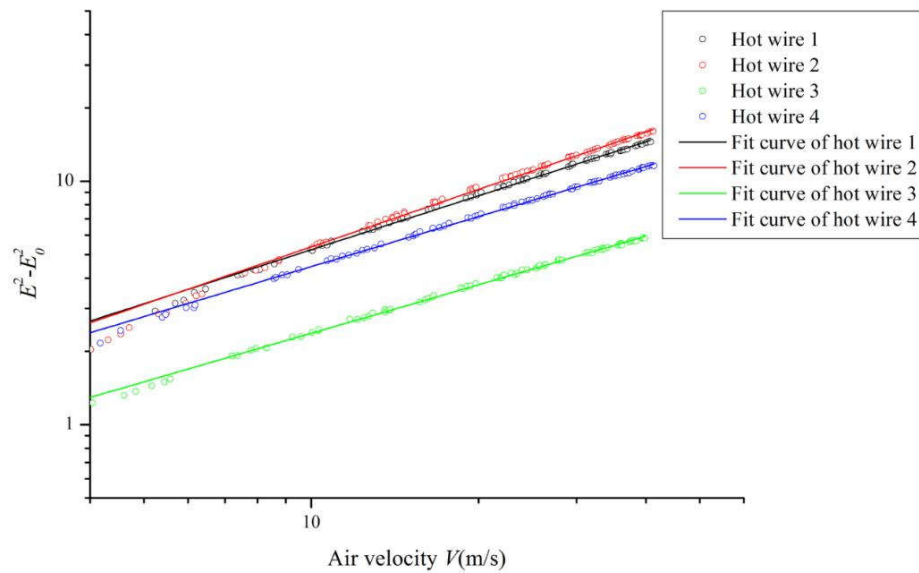
(b) The relation of E^2-E_0^2 as a function of air velocity.

Figure 6-6: Velocity responses of hot wires 1－4.

Table 6-1: Fitting results of King's law of hot wires $1-4$.

Hot wire No.	Fitting results of King's law
Hot wire 1	$E=(5.983+1.844V^{0.591})^{0.5}$
Hot wire 2	$E=(5.770+1.913V^{0.609})^{0.5}$
Hot wire 3	$E=(2.257+0.8178V^{0.561})^{0.5}$
Hot wire 4	$E=(4.698+1.477V^{0.580})^{0.5}$

6.3.2. Double 45º hot wires

The velocity responses of double 45º hot wires have also been tested. Their geometrical structures are shown in Figure 6-7.
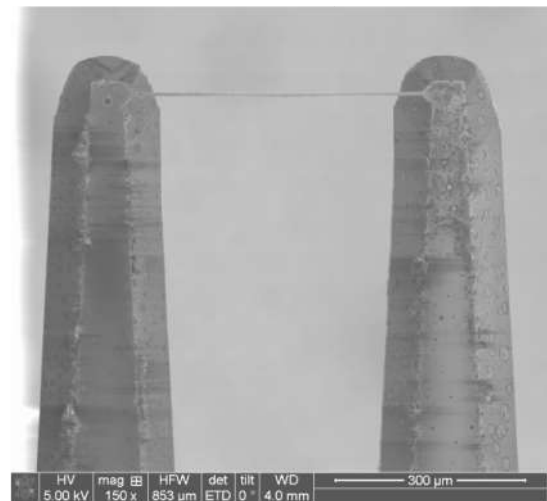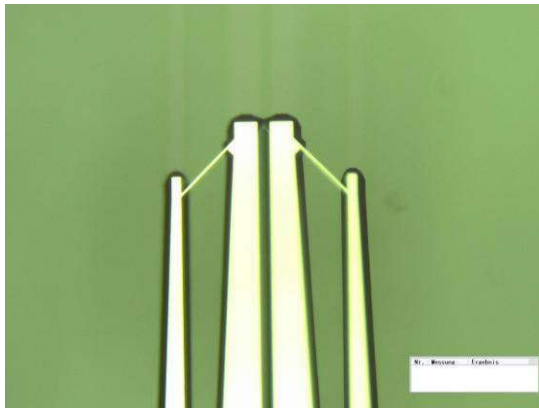

(a) Hot wire 5: wire length =150 μm, prong thickness=34 μm.
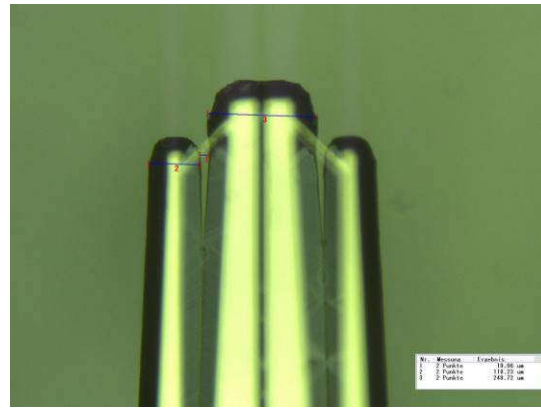
(b) Hot wire 6: wire length =150 μm, prong thickness=82 μm.
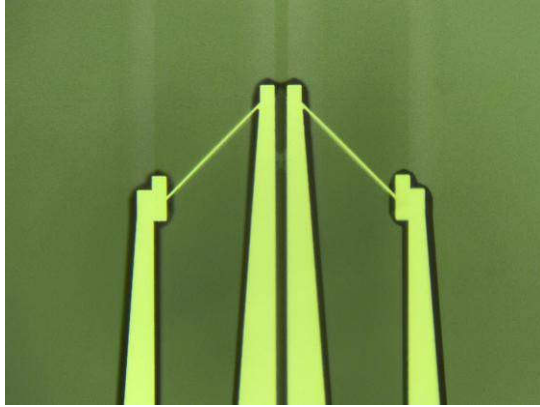
(c) Hot wire 7: wire length =300 μm, prong thickness=38 μm.
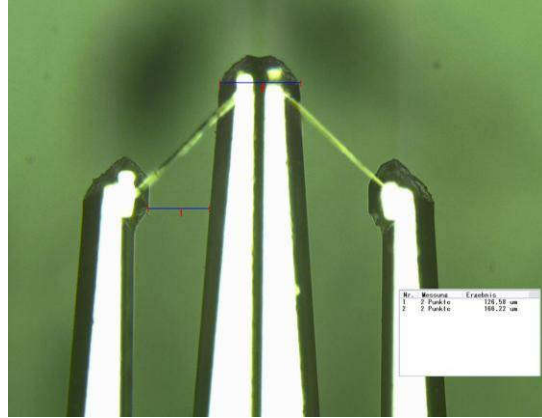
(d) Hot wire 8: wire length=300 μm, prong thickness=76 μm.

Figure 6-7: The double 45º hot wires under calibration.

The measured voltages at different air velocities are presented in Figure 6-8. The voltages were fitted using Eq. (6-4). The fitting results are listed in Table 6-2. It shows the power n is about 0.54-0.57. King's law works as well for double 45° hot wires.

Table 6-2: Fitting results of double 45° hot wires 5－8.

Hot wire No.		Fitting results of King's law
Hot wire 5	Left wire	$E=(8.052+1.829V^{0.570})^{0.5}$
	Right wire	$E=(7.629+1.719V^{0.573})^{0.5}$
Hot wire 6	Left wire	$E=(8.843+2.996V^{0.565})^{0.5}$
	Right wire	$E=(8.227+2.475V^{0.565})^{0.5}$
Hot wire 7	Left wire	$E=(4.993+1.148V^{0.543})^{0.5}$
	Right wire	$E=(4.684+0.888V^{0.543})^{0.5}$
Hot wire 8	Left wire	$E=(5.220+1.140V^{0.561})^{0.5}$
	Right wire	$E=(4.993+0.952V^{0.560})^{0.5}$
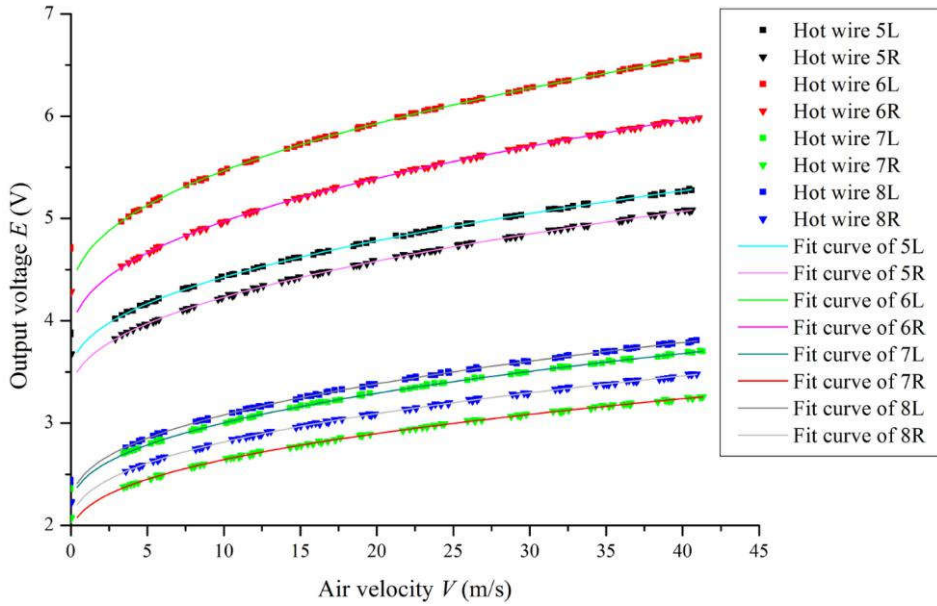
Figure 6-8: Velocity responses of the double 45º hot wires 5－8.

6.4. Direction response of single hot wire sensors

As introduced in Chapter 2, hot wires are also sensitive to the flow direction. Based on King's law and the definition of effective cooling velocity, a theoretical correlation between flow angle and voltage of hot wires for flow direction measurement is given by Eq. (3-3) and Eq. (3-4). h and k in the equations are the unknown parameters to be determined.

6.4.1. Yaw angle response

The yaw angle test is designed to calibrate factor k of the hot wires. The yaw responses of single hot wire 1－4 were tested in the wind tunnel. The static pressure difference at the wind tunnel inlet was set to 0.667 mbar, which corresponds to 10 m/s air velocity. These hot wires were attached to the rotary arm, and their substrate planes were set to 90° level. As the arm pitch was continually varied from -40º to 40º by a stepper motor, the hot wires' yaw angle φ relative to airflow direction varied from -40º to 40º as well. The output voltage $E(\varphi)$ of a constant temperature circuit was acquired. The measurement results of hot wires 1－4 are presented in Figure 6-9. It can be seen that the yaw response curves exhibit a cosine-like shape, and their maximum output occurs at $\varphi \approx 0°$. Applying Eq. (2-61) to the sampled voltage of hot wires, the curve expression to be fitted is of the form as follows:

$$E(\varphi) = (A + B(V(\cos^2\varphi + k\sin^2\varphi)^{0.5})^n)^{0.5} . \qquad (6\text{-}5)$$

The factor k is the only parameter to be determined. The fitting results of k are shown in Figure 6-9. The factor k of hot wire 1-4 are 0.27, 0.20, 0.16, and 0.12, respectively.
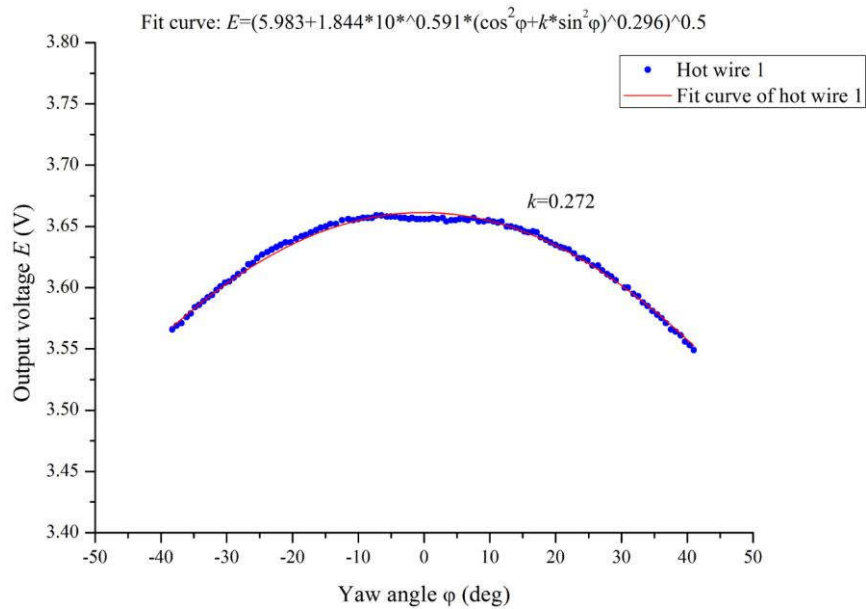
(a) Yaw response of hot wire 1.

(b) Yaw response of hot wire 2.

Fit curve: $E=(2.257+0.8178*10^{\wedge}0.561*(\cos^2\varphi+k*\sin^2\varphi)^{\wedge}0.285)^{\wedge}0.5$

$k=0.155$

(c) Yaw response of hot wire 3.

Fit curve: $E=(4.698+1.477*10^{\wedge}0.580*(\cos^2\varphi+k*\sin^2\varphi)^{\wedge}0.292)^{\wedge}0.5$

$k=0.119$
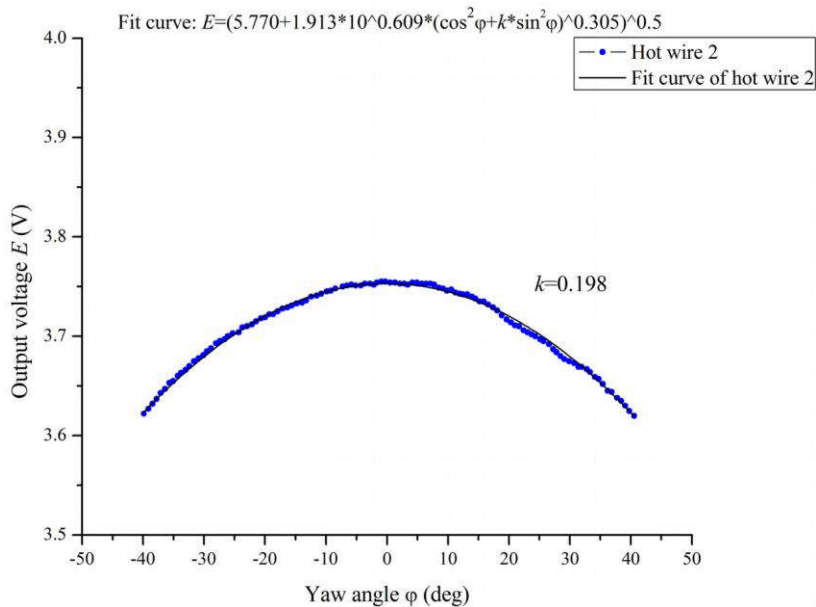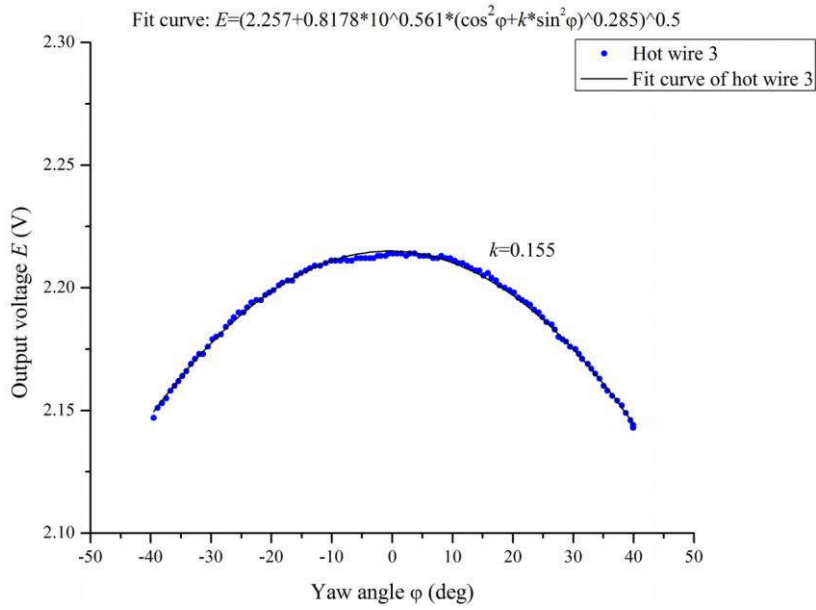
(d) Yaw response of hot wire 4.

Figure 6-9: Yaw responses of single hot wires.

It can be seen that the long hot wires 3 and 4 have a lower yaw factor than wires 1 and 2, and the thicker prongs hot wires 2 and 4 have the larger yaw factor than wires 1 and 4. The hot wire 4 has the smallest factor k, which means the velocity component in bi-normal direction of hot wire 4 has the least contribution to the output voltage in tangential direction;

in other words, the wire is relatively more sensitive to yaw changes. It implies that longer separation distance between prongs and thicker prongs may cause relatively less flow interference or convection along the tangential direction of the hot wire. In order to briefly illustrate their geometry's impact on yaw responses, the output voltages were normalized by dividing the output voltage at $\varphi=0°$, as shown in Figure 6-10.
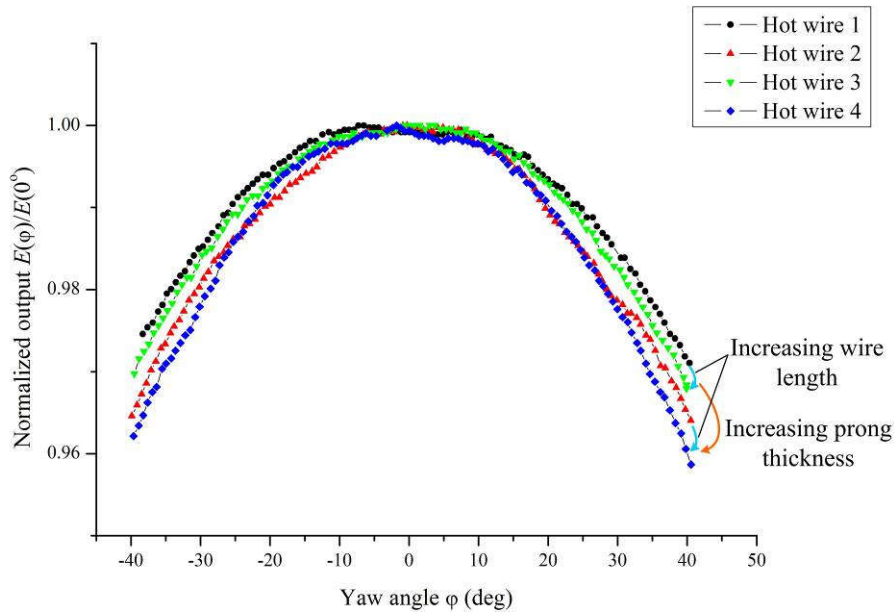
Figure 6-10: Normalized yaw responses of single hot wires.

6.4.2. Pitch response

Pitch response is another vital characteristic of the hot wire sensors. If the definition of effective cooling velocity is still valid, combing Eq. (2-47) and Eq. (2-61), the curve's expression to be fitted is expect to be of the form:

$$E(\phi) = (A + B(V(\cos^2\phi + h\sin^2\phi)^{0.5})^n)^{0.5}, \qquad (6\text{-}6)$$

where the pitch factor h can be obtained from the pitch response test. For convectional hot wires, $h > 1$, thus, their pitch response curves have cosine-like shapes.

The pitch angle of arm and velocity was set up in the same way as in the yaw response test. The sensors' substrate planes were switched to 0° level, and the pitch of arm is rotated from -40º to 40º. Figure 6-11 illustrates the pitch responses of hot wires 1－4. Figure 6-11a shows that a cosine-like response curve occurs in the hot wire 1 (250 μm wire length and 52 μm prong thickness), whereas the response curve of hot wire 4 (500 μm wire length and 44 μm prong thickness) is more like a sine curve with -27° phase shift, in Figure 6-11c. Hot wire 2

and 4 with thicker prong exhibited neither sine-like nor cosine-like curve shapes. Apparently, the definition, effective cooling velocity, cannot be directly applied to this occasion anymore. Furthermore, it indicates that prong geometry has some influence on the pitch response. The prongs effect will be further investigated in section 6.6.
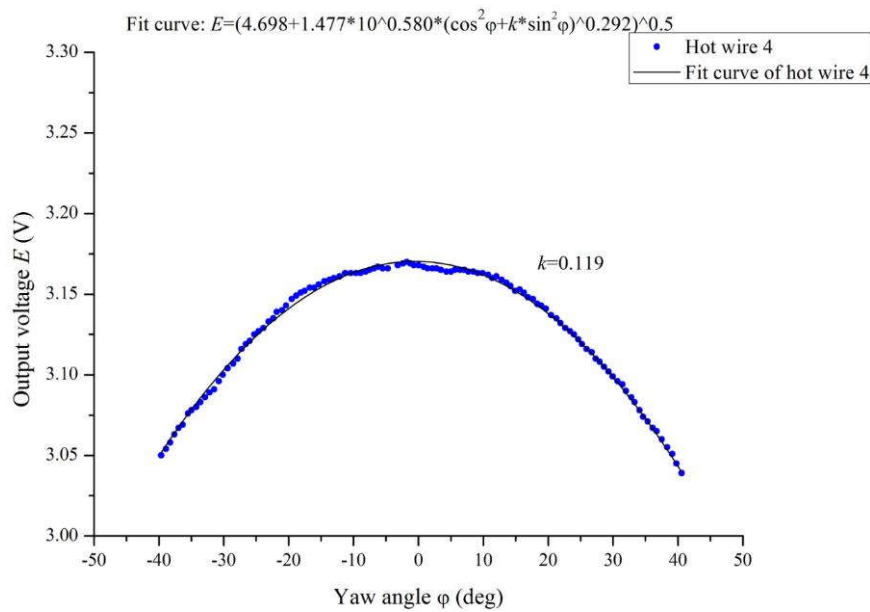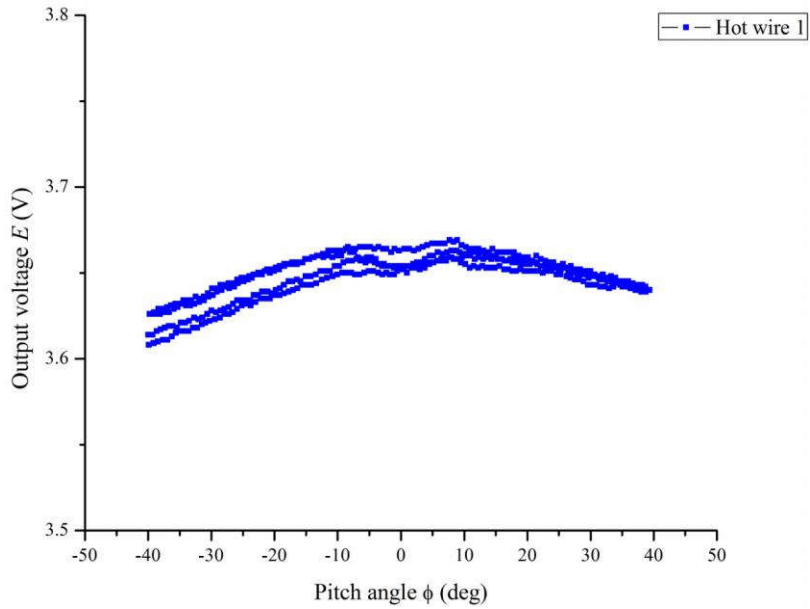

(a) Pitch response of hot wire 1.
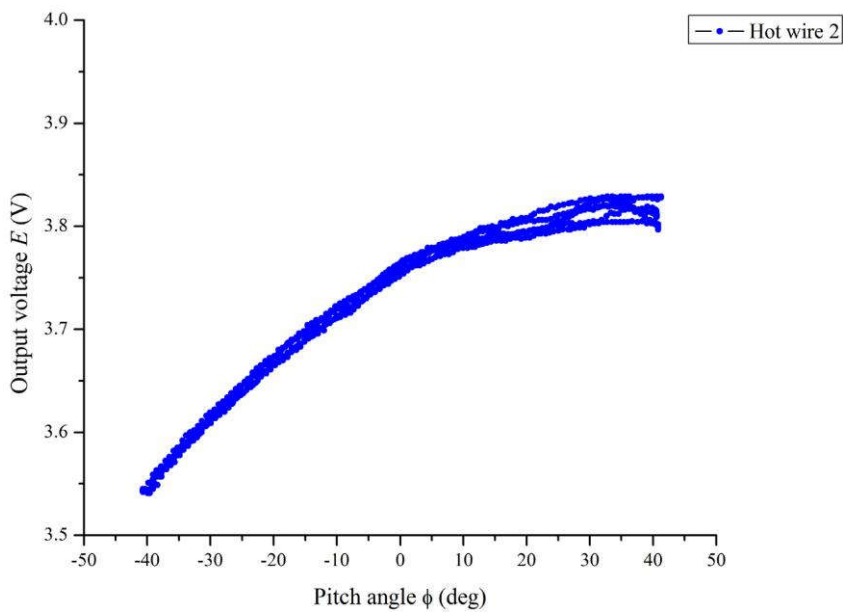
(b) Pitch response of hot wire 2.
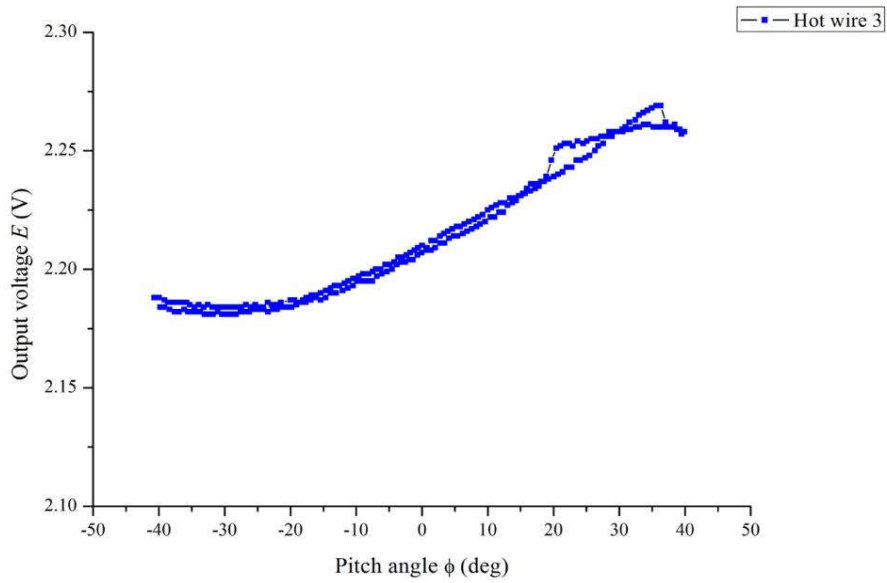
(c) Pitch response of hot wire 3.
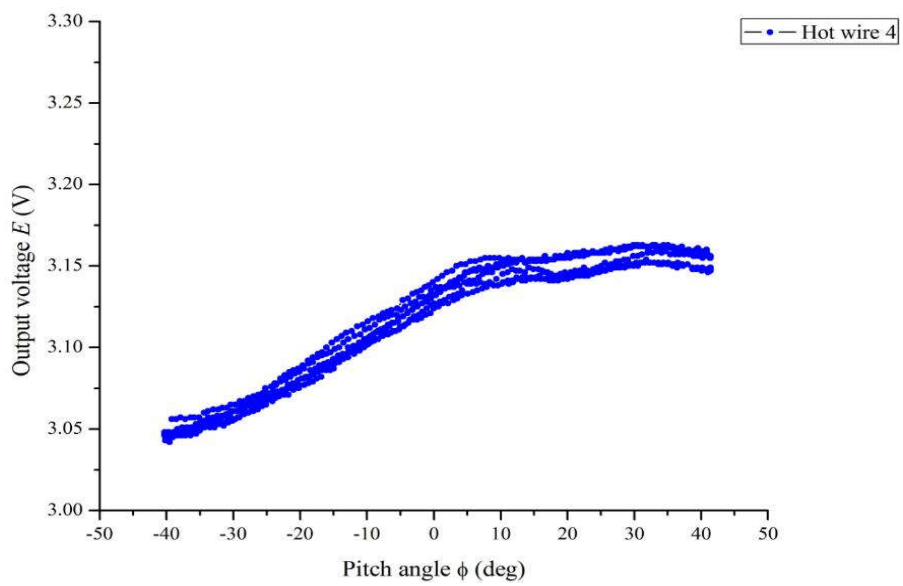
(d) Pitch response of hot wire 4.

Figure 6-11: Pitch responses of single hot wire sensors.

6. 5. Direction responses of double 45° hot wire sensors

6. 5. 1. Yaw response

Double 45° hot wires are used to measure flow direction, the calibration of the parameters k

is an essential step prior to flow direction measurement. Similar to single hot wire calibration, the substrates of double 45º hot wires 5-8 are subsequently attached to a rotating arm, and their substrate planes were set to the 90° position. The two-channel signals connected to the left and right hot wires were measured simultaneously. The results are presented in Figure 6-11. It shows that the output voltages of hot wires follow the yaw angle variation in a regular way. Applying Eq. (2-61) to these wires, their circuit voltages were derived, for left side wires:

$$E(\varphi) = (A + B[V\sqrt{\cos^2(45° + \varphi) + k\sin^2(45 + \varphi)}]^n)^{0.5}, \qquad (6\text{-}7)$$

and for right side wires:

$$E(\varphi) = (A + B[V\sqrt{\cos^2(45° - \varphi) + k\sin^2(45 - \varphi)}]^n)^{0.5}, \qquad (6\text{-}8)$$

where k is the only unknown parameter; parameters A, B, and n have been obtained through the previous velocity response test. Applying the obtained parameters to Eq. (6-7) and Eq. (6-8), the expressions used to fit the yaw response curve are deduced as listed in Table 6-3. The individual fitting results of hot wires 5－8 have been already shown in Figure 6-11. It shows that these two equations fit the measurement data very well, and the factor k is in the range of 0.04-0.13. For the wires on the left and right side of each double 45° hot wire chip, they possess nearly the same factor k. In occasions where tolerance requirements are not so tight, the calibration of only one side wire may be sufficient, which simplifies the process.
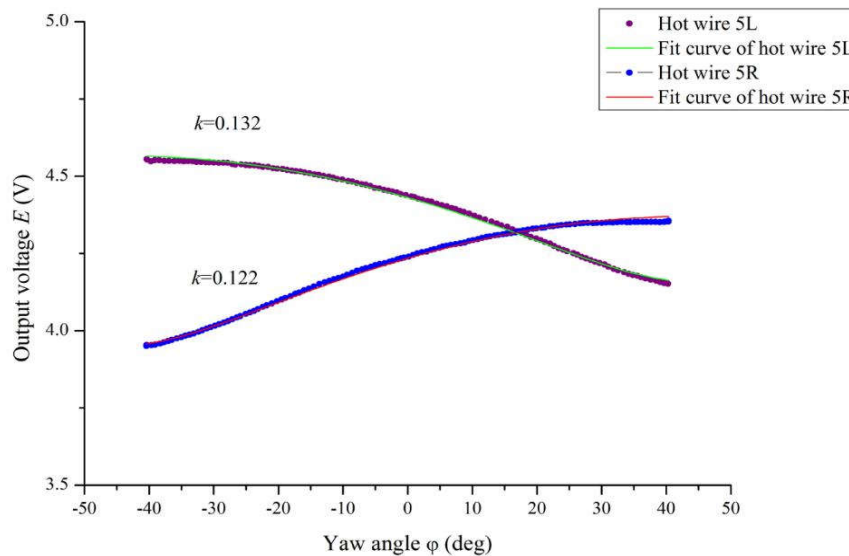
(a) Yaw response of hot wire 5.
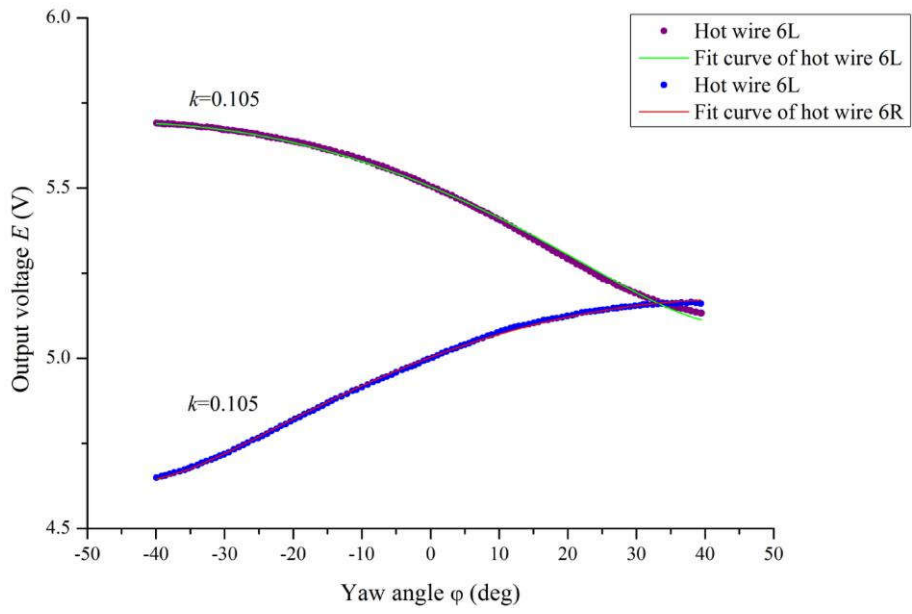
(b) Yaw response of hot wire 6.
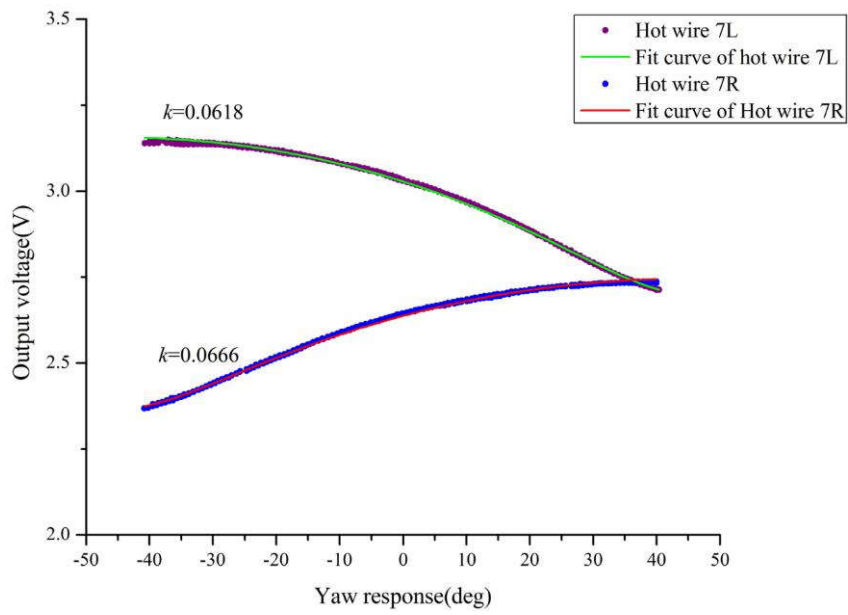
(c) Yaw response of hot wire 7.

(d) Yaw response of hot wire 8.

Figure 6-12: Yaw responses of double 45º hot wires.

Table 6-3: Fitting results of double 45° hot wires 5－8 for solving yaw factor.

| Hot wire No.		Fitting results of King's law
Hot wire 5	Left wire	$E=(8.052+1.829V^{0.570}(\cos^2\varphi+k\sin^2\varphi)^{0.286})^{0.5}$
	Right wire	$E=(7.629+1.719V^{0.573}(\cos^2\varphi+k\sin^2\varphi)^{0.287})^{0.5}$
Hot wire 6	Left wire	$E=(8.843+2.996V^{0.565}(\cos^2\varphi+k\sin^2\varphi)^{0.287})^{0.5}$
	Right wire	$E=(8.227+2.475V^{0.565}(\cos^2\varphi+k\sin^2\varphi)^{0.287})^{0.5}$
Hot wire 7	Left wire	$E=(4.993+1.148V^{0.543}(\cos^2\varphi+k\sin^2\varphi)^{0.276})^{0.5}$
	Right wire	$E=(4.684+0.888V^{0.543}(\cos^2\varphi+k\sin^2\varphi)^{0.277)0.5}$
Hot wire 8	Left wire	$E=(5.220+1.140V^{0.561}(\cos^2\varphi+k\sin^2\varphi)^{0.281})^{0.5}$
	Right wire	$E=(4.929+0.952V^{0.560}(\cos^2\varphi+k\sin^2\varphi)^{0.280})^{0.5}$

To illustrate the effect of different geometries, the yaw responses $E(\varphi)$ were normalized by

dividing through the maximum output voltage E_{max}, as shown in Figure 6-13. It shows both increasing wire length or prong thickness reduce the factor k. Hot wire 8 achieved the smallest factor k, which had the most considerable variation with respect to the yaw changing from 0° to 40°. The results also indicate that thicker prongs and longer wire lengths improve the yaw response sensitivity of hot wires. The background mechanism is similar to the single hot wire with respect to yaw response.
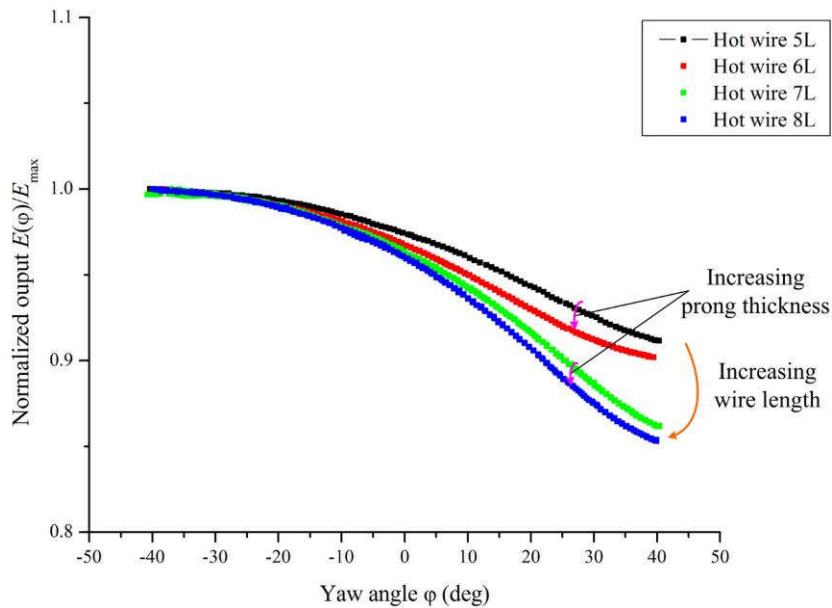
Figure 6-13: Normalized yaw responses of double 45° hot wires.

6.5.2. Pitch response

The pitch responses of hot wire 5-8 were tested with the same method as applied to single wire sensors. The results are illustrated in Figure 6-14. It shows that the voltage of double 45° hot wires varies with pitch angle with sine-like response curves. These curves have different phase shifts relative to 0°. Hot wire 7 and 8 have the same wire length of 300 μm, but different prong thicknesses; the phase shift increases with the prong thickness. For hot wires 5 and 6, the same effect can be seen. Hot wire 6 with the shortest wire and thickest prong, has the most massive phase shift of -35°. These pitch response curves are close to the ones of hot wire 3, except for a different phase shift. It may imply that the prong geometry also plays a role in flow convection.
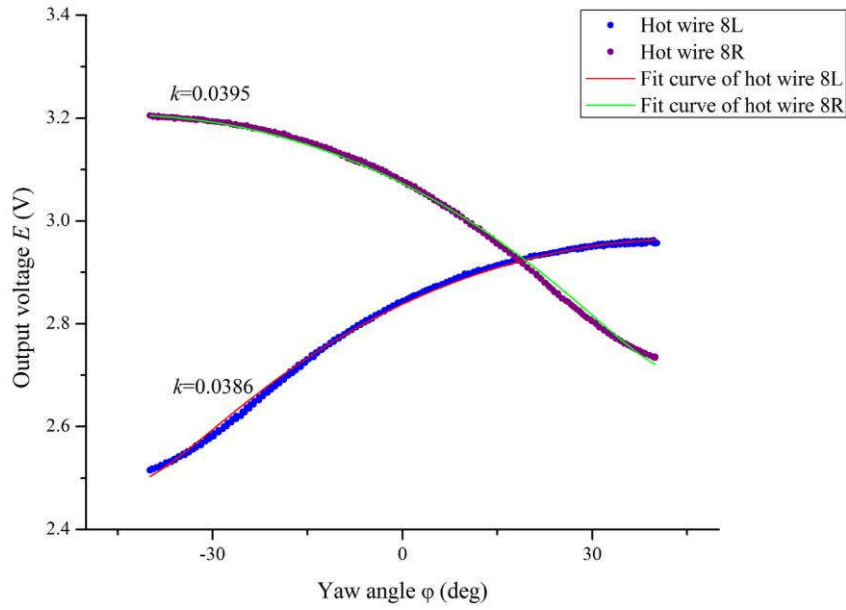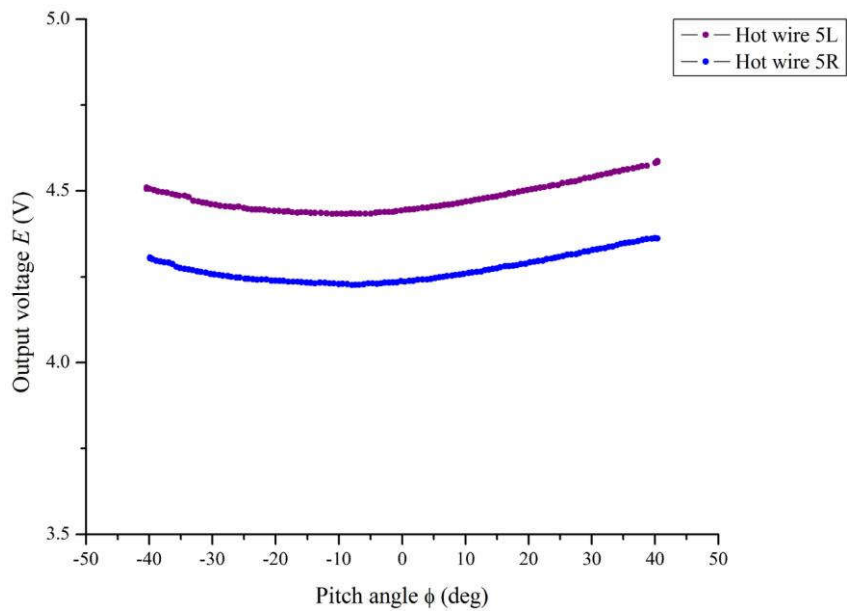
(a) Pitch response of hot wire 5.
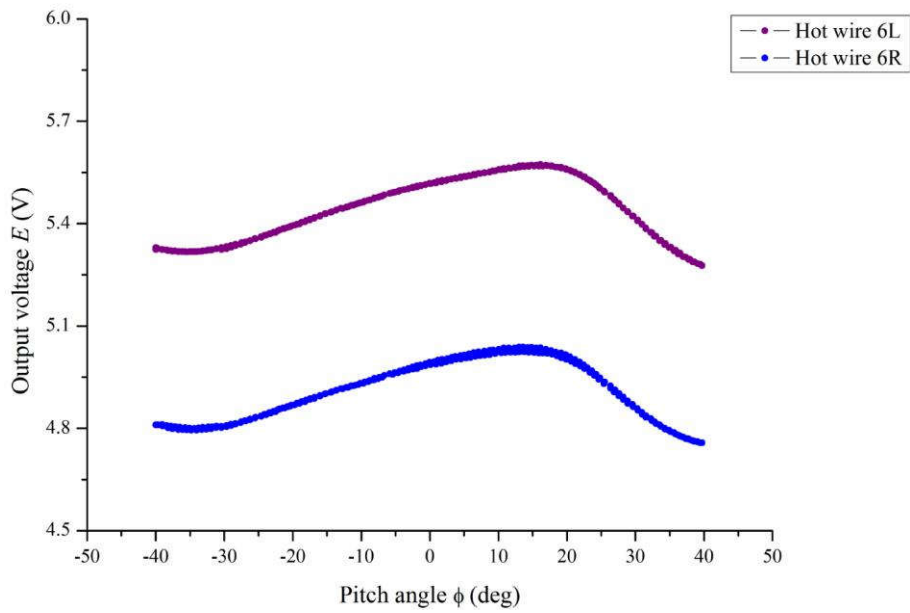
(b) Pitch response of hot wire 6.
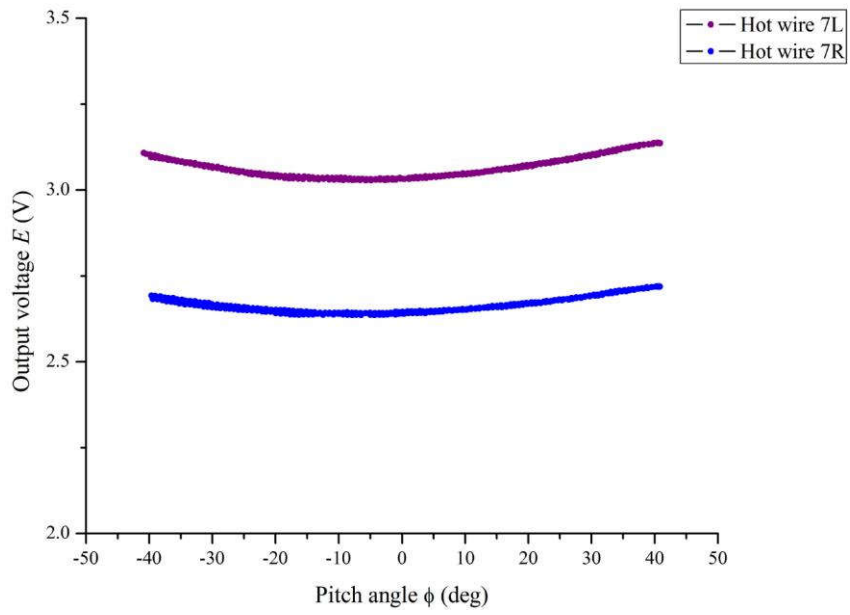
(c) Pitch response of hot wire 7.
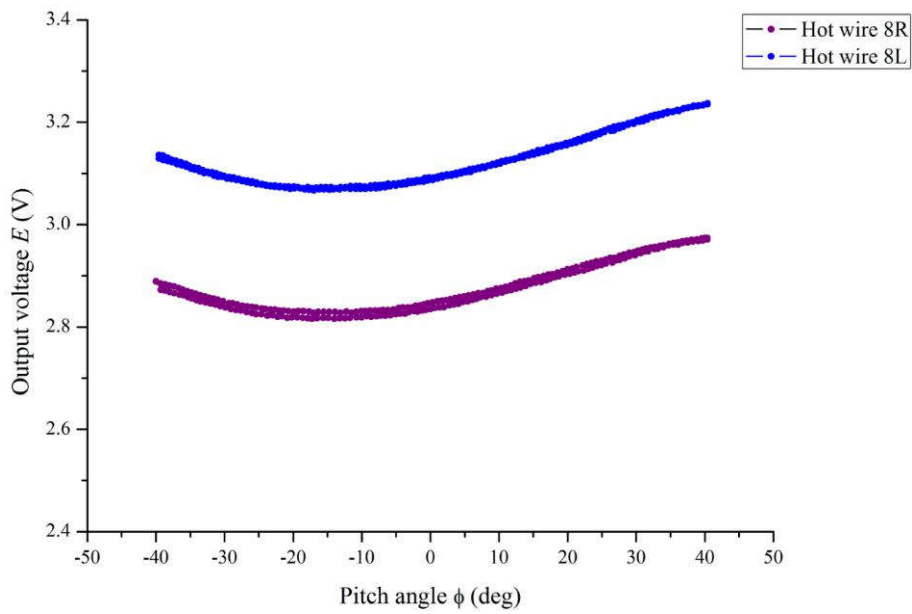
(d) Pitch response of hot wire 8.

Figure 6-14: The pitch responses of the double 45º hot wires.

6. 6. Prong geometry effect

In section 6.4.1, the pitch responses of single hot wires were given. Here, these results are re-illustrated with a normalizing treatment, where their voltages were divided by the maximum of the individual response curve, as shown in Figure 6-15. It is reported that the pitch factor h of conventional hot wires with a circular cross-section is higher than one, which causes a sine-like pitch response curve, implying that the minimum output voltage occurs at a pitch angle $\phi = 0°$. It means that under the sensor-based coordinate, the velocity component in the bi-normal direction of the hot wire has a more significant influence on the effective velocity than the component in the normal direction.
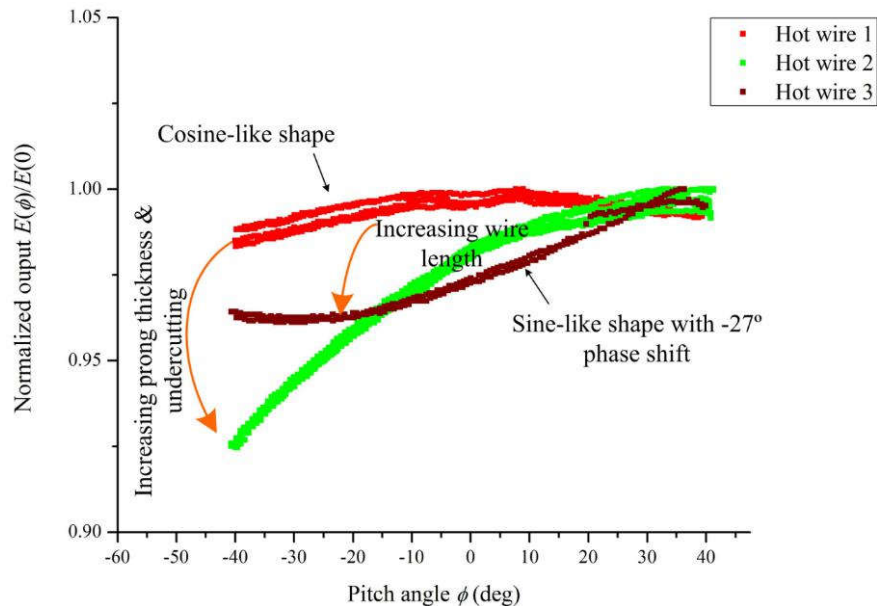
Figure 6-15: The normalized pitch responses of single hot wire sensors.

According to the simulation result shown in Figure 3-18, the shape of the hot wire cross-section also affects the heat convection. A rectangular hot wire without prongs possesses a cosine-like pitch response curve, which means that the factor h should be less than 1, and maximum output should occur at a pitch angle $\phi = 0°$. However, the curves of hot wires 2, 3, and 4 failed to support the simulation results. The disagreement between the simulation result and the actual sensors' response derives from the fact that the geometry model used in the simulation did not take the prong interference into account.

Furthermore, the yaw response curves exhibit distinct shapes under different prong geometries. It can be seen that when the wire length is increased from 250 μm for hot wire 1

to 500 μm for hot wire 3, their curves transform from cosine-like shape to sine-like one. Besides, when the prong thickness is increased from 52 μm for wire 1 to 115 μm for wire 2, the asymmetry of the curves becomes more pronounced. The difference of the curves' shape indicates once more that the prong geometry has given rise to the heat convection.
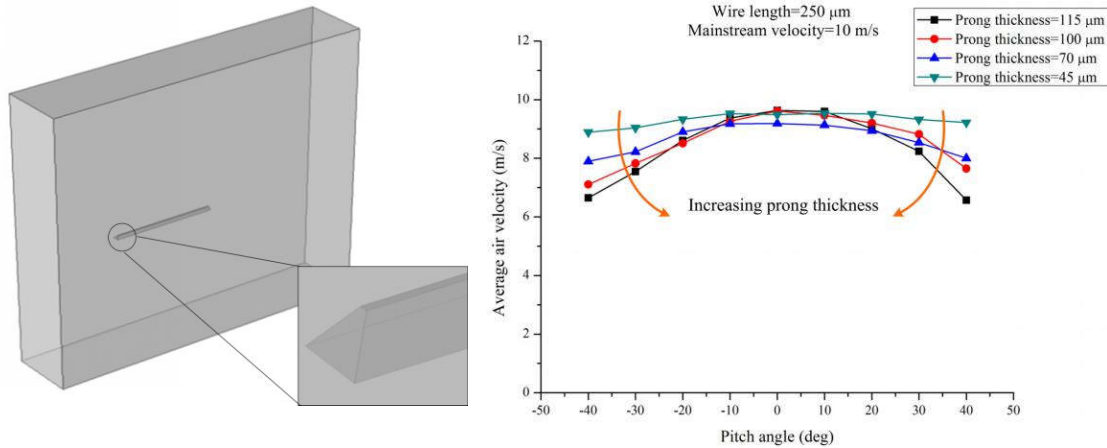
(a) Geometrical prong model of single hot wire for simulation.

(b) Simulation result of prong thickness effect on air velocity arriving at the hot wire.
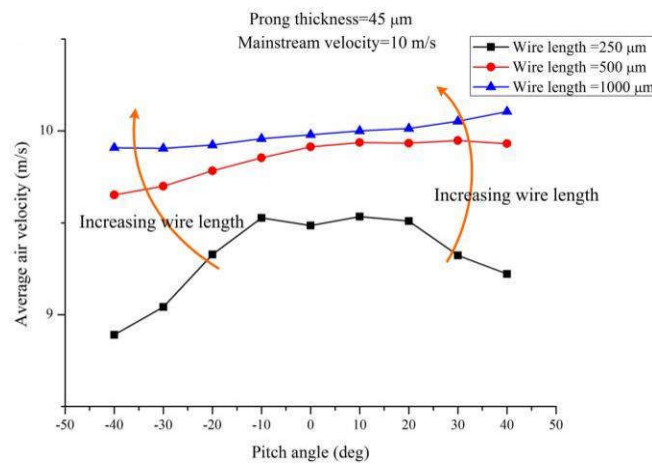
(c) Simulation result of wire length effect on air velocity arriving at the hot wire.

Figure 6-16: Prong thickness and length effect on air velocity arriving at the hot wire.

Many results presented previously suggest that the prong geometry plays an important role in the direction response of either single or double 45º hot wires. In order to investigate the prong shape's effect, the average velocity reaching the hot wire zone at different pitch angles was simulated by FEM. The simulations focused on the aerodynamic impact of the prong tip. The results are illustrated in Figure 6-16. Figure 6-16b shows the thicker prong

could give rise to a "Λ" shaped curve, and the curvature increases with prong thickness. On the other hand, longer wires can counteract the curvature, as shown in Figure 6-16c. With long hot wires of 1000 μm and thin prongs of 45 μm, the velocity-yaw curve transforms from "Λ" to "V". This can explain the observed change in the curves' shape of pitch response between hot wires 1 and 3, where hot wire 3 has a longer wire and thinner prong than hot wire 1.

The undercutting of the prongs is an inevitable problem during wet etching of the hot wires, which modifies the prong geometry. Thicker prongs need longer etching time, thus likely cause a larger undercutting at the prong tip. As a result, the air velocity arriving at hot wires is affected. Figure 6-17 presents the simulation results of the arriving air velocity for different undercutting lengths. It shows that a larger undercutting will exacerbate the asymmetry of the velocity curve. This may explain the shape difference of hot wire 1 and hot wire 2. Although they have the same wire length, hot wire 2 has thicker prongs, and a relatively larger undercutting occurs under the Pt layers, as shown in the SEM photo of hot wire 2 (Figure 6-5b). This may cause the more distinct asymmetrical shape of the velocity-pitch curve for hot wire 2.
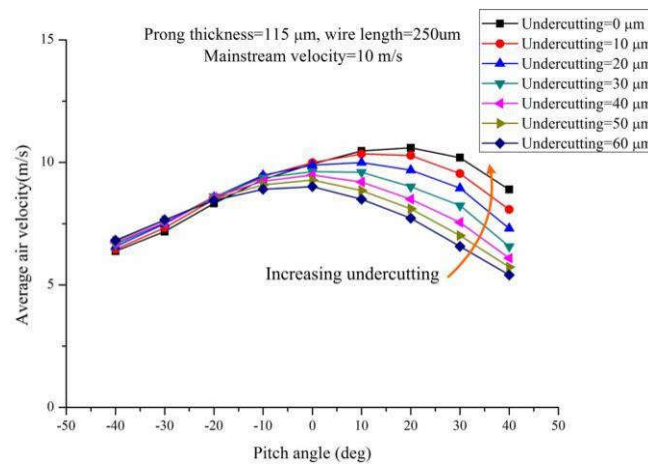
Figure 6-17: Prong undercutting effect on air velocity arriving at the hot wire.

Chapter 7 Conclusion and outlook

7.1. Conclusion

In this work, single and double 45º hot wire sensors have been designed, fabricated, and calibrated. Compared to conventional hot wire sensors, they show high spatial and temporal resolution. Thus, they provide researchers with attractive alternatives to measure small structures in turbulent flow regimes. The following findings are achieved:

Sensor design

Heat convection coefficients of microfabricated hot wires with rectangular cross-section were simulated at different flow velocities, including the application of slip boundary conditions. The results showed that the coefficient h and velocity V have a correlation of $h \propto V^n$, which is consistent with King's law. Simulation results for different geometrical parameters indicate that the reduction of wire width and wire thickness can decrease the time constant of hot wires considerably. Based on these findings, we designed two principal types of hot wire sensors with some subvariants. A single wire is intended for the common measurement of the velocity magnitude. Another one, in which two single wires with 45º inclination are arranged closely, is designed to measure both flow velocity magnitude and direction.

Sensor fabrication

Microfabrication has proven to be an effective way to reduce the overall geometrical size. The critical sizes of produced Pt wires are reduced to 150 μm (length) × 3 μm (width) × 0.3 μm (thickness). However, in the first fabricated device, substantial prong undercutting occurred. SEM photos of prongs indicate that the failure is closely related to the underetching of Si at convex corners and WTi mask overetching. Triton X-100 added to TMAH etching solution proved to alleviate the undercutting of Si prongs. Through optimized process conditions, an undercutting ratio of less than 0.5 has been achieved at 25% TMAH concentration, 95ºC etching temperature. On the other hand, it was found that a runaway reaction of Pt in H_2O_2 was the root cause of WTi overetching. Pt can catalyze the decomposition of H_2O_2. This accelerates rapidly due to reaction heat accumulation under insufficient cooling. As a result of heat accumulation, WTi etching rate is dramatically

increased. When lowering H_2O_2 concentration, then the trigger condition for the runaway reaction can be avoided.

Circuit design and analysis

The fabricated hot wires were operated at a constant temperature mode. Their driving circuits probably undergo unstable oscillation under the improper configuration of circuit parameters. Root locus of the transfer function of a simplified driving circuit was used to analyze the factors to affect their stability, and the rules concluded from the previous analysis were extrapolated to the actually designed circuits. It was subsequently verified by circuit simulation in which the Spice model of a hot wire was created. The verification result shows: offset voltage, GBP, and overheating ratio have a considerable effect on instability of constant temperature circuit, and a stable circuit with fast response can only be reached under the appropriate configuration of circuit components' parameters.

Calibration

The dynamic performance of the fabricated hot wires was estimated by a square wave test. The results imply that the hot wire sensors possessing fast response of a cutoff frequency more than 200 kHz have been achieved under optimum conditions. The responses of 8 sets of hot wires were tested under different flow velocities and under different pitch and yaw angles of attack. Their velocity responses are consistent with King's law, and all constants to be calibrated were obtained by curve fitting. The yaw responses of both single and double 45º hot wires comply with a cosine-like variation. It was also found that their yaw factors were reduced when increasing the Pt wire length and the prong thickness. However, the hot wires' response to pitch angle variation exhibited a complicated variation. It was affected by prong thickness and Pt wire length.

7.2. Outlook

Despite the fact that microfabricated hot wire sensors have been developed and calibrated successfully, there remain a few unsolved topics that need to be investigated further:

1. The cutoff frequency of fabricated hot wires was obtained through a square wave test, rather than in a direct way. As mentioned in chapter 2, the end conduction effect towards the prongs will deteriorate frequency response of a hot wire working in constant temperature mode, which cannot be found out by a purely electronic square wave test. Therefore, a direct

estimation method is required to be established.

2. Although calibrations of those hot wires were accomplished, due to lack of measurement benchmark of turbulence, an actual measurement of turbulence using the fabricated hot wires has not been implemented yet. In the future, a measurement in turbulent surroundings needs to be supplemented.

3. In this work, only common elements of various hot wire probes have already obtained. In order to measure more meaningful information, 3D structures comprising of more wires with the specific spatial arrangement are required to be developed and tested.

Bibliography

[1] Nelkin, Mark. "Resource Letter TF-1: Turbulence in Fluids." *American Journal of Physics* 68, no. 4 (2000): 310–18.

[2] Tsinober, A. *An Informal Introduction to Turbulence*. Springer, Dordrecht, 2009.

[3] Tennekes, H., and J. L. Lumley. *A First Course in Turbulence*. The MIT press, 1972.

[4] Joseph, H Spurk, and A. Nuri. *Fluid Mechanics*. Springer Berlin, 2008.

[5] Grote, Karl-Heinrich, and Erik K Antonsson. *Springer Handbook of Mechanical Engineering*. Vol. 10. Springer Science & Business Media, 2009.

[6] Holmes, Philip, John L Lumley, Gahl Berkooz, and Clarence W Rowley. *Turbulence, Coherent Structures, Dynamical Systems and Symmetry*, Cambridge university press , 2012.

[7] Hussain, AKM Fazle. "Role of Coherent Structures in Turbulent Shear Flows." *Proceedings of the Indian Academy of Sciences Section C: Engineering Sciences 4*, no. 2 (1981): 129.

[8] Träumner, K, Th Damian, Ch Stawiarski, and A Wieser. "Turbulent Structures and Coherence in the Atmospheric Surface Layer." *Boundary-Layer Meteorology* 154, no. 1 (2015): 1–25.

[9] Harun, Zambri, and Eslam Reda Lotfy. "Generation, Evolution, and Characterization of Turbulence Coherent Structures." In *Turbulence and Related Phenomena*. IntechOpen, 2018.

[10] Romeos, A., G. Lemonis, T. Panidis, and D. D. Papailiou. "Multisensor Hot Wire Vorticity Probe Measurements of the Formation Field of Two Corotating Vortices." *Flow, Turbulence and Combustion* 83, no. 2 (2009): 153–83.

[11] Guan, Xinlei, Nan Jiang, Lu Cheng, and Hao Zhang. "TRPIV Measurement of Turbulent Coherent Structures in a Drag-Reducing Flow Bypolymers." *Theoretical and Applied Mechanics Letters* 3, no. 4 (2013): 042006.

[12] Cantwell, Brian J. "Organized Motion in Turbulent Flow." *Annual Review of Fluid Mechanics* 13, no. 1 (1981): 457–515.

[13] Robinson, Stephen K. "Coherent Motions in the Turbulent Boundary Layer." *Annual Review of Fluid Mechanics 23*, no. 1 (1991): 601–39.

[14] Panton, Ronald L. "Overview of the Self-Sustaining Mechanisms of Wall Turbulence." *Progress in Aerospace Sciences* 37, no. 4 (2001): 341–83.

[15] Pope, Stephen B. *Turbulent Flows*. IOP Publishing, 2001.

[16] Robinson, Stephen K. "A Review of Vortex Structures and Associated Coherent Motions in Turbulent Boundary Layers." In *Structure of Turbulence and Drag Reduction*, 23–50. Springer, 1990.

[17] Hamba, Fujihiro. "Inverse Energy Cascade and Vortical Structure in the near-Wall Region of Turbulent Channel Flow." *Physical Review Fluids* 4, no. 11 (2019): 114609.

[18] Biferale, Luca, Stefano Musacchio, and Federico Toschi. "Inverse Energy Cascade in Three-Dimensional Isotropic Turbulence." *Physical Review Letters* 108, no. 16 (2012): 164501.

[19] Tropea, Cameron, and Alexander L Yarin. *Springer Handbook of Experimental Fluid Mechanics*. Springer Science & Business Media, 2007.

[20] Adrian, Ronald J. "Particle-Imaging Techniques for Experimental Fluid Mechanics." *Annual Review of Fluid Mechanics* 23, no. 1 (1991): 261–304.

[21] Lourenco, LM, A Krothapalli, and CA Smith. "Particle Image Velocimetry." In *Advances in Fluid Mechanics Measurements*, 127–99. Springer, 1989.

[22] Raffel, Markus, Christian E Willert, Fulvio Scarano, Christian J Kähler, Steve T Wereley, and Jürgen Kompenhans. *Particle Image Velocimetry: A Practical Guide*. Springer, 2018.

[23] Albrecht, H-E, Nils Damaschke, Michael Borys, and Cameron Tropea. *Laser Doppler and Phase Doppler Measurement Techniques*. Springer Science & Business Media, 2013.

[24] Buchhave, P. George and Lumley JL "The Measurement of Turbulence with the Laser Doppler Anemometer." *Ann. Rev. Fluid Mech* 11 (1979): 443–50.

[25] Goldstein, Richard. *Fluid Mechanics Measurements*. Routledge, 2017.

[26] Bruun, HH, *Hot-Wire Anemometry: Principles and Signal Analysis*, Oxford University Press,1995.

[27] Comte-Bellot, G. "Hot-Wire Anemometry." Annual *Review of Fluid Mechanics* 8, no. 1 (1976): 209–31.

[28] Stainback, PC, and KA Nagabushana. "Review of Hot-Wire Anemometry Techniques and the Range of Their Applicability for Various Flows." in *Third International Symposium on Thermal Anemometry* (1993): 4.

[29] Samet, M, and S Einav. "A Hot-Wire Technique for Simultaneous Measurement of Instantaneous Velocities in 3D Flows." *Journal of Physics E: Scientific Instruments* 20, no. 6 (1987): 683.

[30] Schön, T, and UR Müller. "A New Hot-Wire Technique for Measuring the Instantaneous Velocity Vector in Highly Turbulent Flow." In *Advances in Turbulence* 2, 292–97. Springer, 1989.

[31] Usselman, Melvyn C. "The Platinum Notebooks of William Hyde Wollaston." *Platinum Metals Review* 22, no. 3 (1978): 100–106.

[32] Szymanski, R. "The Fabrication of Ultrafine Platinum Wire." *Platinum Metals Rev* 14 (1970): 54.

[33] Ligrani, PM, and P Bradshaw. "Subminiature Hot-Wire Sensors: Development and Use." *Journal of Physics E: Scientific Instruments* 20, no. 3 (1987): 323.

[34] Fan, Y, G Arwatz, TW Van Buren, DE Hoffman, and M Hultmark. "Nanoscale Sensing Devices for Turbulence Measurements." *Experiments in Fluids* 56, no. 7 (2015): 138.

[35] Bailey, S. C. C., G. J. Kunkel, M. Hultmark, M. Vallikivi, J. P. Hill, K. A. Meyer, C. Tsay, C. B. Arnold, and A. J. Smits. "Turbulence Measurements Using a Nanoscale Thermal Anemometry Probe." *Journal of Fluid Mechanics* 663, no. 1 (2010): 160–79.

[36] Bruun, HH, N Nabhani, AA Fardad, and Hussain H Al-Kayiem. "Velocity Component Measurements by X Hot-Wire Anemometry." *Measurement Science and Technology* 1, no. 12 (1990): 1314.

[37] Mathioudakis, K, and FAE Breugelmans. "Use of Triple Hot Wires to Measure Unsteady Flows with Large Direction Changes." *Journal of Physics E: Scientific Instruments* 18, no. 5 (1985): 414.

[38] Vukoslavčević, PV. "A Hot-Wire Probe Configuration and Data Reduction Method to Minimize Velocity Gradient Errors for Simultaneous Measurement of Three Velocity Components in Turbulent Flows." *Experiments in Fluids* 53, no. 2 (2012): 481–88.

[39] Vukoslavčević, PV, Petar V, and James M Wallace. "Using Direct Numerical Simulation to Analyze and Improve Hot-Wire Probe Sensor and Array Configurations for Simultaneous Measurement of the Velocity Vector and the Velocity Gradient Tensor." *Physics of Fluids* 25, no. 11 (2013): 110820.

[40] Wilcox, David C. *Turbulence Modelling for CFD,* DCW Industries, Inc, 1994.

[41] Fujita, H., and L. S. G. Kovasznay. "Measurement of Reynolds Stress by a Single Rotated Hot Wire Anemometer." *Review of Scientific Instruments* 39, no. 9 (1968): 1351–55.

[42] Sherif, SA, and RH Pletcher. "A Hot-Wire/film Probe Method for the Measurement of Turbulent Stresses and Heat Fluxes in Nonisothermal Highly Three-Dimensional Flows." *Experimental Thermal and Fluid Science* 4, no. 1 (1991): 127–34.

[43] Westphal R.V., P.M. Ligrani and F.R. Lemos, "Development of subminiature multi-sensor hot-wire probes" *NASA Technical Memorandum* 100052 (1988).

[44]Jørgensen, Finn E. *How to Measure Turbulence with Hot-Wire Anemometers: A Practical Guide.* Dantec dynamics, 2002.

[45] Karman, T von. "Mechanische Ähnlichkeit Und Turbulenz, Nach Ges." *Wiss. Gottingen. Math. Physik. Klasse*, 1930.

[46] Barenblatt, GI. "Scaling Laws for Fully Developed Turbulent Shear Flows. Part 1. Basic Hypotheses and Analysis." *Journal of Fluid Mechanics* 248 (1993): 513–20.

[47] Savill, AM, and JC Mumford. "Manipulation of Turbulent Boundary Layers by Outer-Layer Devices: Skin-Friction and Flow-Visualization Results." *Journal of Fluid Mechanics* 191 (1988): 389–418.

[48] Savill, AM. "Drag Reduction by Passive Devices—a Review of Some Recent Developments." In *Structure of Turbulence and Drag Reduction*, 429–65. Springer, 1990.

[49] Chew, YT, BC Khoo, CP Lim, and CJ Teo. "Dynamic Response of a Hot-Wire Anemometer. Part II: A Flush-Mounted Hot-Wire and Hot-Film Probes for Wall Shear Stress Measurements." *Measurement Science and Technology* 9, no. 5 (1998): 764.

[50] Y. Ikeya1, R. Örlü, K. Fukagata1 and P. H. Alfredsson. "Revisiting Hot-Wire Anemometry Close to Solid Walls." (2017). *ERCOFTAC Bulletin*.

[51] Khoo, BC, YT Chew, and GL Li. "Time-Resolved near-Wall Hot-Wire Measurements: Use of

Laminar Flow Wall Correction Curve and near-Wall Calibration Technique." *Measurement Science and Technology* 7, no. 4 (1996): 564.

[52] Löfdahl, L., V. Chernoray, S. Haasl, G. Stemme, and M. Sen. "Characteristics of a Hot-Wire Microsensor for Time-Dependent Wall Shear Stress Measurements." *Experiments in Fluids* 35, no. 3 (2003): 240–51.

[53] Hussain, AKM Fazle. "Coherent Structures—reality and Myth." *The Physics of Fluids* 26, no. 10 (1983): 2816–50.

[54] Wallace, JM. "Methods of Measuring Vorticity in Turbulent Flows." *Experiments in Fluids* 4, no. 2 (1986): 61–71.

[55] Wallace, J. M., and J. F. Foss. "The Measurement of Vorticity in Turbulent Flows." *Annual Review of Fluid Mechanics* 27, no. 1 (1995): 469–514.

[56] Ryabtsev, A, S Pouya, A Safaripour, M Koochesfahani, and M Dantus. "Fluid Flow Vorticity Measurement Using Laser Beams with Orbital Angular Momentum." *Optics Express* 24, no. 11 (2016): 11762–67.

[57] Koochesfahani, Manoochehr, and Marcos Dantus. *Direct Optical Measurement of Vorticity in Fluid Flow*, Technical Report, Air Force Office of Scientific Research, 2015.

[58] Kovasznay, LSG. "Hot-Wire Investigation of the Wake behind Cylinders at Low Reynolds Numbers." *Proceedings of the Royal Society of London. Series A. Mathematical and Physical Sciences* 198, no. 1053 (1949): 174–90.

[59] Zimmerman, S, C Morrill-Winter, and J Klewicki. "Design and Implementation of a Hot-Wire Probe for Simultaneous Velocity and Vorticity Vector Measurements in Boundary Layers." *Experiments in Fluids* 58, no. 10 (2017): 148.

[60] Vukoslavčević, PV.., and J. M. Wallace. "A 12-Sensor Hot-Wire Probe to Measure the Velocity and Vorticity Vectors in Turbulent Flow." *Measurement Science and Technology* 7 (1996): 1451.

[61] Vukoslavčević, PV., J-L Balint, and JM Wallace. "A Multi-Sensor Hot-Wire Probe to Measure Vorticity and Velocity in Turbulent Flows," *J. Fluids Eng.*, 1989.

[62] Vukoslavčević, PV., James M Wallace, and Jean-Louis Balint. "The Velocity and Vorticity Vector Fields of a Turbulent Boundary Layer. Part 1. Simultaneous Measurement by Hot-Wire Anemometry." *Journal of Fluid Mechanics* 228 (1991): 25–51.

[63] Vukoslavčević, PV., and Dragan V Petrovi'c. *Multiple Hot-Wire Probes: Measurements of Turbulent Velocity and Vorticity Vector Fields*. Crnogorska Akademija Nauka I, 2000.

[64] He, Boshu, Yongfa Diao, Jinyuan Xu, and Changhel Chen. "Vorticity Measurements Using a 6-Sensor Hot-Wire Probe in a Tangentially Fired Furnace." *Tsinghua Science and Technology* 8, no. 2 (2003): 215–23.

[65] Vukoslavčević, Petar V, and James M Wallace. "On the Accuracy of Measurement of Turbulent

Velocity Gradient Statistics with Hot-Wire Probes." *Thermal Science* 21, no. suppl. 3 (2017): 533–51.

[66] Hutchins, N., TB Nickels, I. Marusic, and MS Chong. "Hot-Wire Spatial Resolution Issues in Wall-Bounded Turbulence." *J. Fluid Mech* 635 (2009): 103–36.

[67] Örlü, Ramis, and P Henrik Alfredsson. "On Spatial Resolution Issues Related to Time-Averaged Quantities Using Hot-Wire Anemometry." *Experiments in Fluids* 49, no. 1 (2010): 101–10.

[68] Oerlue, R, N Hutchins, T Kurian, and A Talamelli. "Challenges in Hot Wire Measurements in Wall-Bounded Turbulent Flows." In *APS Division of Fluid Dynamics Meeting Abstracts*, 2009.

[69] Hutchins, N, JP Monty, M Hultmark, and AJ Smits. "A Direct Measure of the Frequency Response of Hot-Wire Anemometers: Temporal Resolution Issues in Wall-Bounded Turbulence." *Experiments in Fluids* 56, no. 1 (2015): 18.

[70] Wyngaard, JC. "Spatial Resolution of the Vorticity Meter and Other Hot-Wire Arrays." *Journal of Physics E: Scientific Instruments* 2, no. 11 (1969): 983.

[71] Antonia, RA, and J Mi. "Corrections for Velocity and Temperature Derivatives in Turbulent Flows." *Experiments in Fluids* 14, no. 3 (1993): 203–8.

[72] Antonia, RA, Y Zhu, and J Kim. "On the Measurement of Lateral Velocity Derivatives in Turbulent Flows." *Experiments in Fluids* 15, no. 1 (1993): 65–69.

[73] Zhu, Y., and RA Antonia. "The Spatial Resolution of Hot-Wire Arrays for the Measurement of Small-Scale Turbulence." *Measurement Science and Technology* 7 (1996): 1349.

[74] King, Louis Vessot. "XII. On the Convection of Heat from Small Cylinders in a Stream of Fluid: Determination of the Convection Constants of Small Platinum Wires with Applications to Hot-Wire Anemometry." In *Philosophical Transactions of the Royal Society of London. Series A, Containing Papers of a Mathematical or Physical Character*, The Royal Society London, 1914.

[75] Durst, F, A Melling, and JH Whitelaw. "Principles and Practice of Laser Doppler Anemometry." *NASA STI/Recon Technical Report A*, 1976.

[76] Jensen, KD. "Flow Measurements." *Journal of the Brazilian Society of Mechanical Sciences and Engineering* 26, no. 4 (2004): 400–419.

[77] Lavoie, P, G Avallone, F De Gregorio, GP Romano, and RA Antonia. "Spatial Resolution of PIV for the Measurement of Turbulence." *Experiments in Fluids* 43, no. 1 (2007): 39–51.

[78] Scarano, Fulvio, and Peter Moore. "An Advection-Based Model to Increase the Temporal Resolution of PIV Time Series." *Experiments in Fluids* 52, no. 4 (2012): 919–33.

[79] Kazi, Salim Newaz. *An Overview of Heat Transfer Phenomena*. BoD-Books on Demand, 2012.

[80] Collis, DC, and MJ Williams. "Two-Dimensional Convection from Heated Wires at Low Reynolds Numbers." *Journal of Fluid Mechanics* 6, no. 03 (1959): 357–84.

[81] Stengele, FR, and HJ Rath. "Influence of Free Convection on the Heat Transfer from Hot-Wire Probes." *Wärme-Und Stoffübertragung* 29, no. 5 (1994): 299–307.

[82] Freymuth, P. "Engineering Estimate of Heat Conduction Loss in Constant Temperature Thermal Sensors." *TSI Quart* 4 (1979): 3–6.

[83] Rapp, Bastian E. *Microfluidics: Modeling, Mechanics and Mathematics*. William Andrew, 2016.

[84] Rybiński, Witold, and Jaroslaw Mikielewicz. "Analytical Solutions of Heat Transfer for Laminar Flow in Rectangular Channels." *Archives of Thermodynamics* 35, no. 4 (2014): 29–42.

[85] Welty, James, Gregory L Rorrer, and David G Foster. *Fundamentals of Momentum, Heat, and Mass Transfer*. John Wiley & Sons, 2014.

[86] Bruun, HH. "A Note on Static and Dynamic Calibration of Constant-Temperature Hot-Wire Probes." *Journal of Fluid Mechanics* 76, no. 1 (1976): 145–56.

[87] Swaminathan, MK, R Bacic, GW Rankin, and K Sridhar. "Improved Calibration of Hot-Wire Anemometers." *Journal of Physics E: Scientific Instruments* 16, no. 4 (1983): 335.

[88] Bruun, HH, MA Khan, Hussain H Al-Kayiem, and AA Fardad. "Velocity Calibration Relationships for Hot-Wire Anemometry." *Journal of Physics E: Scientific Instruments* 21, no. 2 (1988): 225.

[89] Bruun, HH. "Interpretation of a Hot Wire Signal Using a Universal Calibration Law." *Journal of Physics E: Scientific Instruments* 4, no. 3 (1971): 225.

[90] Wu, S, and N Bose. "An Extended Power Law Model for the Calibration of Hot-Wire/hot-Film Constant Temperature Probes." International Journal of Heat and Mass Transfer 37, no. 3 (1994): 437–42.

[91] Jorgensen, FE. "Directional Sensitivity of Wire and Fiber Film." *DISA Information* 11 (1971): 31–37.

[92] Yoshino, F., R. Waka, and T. Hayashi. "Hot-Wire Direction-Error Response Equations in Two-Dimensional Flow." *Journal of Physics E: Scientific Instruments* 22 (1989): 480.

[93] Bruun, HH, Nadir Nabhani, HH Al-Kayiem, AA Fardad, MA Khan, and E Hogarth. "Calibration and Analysis of X Hot-Wire Probe Signals." Measurement Science and Technology 1, no. 8 (1990): 782.

[94] Jerome, Frederick Ernest. "An Experimental Study of Interference Effects between Closely Spaced Wires of an X-Type Hot-Wire Probe," 1971.

[95] Andreopoulos, J. "Heat Transfer Measurements in a Heated Jet-Pipe Flow Issuing into a Cold Cross Stream." *The Physics of Fluids* 26, no. 11 (1983): 3201–10.

[96] Wittmer, KS, WJ Devenport, and JS Zsoldos. "A Four-Sensor Hot-Wire Probe System for Three-Component Velocity Measurement." *Experiments in Fluids* 24, no. 5 (1998): 416–23.

[97] Balint, J-L, P Vukoslavčević, and JM Wallace. "A Study of the Vortical Structure of the Turbulent Boundary Layer." In *Advances in Turbulence*, 456–64. Springer, 1987.

[98] Andreopoulos, Yiannis, and Anant Honkan. "Experimental Techniques for Highly Resolved Measurements of Rotation, Strain and Dissipation-Rate Tensors in Turbulent Flows." *Measurement Science and Technology* 7, no. 10 (1996): 1462.

[99] Taylor, G. I. "The Spectrum of Turbulence." *Proceedings of the Royal Society of London. Series*

A-Mathematical and Physical Sciences 164, no. 919 (1938): 476–90.

[100] Frisch Uriel, and Andrei Nikolaevich Kolmogorov. *Turbulence: The Legacy of A.N. Kolmogorov*, Cambridge university press, 1995.

[101] Sreenivasan, Katepalli R, and RA Antonia. "The Phenomenology of Small-Scale Turbulence." *Annual Review of Fluid Mechanics* 29, no. 1 (1997): 435–72.

[102] Moin, P. "Revisiting Taylor's Hypothesis*." Journal of Fluid Mechanics* 640 (2009): 1–4.

[103] Bahraminasab, A, MD Niry, J Davoudi, M Reza Rahimi Tabar, AA Masoudi, and KR Sreenivasan. "Taylor's Frozen-Flow Hypothesis in Burgers Turbulence." *Physical Review E* 77, no. 6 (2008): 065302.

[104] Dahm, Werner JA, and Kenneth B Southerland. "Experimental Assessment of Taylor's Hypothesis and Its Applicability to Dissipation Estimates in Turbulent Flows." *Physics of Fluids* 9, no. 7 (1997): 2101–7.

[105] Weinberg, Bernard C, and Samuel Lederman. *CONSTANT CURRENT ANEMOMETER DIAGNOSTICS OF FLOW FIELDS*. Research rept.:AD0688432, 1969.

[106] Bestion, D, J Gaviglio, and JP Bonnet. "Comparison between Constant-Current and Constant-Temperature Hot-Wire Anemometers in High-Speed Flows." *Review of Scientific Instruments* 54, no. 11 (1983): 1513–24.[

[107] Minn, Khine Soe, Tomoya Houra, Masato Tagawa, and others. "An Adaptive Response Compensation Technique for the Constant-Current Hot-Wire Anemometer," *Open Journal of Fluid Dynamics*, Vol.3 No.2, 2013.

[108] Corrsin, S. "Turbulence: Experimental Methods." In *Handbuch Der Physik*, 3:524–90, 1963.

[109] Blackwelder, Ron F. *Hot-Wire and Hot-Film Anemometers*. Defense Technical Information Center, 1981.

[110] Freymuth, P. "Noise in Hot-Wire Anemometers." *Review of Scientific Instruments* 39, no. 4 (1968): 550–57.

[111] Kidron, Izhak. "The Signal-to-Noise Ratios of Constant-Current and Constant-Temperature Hot-Wire Anemometers." *IEEE Transactions on Instrumentation and Measurement* 16, no. 1 (1967): 68–73.

[112] Samie, M, N Hutchins, and I Marusic. "Revisiting End Conduction Effects in Constant Temperature Hot-Wire Anemometry." *Experiments in Fluids* 59, no. 9 (2018): 133.

[113] Li, JD, BJ McKeon, W. Jiang, JF Morrison, and AJ Smits. "The Response of Hot Wires in High Reynolds-Number Turbulent Pipe Flow." *Measurement Science and Technology* 15 (2004): 789.

[114] Li, JD. "Dynamic Response of Constant Temperature Hot-Wire System in Turbulence Velocity Measurements." *Measurement Science and Technology* 15, no. 9 (2004): 1835.

[115] Manshadi, Mojtaba Dehghan, and Mohammad Kazemi Esfeh. "Analytical and Experimental Investigation About Heat Transfer of Hot-Wire Anemometry." In An Overview of Heat Transfer

Phenomena, 67. INTECH, 2012.

[116] Hultmark, Marcus, Anand Ashok, and Alexander J Smits. "A New Criterion for End-Conduction Effects in Hot-Wire Anemometry." *Measurement Science and Technology* 22, no. 5 (2011): 055401.

[117] Zhang, Wen-Ming, Guang Meng, and Xueyong Wei. "A Review on Slip Models for Gas Microflows." *Microfluidics and Nanofluidics* 13, no. 6 (2012): 845–82.

[118] Guo, ZL, BC Shi, and Ch G Zheng. "An Extended Navier-Stokes Formulation for Gas Flows in the Knudsen Layer near a Wall." EPL (Europhysics Letters) 80, no. 2 (2007): 24001.

[119] Struchtrup, Henning. "Maxwell Boundary Condition and Velocity Dependent Accommodation Coefficient." *Physics of Fluids* 25, no. 11 (2013): 112001.

[120] Yang, Qin, Yulu Liu, Haijun Zhang, and Chuncheng Zuo. "Derivation of Generalized Maxwell Velocity Slip Model." In *AIP Conference Proceedings*, 1628:382–87, 2014.

[121] Lockerby, Duncan A, Jason M Reese, and Michael A Gallis. "The Usefulness of Higher-Order Constitutive Relations for Describing the Knudsen Layer." Physics of Fluids 17, no. 10 (2005): 100609.

[122] McDonald, Donald, and Leslie B Hunt. *A History of Platinum and Its Allied Metals*. Johnson Matthey Plc, 1982.

[123] Sacharoff, AC, RM Westervelt, and J Bevk. "Fabrication of Ultrathin Drawn Pt Wires by an Extension of the Wollaston Process." *Review of Scientific Instruments* 56, no. 7 (1985): 1344–46.

[124] Bennett, Herbert E. "The Manipulation of Wollaston Wire." *Journal of Scientific Instruments* 19, no. 11 (1942): 168.

[125] Bomelburg, Herbert J. "Handling of Extremely Thin Wollaston Wires." *Review of Scientific Instruments* 30, no. 12 (1959): 1114–15.

[126] Ligrani, PM, and P Bradshaw. "Spatial Resolution and Measurement of Turbulence in the Viscous Sublayer Using Subminiature Hot-Wire Probes." *Experiments in Fluids* 5, no. 6 (1987): 407–17.

[127] Young, Darrin J, Christian A Zorman, and Mehran Mehregany. *MEMS/NEMS Devices and Applications*. Springer, Heidelberg, 2004, P. 225, 2004.

[128] Kovačević, Goran, and Branko Pivac. "Reactions in Silicon-Nitrogen Plasma." *Physical Chemistry* 19, no. 5 (2017): 3826–36.

[129] Kelly, John J, and Harold GG Philipsen. "Anisotropy in the Wet-Etching of Semiconductors." *Solid State and Materials Science* 9, no. 1–2 (2005): 84–90.

[130] Köllensperger, PA, WJ Karl, MM Ahmad, WT Pike, and M Green. "Patterning of Platinum (Pt) Thin Films by Chemical Wet Etching in Aqua Regia." *Journal of Micromechanics and Microengineering* 22, no. 6 (2012): 067001.

[131] Meier, Sebastian and Rinck, Helmut, *Patterning platinum by alloying and etching platinum alloy*, US patent 20200035500A1, 2019

[132] Zaborowski, M, P Grabiec, and A Barcz. "Manufacturing of Pt-Electrode by Wet Etching."

Microelectronic Engineering 82, no. 3–4 (2005): 283–88.

[133] Wuu, Dong-Sing, Nai-Hao Kuo, Fang-Ching Liao, Ray-Hua Horng, and Ming-Kwei Lee. "Etching of Platinum Thin Films in an Inductively Coupled Plasma." *Applied Surface Science* 169 (2001): 638–43.

[134] Ramesh, Ramamoorthy. *Thin Film Ferroelectric Materials and Devices*. Vol. 3. Springer Science & Business Media, 2013.

[135] Gosset, Nicolas, Mohamed Boufnichel, Emilie Bahette, Walid Khalfaoui, Rami Ljazouli, Virginie Grimal-Perrigouas, and Remi Dussart. "Single and Multilayered Materials Processing by Argon Ion Beam Etching: Study of Ion Angle Incidence and Defect Formation." *Journal of Micromechanics and Microengineering* 25, no. 9 (2015): 095011.

[136] Faizan, Muhammad. Design and Fabrication of Multilayer Piezoelectric NEMS Resonators, 2016.

[137] Tong, HD, RAF Zwijze, JW Berenschot, RJ Wiegerink, GJM Krijnen, and MC Elwenspoek. "Characterization of Platinum Lift-off Technique," *The Journal of Physical Chemistry*, 2000.

[138] Fu, Yifeng, Li-Lei Ye, and Johan Liu. "Thick Film Patterning by Lift-off Process Using Double-Coated Single Photoresists." *Materials Letters* 76 (2012): 117–19.

[139] Shibata, H, H Iwasaki, T Oku, and Y Tarui. "A Novel Liftoff Process for VLSI Using Plasma Deposition and Etching." In *1979 International Electron Devices Meeting*, 691–691, 1979.

[140] Sarkar, Jaydeep. Sputtering Materials for VLSI and Thin Film Devices. William Andrew, 2010.

[141] Cormier, P-A, A Balhamri, A-L Thomann, Remi Dussart, Nadjib Semmar, Jacky Mathias, R Snyders, and Stephanos Konstantinidis. "Measuring the Energy Flux at the Substrate Position during Magnetron Sputter Deposition Processes." *Journal of Applied Physics* 113, no. 1 (2013): 013305.

[142] Linder, C, L Paratte, M-A Grétillat, VP Jaecklin, and NF De Rooij. "Surface Micromachining." *Journal of Micromechanics and Microengineering* 2, no. 3 (1992): 122.

[143] Maboudian, Roya. "Surface Processes in MEMS Technology." *Surface Science Reports* 30, no. 6 (1998): 207.

[144] Van den Meerakker, JEAM, M Scholten, and JJ van Oekel. "The Etching of Ti-W in Concetrated H2O2 Solutions." *Thin Solid Films* 208, no. 2 (1992): 237–42.

[145] Nagalingam, Samuel, Suketu Parikh, Steve Sharpe, Larry Anderson, and Ron Ross. "Improvement in Wet Etch of TiW Fusible Links in AlCu/TiW/PtSi Metallization for 0.8 μm BICMOS." In *MRS Proceedings*, 427:407, 1996.

[146] Stein, David J, Dale Hetherington, Terry Guilinger, and Joseph L Cecchi. "In Situ Electrochemical Investigation of Tungsten Electrochemical Behavior during Chemical Mechanical Polishing." *Journal of The Electrochemical Society* 145, no. 9 (1998): 3190–96.

[147] Van den Meerakker, JEAM, JP Metsemakers, and JB Giesbers. "The Etching of Ti Adhesion Layers in H2O2 Solutions." *Journal of The Electrochemical Society* 149, no. 5 (2002): C256–C260.

[148] Hanson, Karrie Jo, Barbara J Sapjeta, and Ken M Takahashi. *Process for Etching Titanium at a*

Controllable Rate, US Patent 5,376,236, 1994.

[149] Gosálvez, MA, K Sato, AS Foster, RM Nieminen, and H Tanaka. "An Atomistic Introduction to Anisotropic Etching." *Journal of Micromechanics and Microengineering* 17, no. 4 (2007): S1.

[150] Sato, Kazuo, Mitsuhiro Shikida, Yoshihiro Matsushima, Takashi Yamashiro, Kazuo Asaumi, Yasuroh Iriye, and Masaharu Yamamoto. "Characterization of Orientation-Dependent Etching Properties of Single-Crystal Silicon: Effects of KOH Concentration." *Sensors and Actuators A*: Physical 64, no. 1 (1998): 87–93.

[151] Resnik, Drago, Danilo Vrtacnik, and Slavko Amon. "Morphological Study of {311} Crystal Planes Anisotropically Etched in (100) Silicon: Role of Etchants and Etching Parameters." *Journal of Micromechanics and Microengineering* 10, no. 3 (2000): 430.

[152] Thornton, John A. "Influence of Apparatus Geometry and Deposition Conditions on the Structure and Topography of Thick Sputtered Coatings." *Journal of Vacuum Science and Technology* 11, no. 4 (1974): 666–70.

[153] Huang, Shusen, and Xin Zhang. "Extension of the Stoney Formula for Film-Substrate Systems with Gradient Stress for MEMS Applications." *Journal of Micromechanics and Microengineering* 16, no. 2 (2006): 382.

[154] Mayadas, AF, and M Shatzkes. "Electrical-Resistivity Model for Polycrystalline Films: The Case of Arbitrary Reflection at External Surfaces." *Physical Review B* 1, no. 4 (1970): 1382.

[155] Sondheimer, EH. "A Note on the Theory of Conduction in Metals." *Proceedings of the Physical Society*. Section A 65, no. 7 (1952): 561.

[156] Namba, Yoshikatsu. "Resistivity and Temperature Coefficient of Thin Metal Films with Rough Surface." *Japanese Journal of Applied Physics* 9, no. 11 (1970): 1326.

[157] Datskos, PG, NV Lavrik, and S Rajic. "Performance of Uncooled Microcantilever Thermal Detectors." *Review of Scientific Instruments* 75, no. 4 (2004): 1134–48.

[158] Zhigal'skii, GP, and Brian K Jones. *The Physical Properties of Thin Metal Films*. Vol. 13. CRC Press, 2003.

[159] Agustsson, JS, UB Arnalds, AS Ingason, Kristinn B Gylfason, K Johnsen, S Olafsson, and Jon Tomas Gudmundsson. "Electrical Resistivity and Morphology of Ultra Thin Pt Films Grown by Dc Magnetron Sputtering on SiO2." In *Journal of Physics: Conference Series*, 100:082006, 2008.

[160] Mola, EE, and JM Heras. "Exact and Approximate Equations for the Thickness Dependence of Resistivity and Its Temperature Coefficient in Thin Polycrystalline Metal Films." *Thin Solid Films* 18, no. 1 (1973): 137–44.

[161] Schnelle, W, and U Dillner. "Thickness Dependence of Resistivity and Its Temperature Coefficient of Polycrystalline Bismuth Films*." Physica Status Solidi* (a) 44, no. 1 (1977): 197–204.

[162] Zhai, Yujia, Changlong Cai, Jing Huang, Huan Liu, Shun Zhou, and Weiguo Liu. "Study on the

Resistance Characteristic of Pt Thin Film." *Physics Procedia* 32 (2012): 772–78.

[163] Yamashita, Masato, Shoji Yamaguchi, and Hideo Enjoji. "Resistivity Correction Factor for the Four-Probe Method: Experiment I." *Japanese Journal of Applied Physics* 27, no. 5R (1988): 869.

[164] Yamashita, Masato, Shoji Yamaguchi, Toshifumi Nishii, Hiroshi Kurihara, and Hideo Enjoji. "Resistivity Correction Factor for the Four-Probe Method: Experiment II." *Japanese Journal of Applied Physics* 28, no. 5R (1989): 949.

[165] Yamashita, Masato, Toshifumi Nishi, Hiroshi Kurihara, Hideo Enjoji, and Atsushi Iwata. "Resistivity Correction Factor for the Four-Probe Method: Experiment III." *Japanese Journal of Applied Physics* 29, no. 4R (1990): 776.

[166] Wu, De Jian, Xin Ming Qian, and Ping Huang. "Safety Assessment on Hydrogen Peroxide for Storage and Transportation Based on Runaway Scenario." In *Applied Mechanics and Materials*, 79:215–20, 2011.

[167] Lousada, Cláudio M, Adam Johannes Johansson, Tore Brinck, and Mats Jonsson. "Mechanism of H2O2 Decomposition on Transition Metal Oxide Surfaces." *The Journal of Physical Chemistry C* 116, no. 17 (2012): 9533–43.

[168] Salem, Ibrahim A. "Kinetics of Hydrogen Peroxide Decomposition with Fe (III) and Cr (III)-Ethanolamines Complexes Sorbed on Dowex-50W Resin." *International Journal of Chemical Kinetics* 27, no. 5 (1995): 499–505.

[169] McKee, DW. "Catalytic Decomposition of Hydrogen Peroxide by Metals and Alloys of the Platinum Group." *Journal of Catalysis* 14, no. 4 (1969): 355–64.

[170] Eto, Isao, Miyako Akiyoshi, Atsumi Miyake, Terushige Ogawa, and Takehiro Matsunaga. "Hazard Evaluation of Runaway Reaction of Hydrogen Peroxide-Influence of Contamination of Various Ions." *Journal of Loss Prevention in the Process Industries* 22, no. 1 (2009): 15–20.

[171] Marzzacco, Charles J. "The Enthalpy of Decomposition of Hydrogen Peroxide: A General Chemistry Calorimetry Experiment." *Journal of Chemical Education* 76, no. 11 (1999): 1517.

[172] Serra Maia, Rui Filipe. *Relation between Surface Structural and Chemical Properties of Platinum Nanoparticles and Their Catalytic Activity in the Decomposition of Hydrogen Peroxide*, Dissertation, Virginia Tech, 2018.

[173] Vetter, Tiffany A, and D Philip Colombo Jr. "Kinetics of Platinum-Catalyzed Decomposition of Hydrogen Peroxide." *Journal of Chemical Education* 80, no. 7 (2003): 788.

[174] Brégeault, Jean-Marie. "Transition-Metal Complexes for Liquid-Phase Catalytic Oxidation: Some Aspects of Industrial Reactions and of Emerging Technologies." *Dalton Transactions*, no. 17 (2003): 3289–3302.

[175] Yang, Miao, Xian Zhang, Alex Grosjean, Inna Soroka, and Mats Jonsson. "Kinetics and Mechanism of the Reaction between H2O2 and Tungsten Powder in Water." *The Journal of Physical*

Chemistry C 119, no. 39 (2015): 22560–69.

[176] Gao, Y, TD Shen, Y Chen, HH Zhou, and SP Tong. "Degradation of Dimethyl Phthalate by Ti (IV)-Catalyzed O3/H2O2 under Acidic Conditions." *Huan Jing Ke Xue* 35, no. 8 (2014): 2980–84.

[177] Wu, Dejian, and Xinming Qian. "Experimental Study on the Thermal Runaway of Hydrogen Peroxide with in-/organic Impurities by a Batch Reactor." *Journal of Loss Prevention in the Process Industries* 51 (2018): 200–207.

[178] Lu, Kai-Tai, Ching-Chyuan Yang, and Peng-Chu Lin. "The Criteria of Critical Runaway and Stable Temperatures of Catalytic Decomposition of Hydrogen Peroxide in the Presence of Hydrochloric Acid." *Journal of Hazardous Materials* 135, no. 1–3 (2006): 319–27.

[179] Pal, P., K. Sato, and S. Chandra. "Fabrication Techniques of Convex Corners in a (1 0 0)-Silicon Wafer Using Bulk Micromachining: A Review." *Journal of Micromechanics and Microengineering* 17 (2007): R111.

[180] Pal, Prem, and Kazuo Sato. "A Comprehensive Review on Convex and Concave Corners in Silicon Bulk Micromachining Based on Anisotropic Wet Chemical Etching." *Micro and Nano Systems Letters* 3, no. 1 (2015): 6.

[181] Puers, B, and Willy Sansen. "Compensation Structures for Convex Corner Micromachining in Silicon." *Sensors and Actuators A:* Physical 23, no. 1–3 (1990): 1036–41.

[182] Scheibe, C, and E Obermeier. "Compensating Corner Undercutting in Anisotropic Etching of (100) Silicon for Chip Separation." *Journal of Micromechanics and Microengineering* 5, no. 2 (1995): 109.

[183] Merlos, A, M Acero, MH Bao, J Bausells, and J Esteve. "TMAH/IPA Anisotropic Etching Characteristics." *Sensors and Actuators A*: Physical 37 (1993): 737–43.

[184] Yang, Chii-Rong, Cheng-Hao Yang, and Po-Ying Chen. "Study on Anisotropic Silicon Etching Characteristics in Various Surfactant-Added Tetramethyl Ammonium Hydroxide Water Solutions." *Journal of Micromechanics and Microengineering* 15, no. 11 (2005): 2028.

[185] Yang, Chii-Rong, Po-Ying Chen, Cheng-Hao Yang, Yuang-Cherng Chiou, and Rong-Tsong Lee. "Effects of Various Ion-Typed Surfactants on Silicon Anisotropic Etching Properties in KOH and TMAH Solutions." *Sensors and Actuators A*: Physical 119, no. 1 (2005): 271–81.

[186] Yao, Mingqiu, Bin Tang, Kazuo Sato, and Wei Su. "Silicon Anisotropic Etching in Triton-Mixed and Isopropyl Alcohol-Mixed Tetramethyl Ammonium Hydroxide Solution." *Micro & Nano Letters* 10, no. 9 (2015): 469–71.

[187] Rola, Krzysztof P. "Anisotropic Etching of Silicon in KOH+ Triton X-100 for 45 Micromirror Applications." *Microsystem Technologies* 23, no. 5 (2017): 1463–73.

[188] Paria, Santanu, C Manohar, and Kartic C Khilar. "Kinetics of Adsorption of Anionic, Cationic, and Nonionic Surfactants." *Industrial & Engineering Chemistry Research* 44, no. 9 (2005): 3091–98.

[189] Haiss, Wolfgang, Philipp Raisch, Lennart Bitsch, Richard J Nichols, Xinghua Xia, John J Kelly,

and David J Schiffrin. "Surface Termination and Hydrogen Bubble Adhesion on Si (100) Surfaces during Anisotropic Dissolution in Aqueous KOH." *Journal of Electroanalytical Chemistry* 597, no. 1 (2006): 1–12.

[190] Gosalvez, MA, B Tang, P Pal, K Sato, Y Kimura, and K Ishibashi. "Orientation-and Concentration-Dependent Surfactant Adsorption on Silicon in Aqueous Alkaline Solutions: Explaining the Changes in the Etch Rate, Roughness and Undercutting for MEMS Applications." *Journal of Micromechanics and Microengineering* 19, no. 12 (2009): 125011.

[191] Pal, Prem, and Kazuo Sato. *Silicon Wet Bulk Micromachining for MEMS*. CRC Press, 2017.

[192] Ben-Yaakov, Sam, Mor Mordechai Peretz, and Bryce Hesterman. "A SPICE Compatible Behavioral Electrical Model of a Heated Tungsten Filament." In *Applied Power Electronics Conference and Exposition*, Twentieth Annual IEEE, 2:1079–84, 2005.

[193] Heyd, R, A Hadaoui, and ML Saboungi. "1D Analog Behavioral SPICE Model for Hot Wire Sensors in the Continuum Regime." *Sensors and Actuators A*: Physical 174 (2012): 9–15.

[194] Miller, IS, DA Shah, and RA Antonia. "A Constant Temperature Hot-Wire Anemometer." *Journal of Physics E: Scientific Instruments* 20, no. 3 (1987): 311.

[195] Freymuth, P. "Frequency Response and Electronic Testing for Constant-Temperature Hot-Wire Anemometers." *Journal of Physics E: Scientific Instruments* 10 (1977): 705.

[196] Freymuth, Peter. "Theory of Frequency Optimisation for Hot-Film Anemometers." *Journal of Physics E: Scientific Instruments* 11, no. 2 (1978): 177.

[197] Teo, CJ, BC Khoo, and YT Chew. "The Dynamic Response of a Hot-Wire Anemometer: IV. Sine-Wave Voltage Perturbation Testing for near-Wall Hot-Wire/film Probes and the Presence of Low-High Frequency Response Characteristics." *Measurement Science and Technology* 12, no. 1 (2001): 37.

[198] Kidron, Izhak. "Measurement of the Transfer Function of Hot-Wire and Hot-Film Turbulence Transducers." *Instrumentation and Measurement,* IEEE Transactions on 15, no. 3 (1966): 76–81.

[199] Bonnet, JP, and T Alziary de Roquefort. "Determination and Optimization of Frequency Response of Constant Temperature Hot-Wire Anemometers in Supersonic Flows." *Review of Scientific Instruments* 51, no. 2 (1980): 234–39.

[200] Gavin, Henri. "The Levenberg-Marquardt Method for Nonlinear Least Squares Curve-Fitting Problems." *Department of Civil and Environmental Engineering*, Duke University, 2011, 1–15.

[201] Al-Garni, Abdullah M. "Low Speed Calibration of Hot-Wire Anemometers." *Flow Measurement and Instrumentation* 18, no. 2 (2007): 95–98.

Acknowledgment